Measurement of turbulent scalar mixing by means of a combination of PIV and LIF

Measurement of turbulent scalar mixing by means of a combination of PIV and LIF

Proefschrift

ter verkrijging van de graad van doctor
aan de Technische Universiteit Delft,
op gezag van de Rector Magnificus prof. dr. ir. J.T. Fokkema,
voorzitter van het College voor Promoties,
in het openbaar te verdedigen op dinsdag 29 oktober 2002 om 16.00 uur,

door

Lourens AANEN
natuurkundig ingenieur
geboren te Meerkerk

Dit proefschrift is goedgekeurd door de promotoren:
Prof. dr. ir. J. Westerweel
Prof. dr. ir. F.T.M. Nieuwstadt

Samenstelling promotiecommissie:

Rector Magnificus, voorzitter
Prof. dr. ir. J. Westerweel, Technische Universiteit Delft, promotor
Prof. dr. ir. F.T.M. Nieuwstadt, Technische Universiteit Delft, promotor
Prof. dr. ir. A.A. van Steenhoven , Technische Universiteit Eindhoven,
Prof. dr. ir. G. Ooms, Technische Universiteit Delft,
Prof. dr. ir. J.J.M. Braat, Technische Universiteit Delft,
Dr. ir. W.S.J. Uijttewaal, Technische Universiteit Delft,
Dr. ir. R.E. Uittenbogaard, WL|Delft Hydraulics

Published and distributed by: DUP Science

DUP Science is an imprint of
Delft University Press
P.O. Box 98
2600 MG Delft
The Netherlands
Telephone +31 15 27 85 678
Telefax +31 15 27 85 706
E-mail: Info@Library.TUDelft.NL

ISBN 90-407-2351-6

Keywords: PIV, LIF, mixing

Printed in The Netherlands

Acknowledgements

This thesis is based on more than four years of research at the Laboratory of Aero- & Hydrodynamics of the Delft University of Technology. This thesis is about turbulent mixing, a subject with many applications and many unsolved problems.

Without the help of many other people it would have been impossible to finish al the work presented in this thesis. First of all I would like to thank professor Nieuwstadt and my supervisor professor Westerweel. Without their knowledge, experience and help I would have been totally lost. As for my work is beside a scientific work also a technical work, I also have to thank all the supporting people at the lab: Ruud, Joop, Roland and Cor, without your help and support I would never have been able to do the work I did.

The authors of chapter 6 would like to thank Dr.ir. B.J. Boersma for his contributions to this project.

Antonio! Life would have been lonely and hard if you would not have been there in combining the two measurement techniques for the first time. We spent quite some time together in the basement, trying to solve technical problems. Thanks for all your help and pleasant hours beside the work.

I would like to thank Pim van der Salm to help me bridge the gap between Word and Latex. Without his help the last chapter of this thesis whould have been without any graphics.

I would also like to thank all my colleagues. It was always pleasant to work in our group. We all together made a lot of fun.

Last but not least I would like to thank all the people who gave me the moral support I needed. The people who told me I could do it when I doubted. I think that help was the most important for me.

Delft, September 17 2002

This work was made possible by the financial support of the Nederlandse Organisatie voor Wetenschappelijk Onderzoek and the Stichting Technische Wetenschappen, project number DWT44.3296 which is gratefully acknowledged.

Contents

Summary

In order to gain a better insight in the physics of turbulent mixing, a research project was started at Delft University of Technology to investigate the possibilities for a non-intrusive two dimensional measurement method for simultaneous measurements of concentrations and velocities. To develop this measurement technique, two existing measurement techniques are combined. The first measurement technique is Particle Image Velocimetry (PIV), used to measure two-dimensional velocity fields. The second measurement technique is Laser Induced Fluorescence (LIF), used to measure two-dimensional concentration fields. The final goal of the combined measurement technique is to measure the correlation between velocity fluctuations and concentration fluctuations, $\overline{u'c'}$, quantitatively, because these correlations appear in the Reynolds averaged scalar transport equation.

As test case for the measurement technique two different flow geometries are considered. The first one is a point source of a passive scalar, placed at the centerline of a turbulent pipe flow. The second flow geometry is a turbulent jet containing a passive scalar. For both geometries the combined measurement technique is capable to measure all terms in the Reynolds averaged transport equation.

The reliability of the PIV technique is checked by comparing the measured velocity statistics with results in the literature, for flows with the same geometry and the same Reynolds number. Also the concentration statistics as obtained with the LIF technique are compared with similar results in the literature. Results for the mean concentrations agree well with these results. The concentration RMS values are underestimated due to a too low measurement resolution to resolve the Batchelor scale.

For the point source the concentration-velocity correlations are measured at distances between 0.5 and 4.5 pipe diameters behind the the point source. For short distances behind the the point source the balance between transport by the mean flow and the turbulent transport is not closed. This is probably caused by a resolution problem in the turbulent transport measurements. For larger distances behind the point source, the turbulent transport data are not statistically converged, so no conclusions can be drawn about the balance. This is caused by the small amount of fluorescein injected and the physical nature of a point source. For the

jet measurements the balance is closed.

Samenvatting

Om beter inzicht te verkrijgen in de fysica van het turbulente mengproces, is aan de Technische Universiteit Delft een onderzoek gedaan naar de mogelijkheid van een niet intrusieve meettechniek voor het simultaan, twee dimensionaal meten van snelheids- en concentratievelden. Daartoe zijn twee bestaande meettechnieken met elkaar gecombineerd. De eerste meettechniek is Particle Image Velocimetry (PIV), bedoeld voor het meten van twee-dimensionale snelheidsvelden, de tweede meettechniek is Laser Induced Fluorescence (LIF), bedoeld voor het meten van twee-dimensionale concentratievelden. Het uiteindelijke doel van de meetechniek is het quantitatief meten van de correlatie tussen snelheidsfluctuaties en concentratiefluctuaties, $\overline{u'c'}$, zoals die voorkomen in de Reynolds-gemiddelde scalair transport vergelijking voor de concentratie.

Als test case voor de meettechniek zijn twee verschillende stromingsgeometrieën gebruikt. De eerste is een puntbron van een passieve scalar op de hartlijn van een turbulente buisstroming. De tweede stromingsgeometrie is een turbulente straal met een passieve scalar. Voor beide geometrieën zijn met de gecombineerde meettechniek alle in de Reynoldsgmiddelde transportvergelijking voorkomende termen te meten.

De goede werking van de PIV techniek is geverifieerd door de gemeten snelheidsstatistiek te vergelijken met de in de literatuur bekende statistieken voor metingen en berekeningen aan dezelfde geometrieën en bij hetzelfde Reynolds getal. Ook de met LIF gemeten concentratiestatistiek is vergeleken met literatuurgegevens voor dezelfde geometrieën. De resultaten voor de concentratie komen voor de gemiddelde stroming goed overeen. De concentratie RMS-waarden worden onderschat ten gevolge van een te lage resolutie in de metingen om de Batchelor schaal op te kunnen lossen.

Voor de puntbron zijn de concentratie-snelheidscorrelaties gemeten in het gebied tussen 0.5 en 4.5 pijp diameters na de puntbron. Voor korte afstanden na de puntbron is de balans tussen het transport door de gemiddelde stroming en het turbulente transport niet sluitend. Dit komt waarschijnlijk door een resolutie probleem in de turbulente tranport metingen. Voor grotere afstanden van de puntbron is de statistiek niet ver genoeg geconvergeerd om uitspraken te kunnen doen over de balans. Dit wordt veroorzaakt door de kleine hoeveelheid scalar die geinjecteerd

wordt. Voor de straalmetingen is de balans wel sluitend.

List of symbols

symbol	description	dimension
Normal symbols		
b	image distance	m
c	dye concentration	$molm^{-3}$
D	pipe diameter	m
D	lens diameter	m
d_i	size of interrogation area in object plane	m
d_p	particle diameter	m
d_s	diameter of Airy pattern	m
d_t	particle image diameter	m
F	scalar production	$molm^{-3}s^{-1}$
f	frequency	Hz, s^{-1}
f	focal length	m
I_0	initial light intensity	Wm^{-2}
I_l	light intensity at measurement position	Wm^{-2}
K	turbulent diffusivity of mass	m^2s^{-1}
L	typical length scale	m
M	image magnification	-
p	pressure	Pa
R	correlation	-
Re	Reynolds number	-
Ra	Rayleigh length	m
r	radial direction in cylindrical flow	m
S	source strength of concentration	$molm^{-2}$
Sc	Schmidt number	-
t	time	s
$t_{\mathcal{D}}$	Batchelor time scale	s

U	typical velocity	ms^{-1}
U_i	mean velocity in i direction	ms^{-1}
u	axial velocity in cylindrical flow	ms^{-1}
u_i	i-component of velocity vector	ms^{-1}
u_p	particle velocity	ms^{-1}
u_*	friction velocity	ms^{-1}
v	object distance	m
v	radial velocity in cylindrical flow	ms^{-1}
w	radius of the waist	ms^{-1}
x	stream-wise direction in cylindrical flow	m
x_i	i-component of position vector	m
$z_{1,2}$	distance from waist to lens	m
z_0	image distance	m
Greek symbols		
δz	focal depth	m
ϵ	extinction coefficient	$lm^{-1}mol^{-1}$
ϵ	dissipation of kinetic energy	m^2s^{-3}
η	Kolmogorov length scale	m
λ	wavelength	m
$\lambda_{\mathcal{D}}$	Batchelor length scale	m
ν	kinematic viscosity	m^2s^{-1}
ρ	density	kgm^{-3}
ρ_p	density of particles	kgm^{-3}
σ	standard deviation	m
τ	Kolmogorov time scale	s
τ_p	time constant of particles	s
τ_s	turbulent wall stress	Pa
φ	quantum yield	-
Calligraphic symbols		
$\mathcal{D}$	diffusivity of mass	m^2s^{-1}

Chapter 1

General introduction

1.1 General background

The most frequently used benificial property of turbulence in practice is doubtlessly its efficient mixing. Every day millions of people make use of this property by stirring in their coffee cups to mix the added sugar and milk. Also in industry, mixing by turbulence is one of the key processes, for example in chemical reactors. The designs of such mixing devices are often the result of years of experience, but it is rarely based on scientific research for the optimization of the mixing. Therefor in this thesis the mixing problem is studied. The primary goal of the research described here is not to optimize industrial mixers, but to obtain a better understanding of the basic principles of mixing. To gain a better understanding of mixing good and detailed measurements have to be done. To be able to do so a reliable and validated measurement technique is needed. Therefore it is our first aim to develop a good measurement technique to observe quantities of interest for mixing. A secondary goal is to apply this technique to some well-known flow geometries.

Before we can develop a measurement tool to study mixing, we first have to find out what we want to measure and to check if such measurements can not be done with help of existing measurement techniques. Turbulent mixing is the interaction between a turbulent flow and the concentration field of a scalar present in the flow. We will therefore concentrate on measurement techniques for concentrations and velocity fields.

One of the most powerful "measurement tools" that we have is, although often forgotten, the eye. Observation of mixing by eye provides us with a lot of qualitative results about the mixing process, like the important role of vortices in the mixing process. One can observe that large-scale motion of the fluid can cause small-scale concentration structures if the diffusion coefficient is small. For many applications however qualitative results alone are not sufficient. To be able to know quantities

like maximum concentrations in a mixing flow at a certain position behind a source of a scalar, measurements have to be done. Until now such measurements were mainly done in a point in the flow, both for the concentrations and the velocities. Over the last few years techniques have become available which are able to measure full two-dimensional concentration and velocity fields. As mentioned before, mixing is the interaction between the velocity field and the concentration field. The next logical step to the development of measurement techniques for mixing is to try to measure the concentration and the velocity fields simultaneously. Such measurements will allow us to measure the interaction directly and will provide us with information about the importance of coherent structures in the turbulent flow field on the mixing process or in general about which turbulent structures contribute to the correlation between velocity and concentration data. The final goal should be to do this time resolved and in all three dimensions, but with the techniques available at present this is not yet possible. Therefore the goal of the work presented in this thesis is to develop and test a measurement tool for measuring simultaneously and time resolved the two-dimensional concentration and turbulent velocity fields.

1.2 Two dimensional measurements

For an axisymmetric geometry, the mean fields depend only on the streamwise and the radial direction, and they do not depend on the tangential direction. In other words, the mean flow and concentration field can be considered as two-dimensional. For that reason the experiments presented in this thesis are performed on two simple two dimensional mixing flows, a continuous point source placed at the centerline of a turbulent pipe flow and a jet with a passive scalar.

If molecular diffusion can be neglected, the mean concentration field $\overline{c}$ in case of the point source geometry, can be described by the following equation:

$$-U_x \frac{\partial \overline{c}}{\partial x} = \frac{\partial \overline{u'_x c'}}{\partial x} + \frac{1}{r} \frac{\partial r \overline{u'_r c'}}{\partial r}, \tag{1.1}$$

in which x is the axial coordinate, r is the radial coordinate, U_x is the time averaged axial velocity, c' is the fluctuating component of the concentration and u'_x and u'_r are the fluctuating axial and radial velocity components. As can be seen only axial and radial velocities and concentration gradients in the axial and radial direction are present in this equation. The two terms on the right-hand side of the equation contain gradients of the correlations between turbulent fluid motion and fluctuating concentration. To be able to measure these terms simultaneous concentration and velocity measurements have to be done. To be able to study the role of coherent velocity structures on the mixing process, these structures together with the scalar field should be investigated. Two-dimensional measurements are necessary to be able to do so.

Not every interesting feature of the two mixing problems proposed can be measured. Since only two-dimensional data are obtained, no three-dimensional effects can be measured. For that reason parallel to the study presented in this thesis a numerical study was done by (Brethouwer 2001). Brethouwer performed a Direct Numerical Simulation (DNS) of the same flow geometry as used in the experiment carried out for this investigation. In a DNS the full Navier Stokes equations, and in case of a mixing flow also the mass transport equations, are numerically solved on a grid which is fine enough to capture the smallest velocity and concentration scales present in the flow. The only difference between the experimental and the numerical work is the diffusion coefficient of the scalar.

1.3 Outline of this thesis

In chapter two the theoretical background of the mixing problem is described. The turbulent mass transport equation introduced in the previous section is derived and the models used for comparison with the measurements are described.

To be able to measure two-dimensional velocity and concentration data simultaneously, a technique for measuring two-dimension velocity fields is combined with a technique to measure two dimensional concentration fields. These measurement techniques are described in chapter 3.

For measuring two-dimensional velocity fields we have Particle Image Velocimetry (PIV). With PIV an estimation of the fluid velocity is made by measuring the motion of small tracer particles present in the flow. In the case of the point source doubly exposed images of the flow are made. The displacement of the tracer particles is determined by computing an autocorrelation in a so-called interrogation area as described in chapter 3. For the jet two singly exposed measurements with a short time interval are made, from which the particle displacements are estimated with help of a cross-correlation technique.

For measuring two-dimensional concentration fields Laser Induced Fluorescence (LIF) is used. LIF is a technique based on the linear relation between the concentration of fluorescent dye and the amount of light emitted by the dye when it is illuminated with light of a certain wavelength. Dye concentrations can be so low that buoyancy effects can be neglected. The technique has been used already for a longer time in visualization studies, but with modern cameras it can be also used for measuring two dimensional concentration fields quantitatively.

In chapter 4 we describe the experimental setup, in which our measurements are done. This setup consists of a flow system and the combined measurement systems. The combination of the two measurement techniques requires a setup with a good optical accessibility. To be able to acquire a velocity field with PIV and a

concentration field with LIF within one Kolmogorov time scale fast shutters and cameras are required. The timing of all components is a rather complicated problem to solve; i.e. three lasers, two camera's and an extra shutter are to be operated simultaneously.

In chapter 5 we present the results of the measurements of a point source placed at the centerline of a turbulent pipe flow. The statistics of the flow field are used to check the reliability of the PIV measurements. The statistics of the concentration measurements are used to check the reliability of the LIF technique.

The combination of both measurement techniques is used to determine the correlation between concentrations and velocities quantitatively.

In chapter 6 we discuss the results of measurements of a jet with a passive scalar. Like in the case of the point source, measurements of the velocity statistics, the concentration statistics and the correlations between concentrations and velocities are presented.

In chapter 7 we give the conclusions which can be drawn from the results presented and some recommendations for further research. Finally some recommendations are given aimed to improve the measurements and measurements involving chemical reactions.

Chapter 2

Theory

2.1 Introduction

In this chapter we describe the basic equations that are relevant for turbulent mixing processes, and we discuss the most important scaling parameters for turbulent mixing. Besides that the closure by K-theory for the mixing in axisymmetric flows is restated. The two flow geometries considered are a point source of a passive scalar placed at the centerline of a turbulent pipe flow, and a free jet containing a passive scalar. In the last section of this chapter some remarks are made on the role of coherent structures in the mixing process.

For an introduction to the principles of turbulent flows one should consult the standard text books for example (Hinze 1975).

2.2 Mixing

Turbulent mixing is the dispersion of a scalar by turbulent fluctuations until the scale where molecular diffusion becomes dominant. To be able to measure this dispersion process, simultaneous measurements of the concentration and velocity field are needed.

In the present study we consider the mixing of a passive scalar, i.e. there are no chemical reactions and the scalar field has no influence on the velocity field. The working fluid in our case is water, and the passive scalar is a fluorescent dye, as will be described in section 3.3.1. The scalar transport can be described with the mass transport equation, which is given by:

$$\frac{\partial c}{\partial t} + u_i \frac{\partial c}{\partial x_i} = \mathcal{D} \frac{\partial^2 c}{\partial x_i^2} + F(x_i, c) \tag{2.1}$$

where $\mathcal{D}$ is the scalar diffusivity, c the concentration of the scalar, u_i the velocity vector and $F(x_i, c)$ represents a source or sink. For a flow without chemical reactions $F(x_i, c)$ is identical zero except at the position of any sources. In this study we consider a single continuous source at the position $x = x_0$, so that $F(x_i, c) = c_0\delta(x - x_0, r)$.

The mass transport equation can be written in a dimensionless form using a typical length scale L, a typical velocity scale U, the diffusivity of mass $\mathcal{D}$ and the viscosity ν. The result reads

$$\frac{\partial \tilde{c}}{\partial t} + \tilde{u}_i \frac{\partial \tilde{c}}{\partial \tilde{x}_i} = \frac{1}{\mathrm{Re\ Sc}} \frac{\partial^2 \tilde{c}}{\partial \tilde{x}_i^2} + \tilde{F}(x, c), \tag{2.2}$$

in which a tilde denotes a dimensionless parameter. The only scaling parameters appearing in the equation are the Reynolds number Re and the Schmidt number Sc. The Schmidt number of a scalar is defined as

$$\mathrm{Sc} = \frac{\nu}{\mathcal{D}}. \tag{2.3}$$

The Schmidt number is the ratio between the diffusivity of momentum ν and the diffusivity of mass $\mathcal{D}$. The Reynolds number, Re$= UL/\nu$, is the ratio between inertial forces and viscous forces in the flow. For turbulent flows Re$\gg$1.

The velocity field is described by the continuity equation and the Navier-Stokes equations, to be presented in section 2.3.

2.2.1 Scaling

The macro or the large scales of the concentration field are completely determined by the velocity field. A simple model for these scales is given in section 2.4.1. The smallest concentration scales are determined by a competition between the deformation of the concentration field by the smallest velocity scales, and the molecular diffusion (Batchelor *et al.* 1959b). These scales are known as the Batchelor scales. The Batchelor length scale and time scale are defined as:

$$\lambda_{\mathcal{D}} = \frac{\eta}{\mathrm{Sc}^{\frac{1}{2}}},\ t_{\mathcal{D}} = \frac{\lambda_{\mathcal{D}}^2}{\mathcal{D}}, \tag{2.4}$$

where Sc is the Schmidt number of the scalar and η the Kolmogorov length scales, i.e. the smallest length scale of the turbulent flow field (see section 2.3.1). Relationship (2.4) which is valid for Sc$\gg$1, shows that the smallest concentration scales are proportional to $\mathrm{Sc}^{1/2}$. For flows with Sc$\gg$1 molecular diffusion comes only into play at very small scales. This is the case in many flows with solvents with a relative high molecular weight in water. For flows with Sc$\ll$1 at the other hand, molecular diffusion play already a role at scales larger than the Kolmogorov length

scale. In that case the smallest concentration scales seem to become independent of the flow field (Batchelor *et al.* 1959), although Gibson (1968a, b) reports a universal geometrical scaling following $t_{\mathcal{D}} \sim (D/\epsilon)^{1/2}$ for all Sc. Such a behavior was also confirmed by the computations of Brethouwer (2001).

In our case the scalar used is fluorescein. For fluorescein dissolved in water the diffusivity is 4.8×10^{-4} mm^2/s. Hence in our case the Schmidt number is about 2075, and with a typical value for the Kolmogorov scale in our case $\eta = 0.22$ mm, the Batchelor length scale becomes $\lambda_{\mathcal{D}} = 4.8\mu$m and the Batchelor time scale becomes $t_{\mathcal{D}} = 25$ms.

2.3 Turbulent flow field

The equations of motion for an incompressible fluid are given by the continuity equation and the Navier-Stoles equations. The continuity equation reads:

$$\frac{\partial u_i}{\partial x_i} = 0, \tag{2.5}$$

in which u_i is the velocity in the x_i direction. For a homogeneous, Newtonian fluid the Navier Stokes equations are:

$$\frac{\partial u_i}{\partial t} + u_j \frac{\partial u_i}{\partial x_j} = -\frac{1}{\rho}\frac{\partial p}{\partial x_i} + \nu \frac{\partial^2 u_i}{\partial x_j^2}, \tag{2.6}$$

where ρ is the density of the fluid, ν the kinematic viscosity of the fluid and p is the pressure. We can write these equations in a dimensionless form using again the typical velocity U, a typical length scale L and the kinematic viscosity ν already used in the previous section. In dimensionless form the continuity equation becomes

$$\frac{\partial \tilde{u}_i}{\partial \tilde{x}_i} = 0 \tag{2.7}$$

with $\tilde{u}_i = u_i/U$ and $\tilde{x}_i = x_i/L$. The Navier-Stokes equation becomes

$$\frac{\partial \tilde{u}_i}{\partial \tilde{t}} + \tilde{u}_j \frac{\partial \tilde{u}_i}{\partial \tilde{x}_j} = -\frac{\partial \tilde{p}}{\partial \tilde{x}_i} + \frac{1}{\mathrm{Re}} \frac{\partial^2 \tilde{u}_i}{\partial \tilde{x}_j^2}. \tag{2.8}$$

with $\tilde{t} = tL/U$ and $\tilde{p} = p/(\rho U^2)$.

2.3.1 Scaling of turbulent pipe flow.

A turbulent flow is characterized by a wide range of flow scales. The smallest scales in the flow are determined by the kinematic viscosity ν and the energy dissipation

ϵ. These scales, called the Kolmogorov scales, are defined as:

$$\eta = \left(\frac{\nu^3}{\epsilon}\right)^{\frac{1}{4}}, \tag{2.9}$$

for the Kolmogorov length scale,

$$\tau = \left(\frac{\nu}{\epsilon}\right)^{\frac{1}{2}}, \tag{2.10}$$

for the Kolmogorov time scale and

$$v = (\nu\epsilon)^{\frac{1}{4}}, \tag{2.11}$$

for the Kolmogorov velocity scale. The energy dissipations scales like

$$\epsilon \approx U^3/L \tag{2.12}$$

where U and L are representative velocity and length scales introduced above.

In wall-bounded turbulent flows the characteristic velocity scale is usually taken equal to friction velocity u_* which is defined as:

$$u_* = \sqrt{\frac{\tau_s}{\rho}} \tag{2.13}$$

where τ_s is the wall shear stress. In the case of a fully-developed turbulent pipe flow the shear stress on the wall is related to the pressure drop along the pipe according to

$$\tau_s = \frac{-D}{4}\frac{\partial \overline{p}}{\partial x}, \tag{2.14}$$

so that

$$u_* = \left(\frac{-\mathrm{D}}{4\rho}\frac{\partial \overline{p}}{\partial x}\right)^{\frac{1}{2}}. \tag{2.15}$$

On average there is a balance between production and dissipation of turbulence in a pipe. All energy produced by wall shear stresses is finally dissipated by the turbulence. So, for the volume-averaged turbulent dissipation $<\epsilon>$ the we can write:

$$<\epsilon> = \frac{1}{\rho}\overline{u}\frac{\partial \overline{p}}{\partial x}, \tag{2.16}$$

with $\overline{u}$ the mean or bulk velocity. For a fully developed turbulent pipe flow substitution of (2.15) into (2.16) leads to:

$$<\epsilon> = 4u_*^2\frac{\overline{u}}{\mathrm{D}} \tag{2.17}$$

Table 2.1: The values of relevant flow parameters of the turbulent pipe flow used in this study, with water as fluid. The Reynolds numbers used, based on the bulk velocity, are 5300 and 10000.

Re	5300	10000
D (mm)	50	50
ρ (kg/m^3)	1000	1000
ϵ (mm^2/s^3)	431	2532
ν (m^2/s)	1.0×10^{-6}	1.0×10^{-6}
η (mm)	0.22	0.14
τ (ms)	48	20
v (mm/s)	4.6	7.1
u_* (mm/s)	7.2	12.6
$\overline{u}$ (mm/s)	106	200
$\mathcal{D}$ (mm^2/s)	4.8×10^{-4}	4.8×10^{-4}
$\lambda_\mathcal{D}$ (μm)	4.8	3.1
$t_\mathcal{D}$ (ms)	48	20

With this expression for the dissipation the average Kolmogorov length scale can be estimated by substitution of (2.17) in (2.9). This leads to:

$$\eta = \left(\frac{\nu^3 \mathrm{D}}{4\overline{u}u_*^2} \right)^{\frac{1}{4}}. \tag{2.18}$$

In table 2.1 the different values of the Kolmogorov scales and other important flow variables are given for a tube of 50 mm diameter and Reynolds numbers of 5300 and 10000 in which the Reynolds number is based on the pipe diameter and the bulk velocity. The Re value of 5300 was chosen because it corresponds to the value used by Brethouwer (2000) in his direct numerical simulation (DNS). In the DNS the same flow geometry was used (although no disturbances from a injection mechanism for fluorescein was present,) however in the DNS the Schmidt number of the flow was 1, while the Schmidt number in the experiments was 2400. This will have consequence for the small scale concentration fluctuations

2.4 Axisymmetric flows

As mentioned in the introduction of this thesis, we present the results of measurements in two different flow geometries. The first is a point source of a passive scalar placed at the centerline of a fully developed turbulent pipe flow; the second is a free jet containing a passive scalar. A sketch of the first flow geometry is given in figure 2.1.

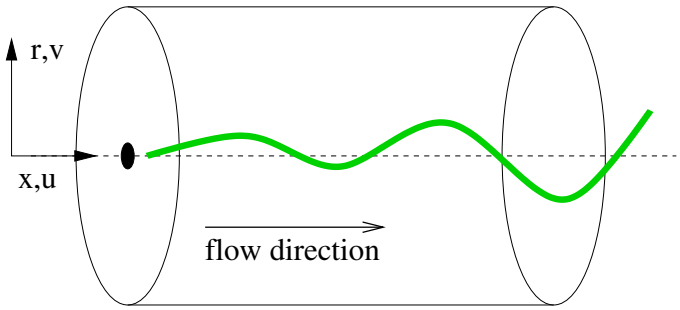

Figure 2.1: A point source at the centerline of a pipe.

A point source at the centerline of a turbulent pipe flow was chosen for the reason that due to axisymmetry, terms in the Reynolds averaged scalar transport equations vanish (see equation 2.24). All remaining terms in the transport equation can be measured with our two-dimensional measurement techniques. Besides that, the turbulence at the centerline of a pipe is close to homogeneous, for which an analytical solution exists and which can be compared with our results. The third reason for choosing a point source in a turbulent pipe flow is that for this geometry also results from a Direct Numerical Simulation (DNS) are available.

For an axisymmetric, stationary turbulent flow without swirl with a continuous point source at the centerline, all mean gradients in the tangential direction and time derivatives vanish, and the mean velocity has only components in the axial and radial flow directions. Let us split the velocity components and the concentration in a mean component and fluctuating component, $u_i = U_i + u_i'$ and $c = \overline{c} + c'$, with $\overline{u_i'} = 0$ and $\overline{c'} = 0$. The Reynolds-averaged scalar transport equation in a cylindrical coordinate system (x, r, θ) then becomes:

$$U_x \frac{\partial \overline{c}}{\partial x} + U_r \frac{\partial \overline{c}}{\partial r} = -\overline{u_x' \frac{\partial c'}{\partial x}} - \overline{u_r' \frac{\partial c'}{\partial r}} + \mathcal{D}\left\{ \frac{\partial^2 \overline{c}}{\partial x^2} + \frac{1}{r}\frac{\partial}{\partial r}\left(r \frac{\partial \overline{c}}{\partial r} \right) \right\} \tag{2.19}$$

We can write

$$u_x' \frac{\partial c'}{\partial x} = \frac{\partial u_x' c'}{\partial x} - c' \frac{\partial u_x'}{\partial x}. \tag{2.20}$$

and

$$u_r' \frac{\partial c'}{\partial r} = \frac{1}{r}\frac{\partial r u_r' c'}{\partial r} - c' \frac{1}{r}\frac{\partial r u_r'}{\partial r}. \tag{2.21}$$

Using continuity the last terms in (2.20) and (2.21) vanish if they are summed and therefore (2.19) can be written as:

$$U_x \frac{\partial \overline{c}}{\partial x} + U_r \frac{\partial \overline{c}}{\partial r} = -\frac{\partial \overline{u_x' c'}}{\partial x} - \frac{1}{r}\frac{\partial r \overline{u_r' c'}}{\partial r} + \mathcal{D}\left\{ \frac{\partial^2 \overline{c}}{\partial x^2} + \frac{1}{r}\frac{\partial}{\partial r}\left(r \frac{\partial \overline{c}}{\partial r} \right) \right\}. \tag{2.22}$$

Due to the high Schmidt and Reynolds numbers of the flow the last term in (2.22) is negligible. The transport equation for the mean concentration can therefore be simplified to

$$-U_x\frac{\partial \overline{c}}{\partial x} - U_r\frac{\partial \overline{c}}{\partial r} = \frac{\partial \overline{u_x' c'}}{\partial x} + \frac{1}{r}\frac{\partial r\overline{u_r' c'}}{\partial r}. \tag{2.23}$$

In the case of a fully-developed turbulent pipe flow with a point source on the centerline the mean flow has only a component in the streamwise direction, so the second term at the left-hand side vanishes and the transport equation becomes:

$$-U_x\frac{\partial \overline{c}}{\partial x} = \frac{\partial \overline{u_x' c'}}{\partial x} + \frac{1}{r}\frac{\partial r\overline{u_r' c'}}{\partial r}. \tag{2.24}$$

In this equation only streamwise and radial velocity components and concentration fluctuations are present. The velocity components can be measured using two-component planar Particle Image Velocimetry. The concentration and concentration gradient can be measured using planar Laser Induced Fluorescence. A description of the two measurement techniques will be given in Chapter 3.

The Reynolds-averaged Navier Stokes equations for an axisymmetric flow can be derived in the same way as done for the mass transport equations. This leads to:

$$\frac{\partial U_x}{\partial t} + U_x\frac{\partial U_x}{\partial x} + U_r\frac{\partial U_x}{\partial r} + \overline{u_x'\frac{\partial u_x'}{\partial x}} + \overline{u_r'\frac{\partial u_x'}{\partial r}} = \frac{-1}{\rho}\frac{\partial \overline{p}}{\partial x} + \nu\left(\frac{\partial^2 U_x}{\partial x^2} + \frac{1}{r}\frac{\partial}{\partial r}\left(r\frac{\partial U_x}{\partial r}\right)\right) \tag{2.25}$$

for the axial velocity and

$$\frac{\partial U_r}{\partial t} + U_x\frac{\partial U_r}{\partial x} + U_r\frac{\partial U_r}{\partial r} + \overline{u_x'\frac{\partial u_r'}{\partial x}} + \overline{u_r'\frac{\partial u_r'}{\partial r}} = \frac{-1}{\rho}\frac{\partial \overline{p}}{\partial r} + \nu\left(\frac{\partial^2 U_r}{\partial x^2} + \frac{1}{r}\frac{\partial}{\partial r}\left(r\frac{\partial U_r}{\partial r}\right)\right) \tag{2.26}$$

for the radial velocity.

For a stationary axisymmetric jet flow, the time derivatives vanish. For a stationary turbulent pipe flow, (2.26) vanishes and (2.25) becomes:

$$\frac{\partial U_x}{\partial t} + \overline{u_r'\frac{\partial u_x'}{\partial r}} = \frac{-1}{\rho}\frac{\partial \overline{p}}{\partial x} + \nu\frac{1}{r}\frac{\partial}{\partial r}\left(r\frac{\partial U_x}{\partial r}\right), \tag{2.27}$$

or, using continuity,

$$\frac{\partial U_x}{\partial t} + \frac{\partial \overline{u_r' u_x'}}{\partial r} = \frac{-1}{\rho}\frac{\partial \overline{p}}{\partial x} + \nu\frac{1}{r}\frac{\partial}{\partial r}\left(r\frac{\partial U_x}{\partial r}\right), \tag{2.28}$$

So for the pipe-flow the complete flow is characterized by the mean flow U_x and $\overline{u_r' u_x'}$.

2.4.1 The Reynolds stress modeling

To get a first impression of the mean concentration profile of the pipe flow, a very simple mixing model is considered. At the centerline of the pipe flow, the turbulence can be considered to be almost homogeneous and isotropic. This means that all components of the velocity fluctuations are equal and independent of the position. As can be seen in figure 5.1b, where the axial and the radial turbulent velocity fluctuations are plotted as function of the radial position, this is a good approximation near the centerline of the pipe. The velocity gradients of the mean flow should be zero. Near the centerline of a turbulent pipe flow, velocity gradients are clearly small. The initial spreading of the plume is therefore estimated by computing the spreading of a point source placed in a uniform flow with isotropic turbulence. This estimation is made by using the so-called K-theory (Hinze 1975). This theory assumes that the turbulent transport terms in the scalar transport equation can be modeled as:

$$-\overline{u_r' c'} = K(x,r)\frac{\partial \overline{c}}{\partial r}, \tag{2.29}$$

and

$$-\overline{u_x' c'} = K(x,r)\frac{\partial \overline{c}}{\partial x} \tag{2.30}$$

where $K(x,r)$ is a turbulent transport coefficient which scales with the macroscopic velocity scale U and macroscopic length scale L ($K \sim UL$).

With this turbulent transport coefficient $K(x,r)$ the transport equation can be written as:

$$U\frac{\partial \overline{c}}{\partial x} = \frac{\partial}{\partial x}\left(K(x,r)\frac{\partial \overline{c}}{\partial x}\right) + \frac{1}{r}\frac{\partial}{\partial r}\left(K(x,r)r\frac{\partial \overline{c}}{\partial r}\right). \tag{2.31}$$

For points far downstream from the injection point K becomes independent of the position (the mixing process is modeled as a purely diffusive process). In that case the mass transport equation has the following solution (e.g. Hinze (1975))

$$\overline{c(x,r)} = \frac{S}{4\pi\sqrt{x^2+r^2}K} e^{-U\frac{\left(\sqrt{x^2+r^2}-x\right)}{2K}}, \tag{2.32}$$

where S is the source strength of the point source.

In the case of $r \ll x$ this equation can be simplified to

$$c(x,r) = \frac{S}{4\pi K x} e^{-\frac{Ur^2}{4Kx}} \tag{2.33}$$

The diffusion coefficient becomes $K = \overline{u'^2}L/U$, with L a macroscopic length scale of the turbulence.

At the centerline (i.e. $r = 0$) concentration decays as $1/x$. The spreading of the plume is characterized by the second moment of the concentration profile which reads $\sigma^2 = 2Kx/U$. The spreading of the plume thus grows proportional to $\sqrt{x}$.

This equation is only valid if the travel time scale of a scalar fluid element that originates from the point source is greater than the time scale of the turbulence. When the travel time is smaller, the mixing process is not a diffusive process but a convective process. The turbulent transport coefficient K becomes a linear function of the travel time of the scalar in the flow. So the transport coefficient is also a linear function of the distance to the point source: $K = \overline{u'^2}x/U$. In that case the solution of the diffusion equation under assumption of small distances from the centerline and low turbulence intensities becomes (Hinze 1975):

$$\overline{c(x,r)} = \frac{SU}{2\pi(\overline{u_r'^2}\overline{u_\phi'^2})^{\frac{1}{2}}x^2} e^{\frac{-U^2}{2\overline{u_r'^2}}\frac{r^2}{x^2}} \tag{2.34}$$

As can be seen the centerline concentration now follows a $\frac{1}{x^2}$ decay and the spreading of the plume grows linear with the distance from the injection point.

Of course this model of the flow can give us only an approximation of the real concentration distribution. In reality the turbulence at the centerline of the pipe is not isotropic. Also the effects of the wall become important after some time.

Chapter 3

Measurement techniques

3.1 Introduction

In this chapter we describe the measurement techniques used in the present study. These measurement techniques are Particle Image Velocimetry (PIV), used for measuring the two in-plane velocity components in a light sheet, and Laser Induced Fluorescence (LIF), used for measuring two-dimensional concentration fields.

Besides the basic principles of PIV some attention is given to the problem of 'pixel locking' and the technique of 'window matching' which is used to improve the accuracy of the measurements.

For the LIF technique we describe the basic principles and the calibration procedure used for the measurements.

In the last section of this chapter we describe the features of the combined PIV-LIF measurement technique. The problems are identified that appear in combining the two measurement techniques. Furthermore we give the difference in resolution between the two techniques and the way to handle this difference.

3.2 Principles of PIV

The principle of PIV is that the flow velocity is measured by tracing the motion of small tracer particles present in the fluid. This can only be done if the particles are small enough so that they completely follow the fluid flow, but still large enough that they scatter enough light.

To be able to visualize the motion of the tracer particles the position of the particles illuminated in a thin sheet are recorded twice with a camera as sketched in figure 3.1. In the point-source measurements presented in this thesis the two recordings of a particle are stored in one frame. The result is a picture with doubly-

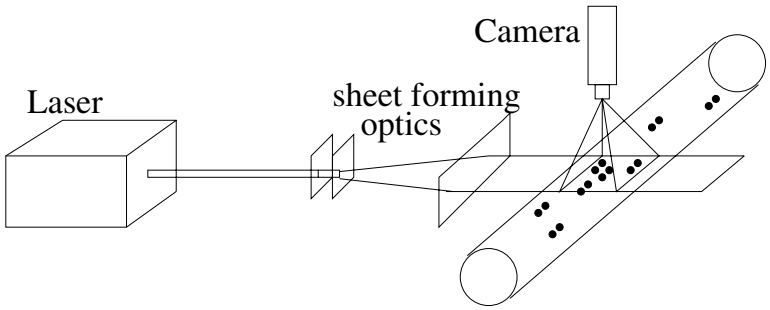

Figure 3.1: Sketch of the setup needed for PIV measurements.

exposed particles. From the displacement of the particles the fluid velocity can be estimated. In the jet-flow measurements the two exposures of the particles are recorded on two different frames. In that case a correlation of the two frames will give the particle displacements. An extensive description of the technique is given by Westerweel (1993).

3.2.1 Tracer particles

There are a number of requirements that the tracer particles must meet. These are

1. The particles must be small enough to follow the fluid motion completely.
2. The particles must be large enough to scatter enough light.
3. The particles must be homogeneously distributed over the light sheet.
4. The particles must not alter the fluid properties ort the flow (two fase flow effects).

Upper limit particle size
To follow the fluid motion completely implies that the slip velocity of the particles with respect to the fluid velocity must be small. In practice a sufficient requirement is that the slip velocity is small in comparison to the measurement inaccuracy. One of the characteristic parameters of the particles which determines the suitability of the particles, is the relaxation time constant, which gives the time that a particle need to adjust a sudden change in the velocity. When this time constant is small compared to the smallest time scale of the fluid motion the particle follows the flow completely (Adrian 1995). This time constant is obtained from a simple approximation for which the particle motion is supposed to be determined by Stokes drag only. For that case the particle motion is described by

$$\frac{\partial U_p}{\partial t} = \frac{1}{\tau_p}(U_f - U_p) \tag{3.1}$$

in which τ_p is the time constant of the particles. This time constant is defined as:

$$\tau_p = \frac{2\rho_p d_p^2}{9\rho_f \nu_f}, \tag{3.2}$$

with ρ_p is the density of the particles, ρ_f is the density of the fluid, d_p is the particle diameter and ν_f is the kinematic viscosity of the fluid. Equation (3.1) is true only if the density of the particles is much larger than the density of the fluid. In our case the density ratio is 2.7.

For the criterion that the time scale of the particles is much smaller than the time scale of the fluid τ_f, we can write:

$$\tau_f \gg \frac{2\rho_p d_p^2}{9\rho_f \nu_f}, \tag{3.3}$$

which leads to

$$d_p \ll \left(\frac{\tau_f 9\rho_f \nu_f}{2\rho_p} \right)^{1/2} \tag{3.4}$$

with the time scale of the fluid estimated as a typical length scale of the eddies divided by the rms of the velocity. As the length scale is estimated as $0.1D$ and the u_{rms} is estimated as $0.05\ U$, with U the mean velocity, the upper limit of the particle size becomes

$$d_p \ll \left(\frac{9D\rho_f \nu_f}{U\rho_p} \right)^{1/2} \tag{3.5}$$

Lower limit particle size
With requirement (3.5) the upper limit of the particle size is fixed. But if the particles are too small, they do not scatter enough light and are therefore not visible. This means there is also a lower limit on the particle size, depending on the optical arrangement of the setup, the sensitivity of the camera and the energy of the light source used to illuminate the particles. In practice the lower limit of the particles is given by $d_p > 1\mu$m since for particles smaller than 1 μm the scattering intensity decreases rapidly (Adrian & Yao 1984) (Adrian 1991).

particle distribution
The particles should be distributed homogeneously over the light sheet, in order to be able to make an unbiased estimation of the particle displacement by means of correlation techniques and to prevent too large differences in the number of particles in the interrogation areas (see section 3.2.2). The homogeneity of the particles over the light sheet depends strongly on the time constant of the particles as defined in (3.2). Particles with a large τ_f will tend to segregate in regions with

high vorticity. If particles are small enough to follow the flow accurately, they will also be homogeneously distributed over the light sheet. This is of course only true if the particles are added far enough upstream of the measurement position in order to let the turbulence mix the particles over the complete measurement volume. An alternative method, used in our case, is to have particles recirculate through the setup. After adding particles the setup should run for a sufficient long time to obtain a homogeneous distribution.

two fase flow effects

In order to prevent two fase flow effects due to particles added it is necessary that the volumer fraction of the particles is smaller than 10^{-6} (Elghobashi 1994).

3.2.2 Correlation technique

As mentioned above, in the point source measurements doubly exposed pictures are used to measure the flow field. In this case the displacement of the particles is estimated as follows. A small region of the doubly exposed picture is selected, called the interrogation window. In this interrogation window the autocorrelation of the particle positions is computed. This correlation is computed with help of a the Fast Fourier Transform algorithm. A graphical illustration of this autocorrelation technique is given in figure 3.2. The two dimensional autocorrelation looks in the ideal case as shown in figure 3.2c, as a function with three dominant peaks. (A more realistic result for the autocorrelation is given in figure 3.3.) The center peak represents the self-correlation of the particles. The two other peaks represent the correlation of the particle images in the first exposure with the particles in the second exposure, and visce versa. By moving the interrogation window over the complete image, the displacement field of the particle images over the image can be found. For a complete description of the autocorrelation technique, we refer to Adrian (1988).

To be able to compute the displacement of the particle images, the interrogation areas should obey the following criteria (Keane & Adrian 1990):

1. There should be enough particle images inside the interrogation area. In the case of one particle in the interrogation area the displacement is clear. For 2 particles however the displacement is ambiguous. In general the signal to noise ratio is increasing with an increasing number of particles present in the interrogation area. The number of doubly exposed tracer particles inside an interrogation window, needed to be able to compute an autocorrelation function with a 95% valid detection probability is about 8 (Keane & Adrian 1993). This can be achieved by a sufficiently large particles concentration in combination with a sufficiently thick light sheet.

2. The differences in the displacement for the different particles inside the interrogation area should be small. For large differences which e.g. may due to

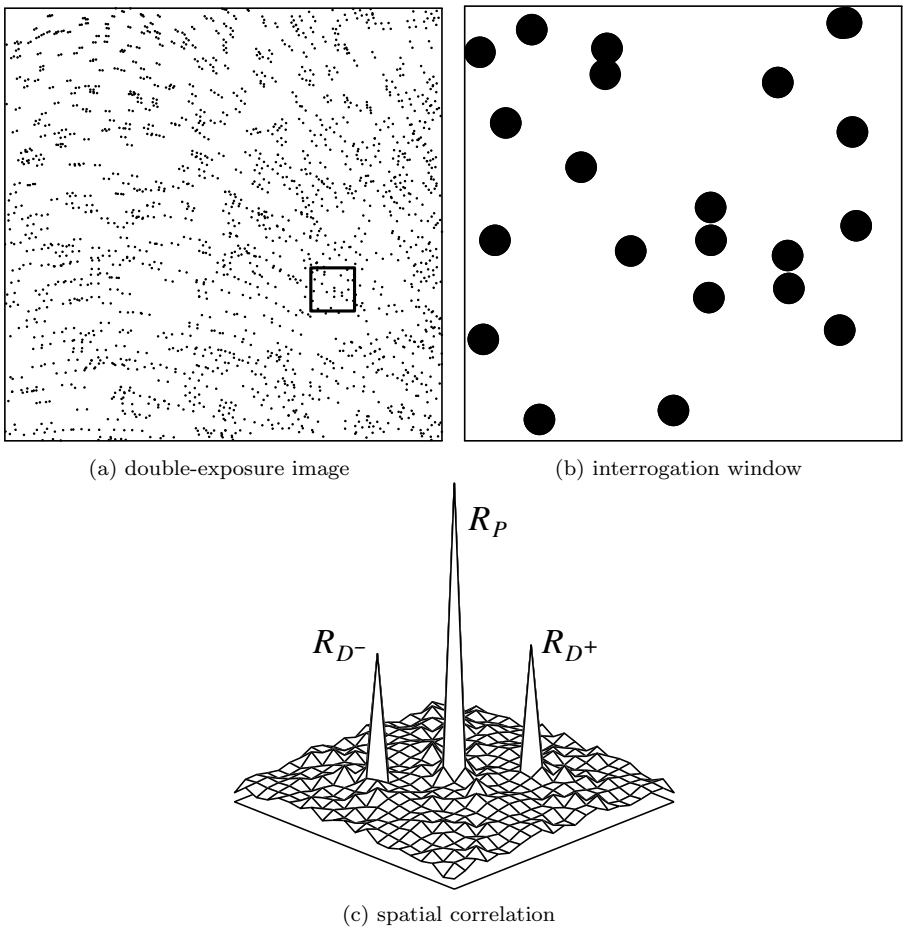

(a) double-exposure image (b) interrogation window

(c) spatial correlation

Figure 3.2: Interrogation analysis for a double-exposure PIV image. The location of the displacement-correlation peak R_{D^+} yields the in-plane displacement of the particle images within a small interrogation window. From: Westerweel (1993).

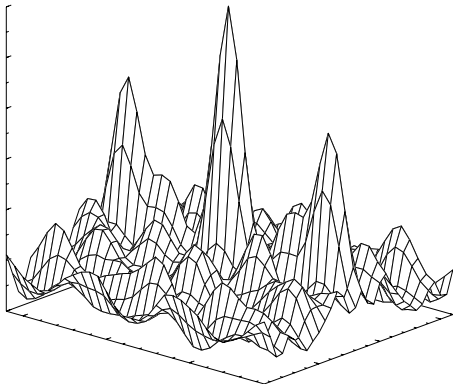

Figure 3.3: A measured autocorrelation function from a PIV interrogation window (from: Aanen (1995)

an inhomogeneous flow field, the correlation peak becomes wider, and therefore harder to detect. Besides that there is a bias to smaller displacements in the interrogation areas, since the the probability for a particle with a small displacement to be doubly exposed is larger than for a particle with a large displacement. This requirement implicates that the size of the interrogation window should be chosen such that (Keane & Adrian 1993).

$$M|\Delta u|\Delta t/d_\tau < 1, \tag{3.6}$$

with M the magnification of the camera system, Δu the velocity difference in an interrogation area, Δt the time delay between the two exposures and d_i the size of the interrogation area in the object plane and d_τ the particle image diameter. This restriction means that the differences in particle displacement should be less than one particle image diameter. For larger differences the correlation peak becomes too wide. To know if this condition is fulfilled an estimation has to be made of the velocity gradients in the flow. In the case of a turbulent pipe flow these restrictions are not satisfied near the wall, where turbulent intensities are high and the velocity gradients are large.

3. The number of particles which are exposed only once inside the interrogation area should be small. These particles add only noise to the correlation computed. To fulfill this last requirement, two different points are important:

- The displacement of the particles should be smaller than 0.25 times the size of the interrogation area. If the displacement of the particles is too large with respect to the size of the interrogation domain, too many particles move out of the interrogation area in between the two exposures. This can be prevented by choosing the proper time delay between the two exposures.
- The number of particles that is exposed only once due to out-of-plane motion should be small. Together with the thickness of the light sheet, this gives a criterion for the velocity component perpendicular to the light sheet. In the case of a turbulent pipe flow with a light sheet in the streamwise direction on the centerline of the pipe, the mean out-of-plane motion is zero. The maximum out-of-plane displacement should be smaller than 0.25 times the thickness of the light sheet. The maximum velocities in the direction perpendicular to the light sheet, determined by the tangential component of the turbulence intensities, are estimated to be 0.1 times the mean velocity. So the number of out of plane particles is small enough if:

$$\Delta t \ll 2.5\frac{\delta y}{U}, \tag{3.7}$$

  with δy the thickness of the light sheet. With a light sheet of 0.4 mm and a mean velocity of 0.1 ms, the maximum time delay becomes 10 ms.

If these criteria are not obeyed, it is not possible to reliably detect the correlation peak connected to the particle image displacement. In that case some other peak will be selected, causing a wrong estimation for the velocity. The result is a so-called "outlier" or spurious measurement of the velocity field.

Cross-correlation measurements For the jet-flow measurements the auto-correlation technique described can not be used, because especially near the sides not all particles have a positive displacement. Particle images may overlap and no distinction can be made between positive and negative displacements. To solve this problem, the two exposures are recorded on two different frames. The displacement is now estimated by means of a cross correlation between two corresponding interrogation areas of the two frames. In a cross correlation the peaks R_p and R_{D^-} which appear in the autocorrelation (see figure 3.2) vanish, and only the R_{D^+} peak remains. An overview of the theory of cross-correlation analyses of PIV images is given in Keane & Adrian (1993).

3.2.3 Sub-pixel displacement

The recording of the particle image is done by a CCD camera. The method PIV in which CCD cameras are used to record particle images, is often referred to as

Digital Particle Image Velocimetry (DPIV). One of the first applications of DPIV is described by Willert & Garib (1991). The typical resolution of a modern CCD-camera is 1000×1000 pixels. Cameras with much larger CCD-chips are available, but with CCD-chips with more pixels the measurement frequency goes down due to a limited speed of the data readout. This frequency is limited to a maximum speed of about 20 MHz. The speed of the cameras can be increased by using parallel read-outs. The Kodak ES 1.0 used has a parallel read-out for the odd and even lines. Cameras with more read-outs are available (but at the moment still very expensive).

The size of the interrogation window is typically 32×32 pixels. This size is a compromise between spatial resolution of the velocity field and the measurement reliability in estimating the particle displacement. With a 50% overlap between the interrogation windows displacement vectors can be found on a 16×16-pixel grid. As described in section 3.2.2, typical particle image displacements should be at most one fourth of the size of the interrogation windows, so in our case 8 pixels. To increase the measurement resolution of a CCD camera the displacement of the particles is estimated on a sub-pixel scale (Willert 1989). This is done by fitting a function, e.g. a Gaussian though the correlation peak representing the particle image displacements. To be able to do so the peak should cover more than one pixel. In our case a three-point estimator is used:

$$\hat{\epsilon} = \frac{\ln \hat{R}_{-1} - \ln \hat{R}_{+1}}{2(\ln \hat{R}_{-1} + \ln \hat{R}_{+1} - 2\ln \hat{R}_0)}, \tag{3.8}$$

in which $\hat{\epsilon}$ is the estimated fractional displacement, $\hat{R}_0$) is the value of the correlation peak, $\hat{R}_{-1}$) is the value of the correlation for a displacement one pixel less than the displacement peak and $\hat{R}_{+1}$) is the height of the correlation for a displacement one pixel larger than the displacement peak. A Gaussian peak fit is used because of the fact that the peaks have approximately a Gaussian shape. Therefore a fit with a Gaussian peak will give a better estimation of the real position of the peak in comparison with other three-point estimators like the center-of-mass estimator or the parabolic-fit estimator (Westerweel 1993).

3.2.4 Pixel locking

As mentioned in the previous section, a Gaussian fit to estimate the sub-pixel displacement is valid only if the displacement peak in the auto- or cross-correlation function has a Gaussian shape. Under certain conditions, the sub-pixel displacement estimation is biased towards integer pixel displacements or, under certain circumstances, to even pixel displacements. In the following we consider these two types of bias in more detail.

Pixel locking to integer pixel displacements

The first type i.e. bias towards integer pixel displacements appears when the images

of the particles on the CCD chip become too small with respect to the pixel size. In the most extreme case, the particle images are only one pixel wide. In that case the correlation peak is not a Gaussian anymore but tends to a delta peak of one pixel wide, especially when the number of particles inside an interrogation area is small. Since the three-point estimator used needs the values of the correlation on the pixels next to the peak, it will fail in the case of a delta peak. The estimated fractional displacement will be close to zero, and pixel locking will occur. Prasad *et al* (1992) showed minor pixel locking problems at particle image sizes of 3.8 pixels and severe pixel locking at particle image sizes of 1.9 pixels, using a center-of-mass estimator for the fractional displacement.

In order to know if in a setup pixel locking will occur, the size of the particle images with respect to the pixel size should be computed. The size of the particle images is determined by the size of the particles and the optical recording system. The image diameter d_t of a particle with diameter d_p can be approximated with:

$$d_t^2 \approx M^2 d_p^2 + d_s^2, \tag{3.9}$$

where M is the image magnification of the optical system, d_s is the diameter of the diffraction limited spot, given by:

$$d_s \approx 2.44 \frac{\lambda z_0}{D}, \tag{3.10}$$

where λ is the wave length of the light, z_0 the image distance and D the diameter of the lens (Goodman 1968). The image distance can be determined from the focal length f of the lens used and the magnification with:

$$z_0 = (M + 1)f \tag{3.11}$$

The first term in (3.9) is due to the geometric image of the particle. The second term is a contribution due to diffraction. For systems with small particles and low image magnification, the diffraction diameter is dominant. In the present experiments typical values for the relevant parameters are: $M = 0.25$, $d_p = 5\mu$m, $\lambda = 532$nm, $f = 55$mm, f/D=8, so $Md_p = 1.25\mu$m and $d_s = 13\mu$m. Clearly $d_\tau \approx d_s$. This means that the size of the particle images is almost independent of the exact particle diameter and strongly depending on the aperture of the lens. The size of the pixels in the cameras used is about 9 μm. This is only 1.4 times smaller than the estimated particle image diameter, so some peak locking is expected.

An example of a particle displacement histogram with pixel locking is given in figure 3.2.4. In this figure the particle displacement histogram of measurement series P2 to be presented in chapter 5 is shown. The preference for (nearly) integer values of the displacement is clear.

One of the parameters determining the sensitivity for pixel locking is the fill ratio of the camera used. The fill ratio of the cameras is the ratio between the

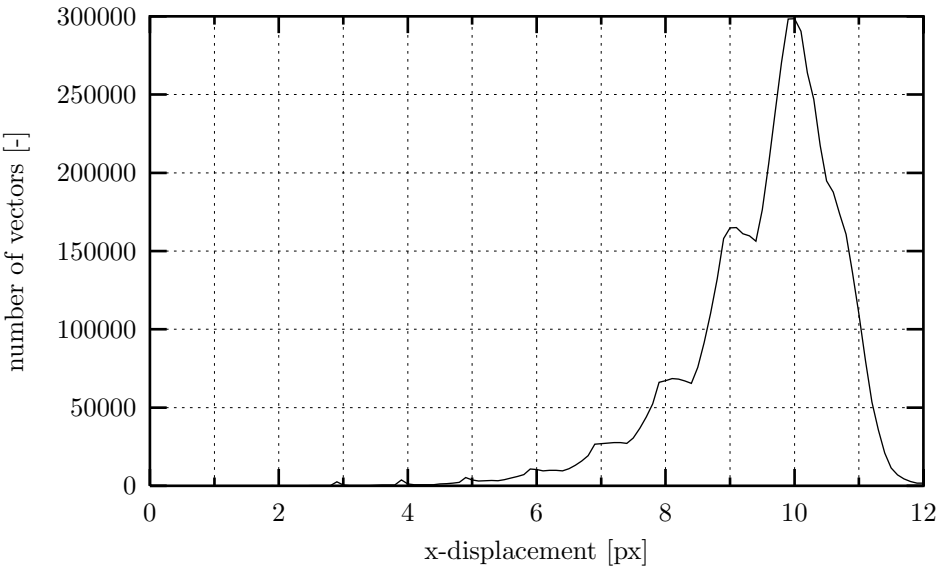

Figure 3.4: The particle displacement histogram of measurement series P2

light sensitive area of a pixel of the camera, and the distance to neighboring pixels in horizontal direction multiplied by the distance in vertical direction. The ratio between the area of one of the grey squares denoting the light sensitive area of a pixel and the open squares in figure 3.5 being the total area occupied by one pixel denotes the fill ratio. As said before the sub-pixel estimator used is a three point

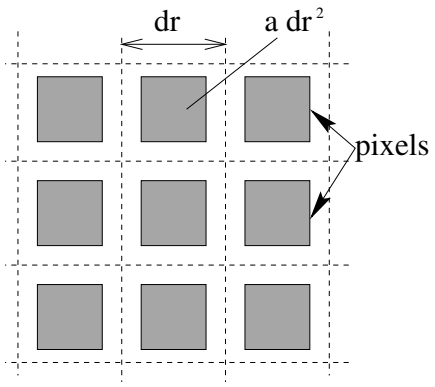

Figure 3.5: Schematic view of the light sensitive parts of the camera.

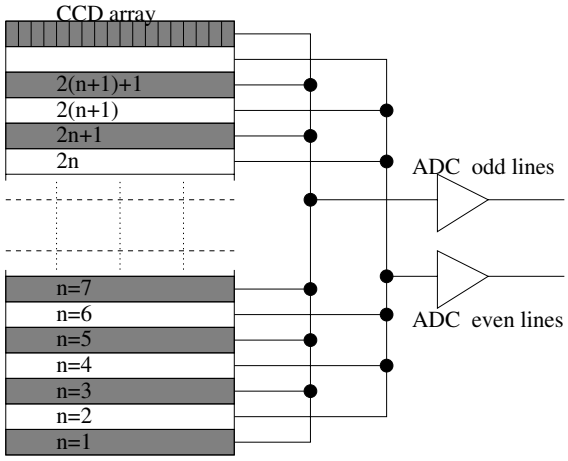

Figure 3.6: A sketch of the read-out system of the cameras. The odd and the even lines are read out by two separate A to D converters.

estimator. For cameras with small fill ratio the image of a particle has to be larger compared to cameras with a high fill ratio, in order to cover three pixels of the camera.

Pixel locking to even pixel displacements

The second type of pixel locking is caused by the fact that for the CCD cameras used in our experiments the odd and even lines are read out by two different analog to digital converters (see figure 3.6). Due to small differences in the electronic devices used this causes a small difference in output between the odd and even lines as response to a given amount of light. The result is that the mean grey value of the odd and even lines are not equal. Due to the difference in mean grey value the autocorrelation functions of the interrogation areas show peaks at even pixel positions. These differences are minimized by the possibility to apply a different gain and offset to the different A to D converters. Since the offset and gain can be changed with discrete steps only there will always remain a small difference between the odd and even lines. The resulting differences in sensitivity between the odd and even lines causes pixel locking at even pixel displacements if the differences in grey values become too large. This is shown figure 3.7 where the measured displacement histograms of a rotated artificial particle field, with an increasing imposed difference in grey value between odd and even lines are plotted. The 'particle field' consists of a paper with randomly distributed spots on it. By rotating the paper over a small angle the dots get a displacement proportional to the distance from the rotation point. As can be seen the original vertical displacement histogram shows an almost

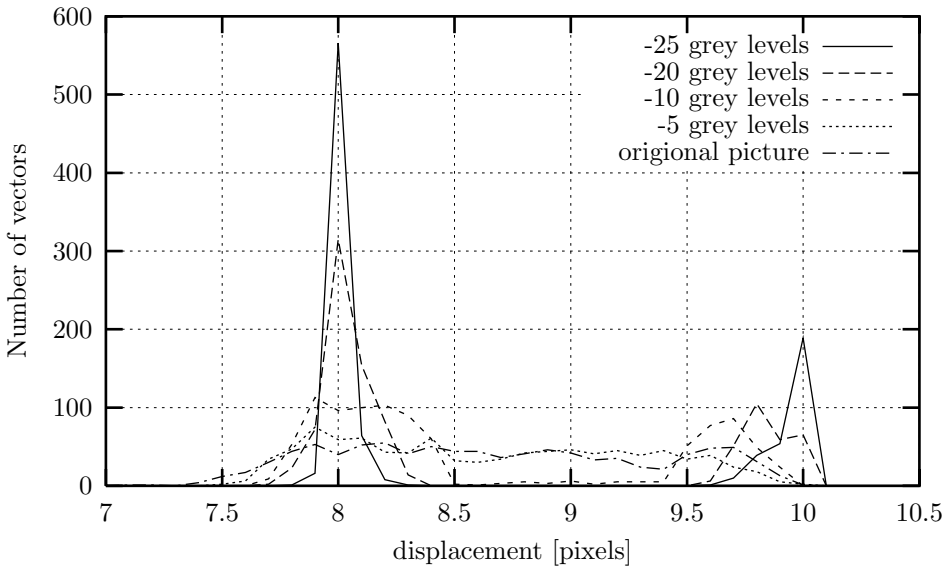

Figure 3.7: The effect of a constant difference in grey values between odd and even lines (from Telesca 1998).

flat distribution as expected from the imposed displacement. The flat distribution is caused by the fact that the vertical displacement of the particles is a linear function of the the horizontal distance from the rotation point. Using an image processing package an offset is given to the grey values of the odd lines. The displacement of the dots is computed for the edited pictures. With an increase of the difference between the odd and even lines of 5 grey values no severe pixel locking occurs. With an increase of 10 grey values however severe pixel locking occurs.

3.2.5 Outliers

Due to fluctuations in the local seeding density, the presence of large particles and other disturbing factors not all displacements are measured correctly, causing so called outliers to appear in the measured flow field (see section 3.2.2).

To detect outliers, each estimated displacement is compared with the median of the 8 (or less for the positions at the edge of the pictures) neighboring displacements. An extensive description of this technique is given Westerweel (1993). If the displacement deviates more than a given threshold value from this median, the discard level it is supposed to be an outlier. Outliers are replaced with the average displacement of their neighbors. The discard level used is determined by computing the number of discarded vectors as function of the threshold value. Below a certain

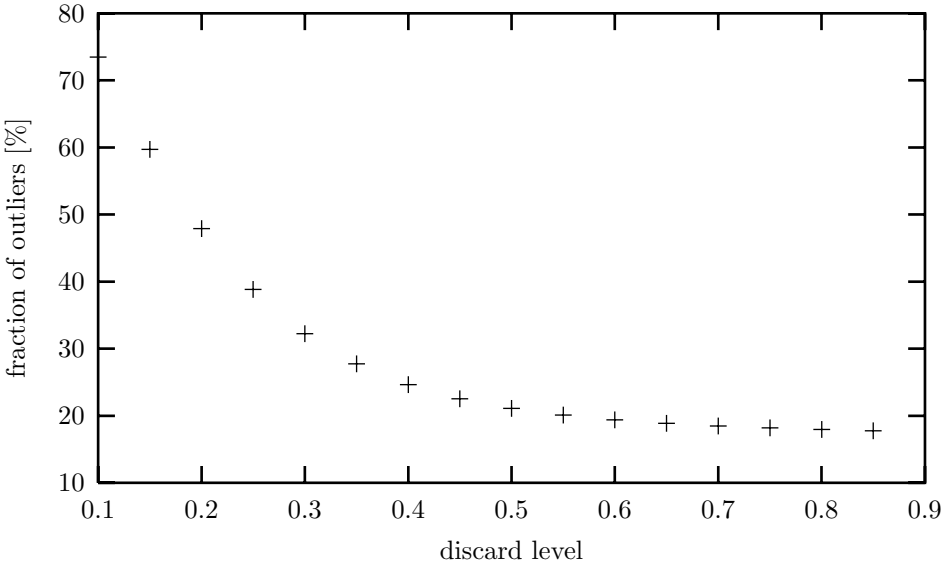

Figure 3.8: The fraction of discarded vectors as function of the threshold value for the deviation of the mean for a single frame of low quality.

discard level the velocity fluctuations present in the flow start to be larger than the discard level, causing the number of discarded vectors to increases rapidly. An example of number of discarded vectors as function of the discard level for a picture with a low particle density, resulting in a high number of outliers, is given in figure 3.8. The number of discarded vectors remains almost constant above a discard value of 0.6. The discard level used, was chosen just above this value. Looking at the resulting discarded vectors, we found this procedure detected most of the wrong vectors. The spurious vectors that were not detected by this choice do not have any measurable influence on the statistics of the mean and rms-values of the velocity statistics. They probably have influence on velocity gradient based quantities like the deformation.

3.2.6 Window matching

To reduce the amount of outliers and the uncertainty in the sub-pixel estimator we have used window matching (Westerweel *et al.* 1997). To be able to apply window matching, a first guess of the velocity field has to be estimated by mean of the normal procedure. After that a second estimate can be made by doing a cross correlation on the double exposed frame between two interrogation areas which have a shift with respect to each other, equal to the displacement computed with

the normal autocorrelation technique (see figure 3.9). The effect of this window matching technique on the measurement accuracy is described by Westerweel *et al.* (1997). The results improve in two ways.

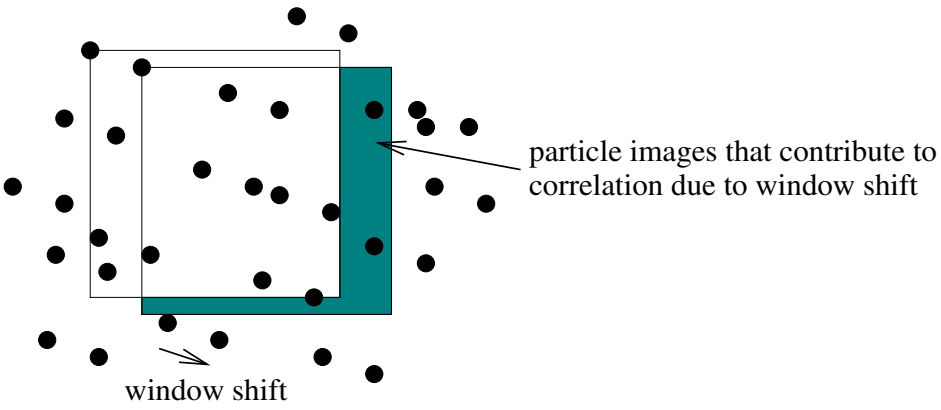

Figure 3.9: The principle of window matching.

First, due to the shift the loss of pairs will be reduced significantly. In the first exposure all particles with a distance less than the particle displacement from the right edge from the interrogation window (in the case that the displacement is purely to the right) will move out of that window during the time interval in between the exposures (Keane & Adrian 1993). In the case of window matching, the second exposure of the particles is captured in the shifted frame (the grey area in figure 3.9).

The second improvement is that the standard deviation of the error in the displacement estimated by a cross correlation reduces significantly. If the shift chosen is accurate, the displacement of the particles with respect to the shifted window is always less than half a pixel. In that case the error reduces strongly, as shown in figure 3.10 (Westerweel 1999). The effect of window matching can be seen in figure 3.11 in which two vector plots are shown. The upper vector plot shows the particle displacement relative to maximum value of the mean velocity profile, after replacing outliers without window matching. The lower vector plot gives the same displacements, but now when window matching is applied. To obtain the shift as accurate as possible, the velocity field is checked for outliers which are replaced in the usual way. As can be seen the lower plot looks much more regular and contains less outliers as the upper plot. This is caused by a significant noise reduction resulting from the window shifting and not by any smoothing.

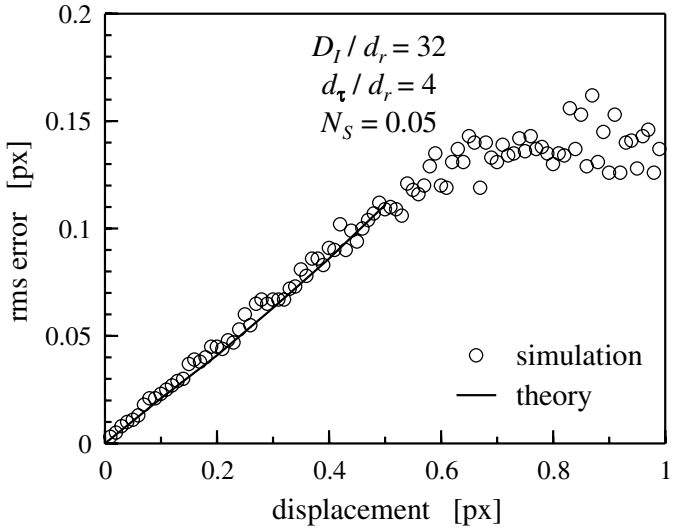

Figure 3.10: The standard deviation in the estimation of the displacement as function of that displacement. Both the results of a simulation and a theoretical curve are shown (from Westerweel (1999).

3.2.7 PIV procedure and data statistics

The procedure used to compute the velocity fields of the point source measurements that we will show later in this thesis, becomes:

1. select the interrogation areas in the PIV frames for all desired positions
2. compute the autocorrelation for each interrogation area
3. determine position of the displacement peak for each interrogation area
4. Remove outliers with median technique (use linear interpolation to replace discarded vectors)
5. compute cross-correlation with a shifted interrogation window, using the results of step 2 for the image shift
6. determine position of the displacement peak for each interrogation area
7. Remove outliers with median technique

For the jet measurements the same procedure is followed, using a cross-correlation between two single exposed frames in stead of an autocorrelation in step 2.

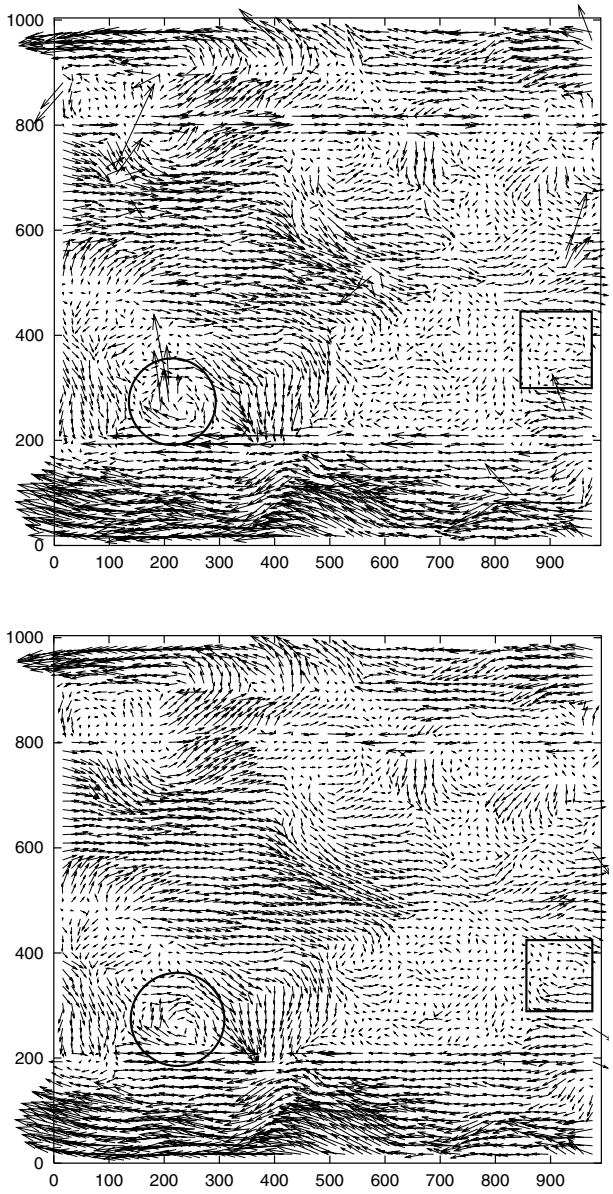

Figure 3.11: The effect of window matching on the relative displacement vector fields. The upper plot is computed without window matching, the lower plot is computed with widow matching. In the plot with window matching less outliers are present (see circles) en more structure can be seen (see squares)

From obtained velocity fields the mean velocity can be computed by recording PIV images over a sufficient long time and by taking the average of the particle displacement for each measurement position. If the velocity field is independent from the streamwise direction, an average over that direction can be made in order to decrease the statistical error. The turbulence intensities for each point can be computed by subtracting the measured mean displacement from the displacement value at that point and compute the rms of these residuals. The local turbulent stresses can be computed by multiplying the fluctuating part of the displacement in the streamwise and the radial direction and average in time and if possible in the streamwise direction. For the scaling from pixel displacements to velocities we refer to 4.5.6.

3.3 Principles of LIF

3.3.1 Fluorescence

Laser Induced Fluorescence (LIF) is a well-known technique which is often used in visualization experiments. However, if the experiments are done carefully, it is possible to do quantitative concentration measurements with the technique. A very good description of the principles of the technique is given by Walker (1987). He describes a one-point measurement system, but the principles used in the present measurement system are the same. Therefore, we give here only a brief description of the technique.

The technique is based on the physical property of certain organic molecules, that an electron in the outer orbit can be exited. It moves from one of the vibrational levels of the ground state into the so-called singlet state. This exited electron can fall back into the ground state along several paths as shown in figure 3.12. In the case of fluorescence the electron first goes to the lowest energy level of the singlet state. This is called the Stokes shift. Thereafter, it falls back to the ground state under emission of a photon. The time in between absorption and emission is about 10^{-4} ms. This time interval is long enough to give the molecule a random orientation with respect to its orientation during absorption. The emitted light therefore is polarized randomly. There is some loss of energy between absorption and emission and therefore the wavelength of the emitted light is slightly longer than the wavelength of the absorbed light. The lost energy is transformed into heat. The probability with which the electron is exited when a photon is absorbed by the molecule is strongly dependent on the species and the wavelength of the incoming light. In our case fluorescein [$C_{20}H_{14}Na_2O_5$] is used. The structure of the fluorescein is given in figure 3.13. Another name for fluorescein is Uranine AP. The absorption and emission spectra for fluorescein are shown in figure 3.14. The maximum absorption occurs at a wavelength $\lambda = 488$ nm, whereas the maximum of the emission peak is positioned at $\lambda = 515$ nm. Fluorescein is very useful as a dye

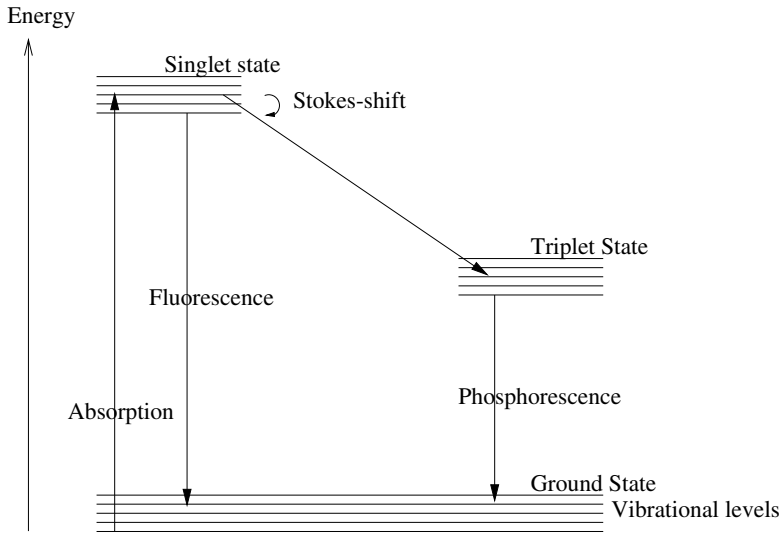

Figure 3.12: The vibrational levels of an electron relevant for fluorescence (Walker 1987).

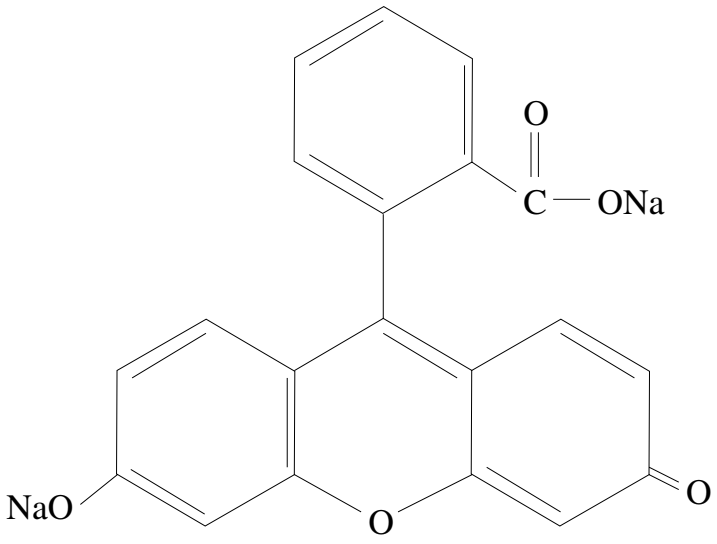

Figure 3.13: The molecular structure of fluorescein.

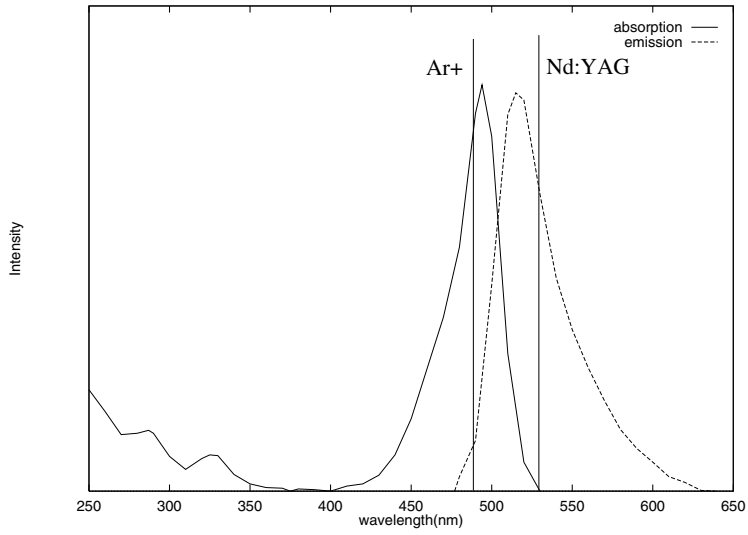

Figure 3.14: The absorption and emission spectra fluorescein (Miller 1981). Beside the spectra also the wavelengths of the light emitted by the Argon-ion and the YAG laser are denoted.

for our experiments. Because under certain restrictions to be discussed below, the amount of light emitted depends linearly on the concentration of the dye for a quite wide range of concentrations (Buch 1995) (Walker 1987). Besides that the intensity of the emitted light also depends linearly on the intensity of the incoming light if the light intensity is not too high (Walker 1987). Another important property of fluorescein is that the frequencies of the emitted light lie in the visible part of the electromagnetic wave spectrum. In figure 3.14, besides the absorption and emission spectra of fluorescein, we have also indicated the wave lengths of the 488 nm line of an Argon-ion laser and the 532 nm line of a frequency doubled Nd:YAG laser. The 488 nm line is positioned almost at the peak of the absorption spectrum of fluorescein. This line is therefore very useful as light source for LIF experiments. The reason that the 532 nm is drawn, is that this wavelength is used for the PIV experiments. The absorption of light with this wavelength is almost negligible. This means that the fluorescein is expected to be not visible in the PIV frames. The Argon laser should be blocked during PIV exposures, since no distinction can be made by Nd:YAG-light reflected by particles and light emitted by fluorescein.

absorption

Due to the absorption of light, the light intensity of a laser beam I_l passing a volume with a concentration c will decay. The decay is proportional with the concentration

and the light intensity, so that it can be modeled with:

$$\frac{dI_l}{dx} = -\epsilon c(x) I_l, \tag{3.12}$$

in which ϵ is the extinction coefficient. For wide range of concentrations (more then 5 decades) and not too high light intensities this model gives an accurate description of the light absorption by fluorescein. For high light intensities saturation occurs, i.e. nearly all fluorescein molecules in the beam path are exited and the fluorescence intensity becomes independent of the light intensity. Walker (1982) has measured no saturation at laser power up to 300 mW with a beam focussed with a 220 mm lens. The extinction coefficient of fluorescein for light with a wavelength of 488 nm at room temperature and at a pH=9 is 8.51×10^3 m^2/mol.

The concentration of the dye can be a function of position along the beam. In case of a uniform concentration the intensity of the beam decays as

$$I_l = I_0 e^{-\epsilon c x}. \tag{3.13}$$

In the case of a non-uniform concentration the solution changes to

$$I_l = I_0 e^{-\epsilon \int c(x)\, dx}. \tag{3.14}$$

Only a fraction of the light absorbed by the fluorescein molecules is emitted afterwards. The rest is dissipated into heat. The ratio between the amount of absorbed and the amount of emitted light is the quantum yield. From 3.12 the amount of light emitted per volume unit can be written as

$$I_e = \varphi \epsilon I_l c, \tag{3.15}$$

with φ the quantum yield ranging from 1 under ideal circumstances to 0 for e.g. low pH values. As can be seen there is a linear relation between the intensity of the incoming and emitted light. The amount of light emitted by the dye per unit volume can now be written as

$$I_e = \Psi I_l c, \tag{3.16}$$

with Ψ a constant depending on a number of factors, e.g. pH-value, wavelength of the incoming beam and temperature.

In the case of very dilute fluorescein solutions or only a small volume fraction of high concentration of fluorescein, the absorption is small. As soon as the total absorption in the experiment is smaller than the measurement error, absorption can be neglected. In our case the LIF images are recorded with a CCD camera with 256 grey values. Together with the noise in the camera which is in the order of one grey value (see section 4.5.3), this leads to a statistical error of about one percent, since this error occurs in the measurements and in the reference frames for the background image and the reference frame for the light intensity distribution of the light sheet.

3.3.2 Calibration

To be able to do quantitative concentration measurements with LIF, some practical problems have to be solved.

In the measurements presented here, we have used planar LIF. This means that we have not used a single incoming light beam with an easy to measure intensity, but 2D light intensity distribution over the light sheet. Besides that the measurements are done with a CCD camera. The geometry of each pixel is slightly different, so that for each pixel a different offset and proportionality constant has to be determined in order to make quantitative measurements. Differences in offset are in our case typically 1 grey value. The rms on a black image due to thermal noise is also typically 1 grey value. Differences in slope of the grey values with increasing light intensity are in the order of 1%. The differences in intensity of the light sheet have a much larger impact on the calibration of the LIF technique. The measured intensities of the laser sheet show a spreading of about 15 %.

The offset grey values of the cameras was determined by recording 50 frames with no fluorescein added to the flow. During recording the Argon laser was switched on and the exposure time of the cameras was set equal to the exposure time during the measurements. This was done to be able to subtract a possible background due to scattered light. In practice the difference between an image, recorded with the lens of the camera covered, and the recorded background images was negligible.

To determine the light intensity distribution of the laser light sheet, part of the setup was filled with a uniform fluorescein concentration as described in section 4.3.1. From this concentration a series of 50 frames was recorded with an exposure time of 25 ms. The diafragm of the lens during these recordings was the same as used during the measurements. We used such a long exposure time in order to be able to use a low concentration which is needed to prevent errors due to absorption. The average of these 50 frames was used as light intensity distribution of the light sheet. In figure 3.15 the grey value averaged over pixel rows (figure 3.15b) and pixel columns (figure 3.15a) of the resulting intensity distribution at measurement position P2 are show. The variation of the measured light intensity in vertical direction is caused by the optical configuration of the setup, like refraction by the tube. Clearly the differences between the odd and even lines, caused by the CCD cameras can be seen. The disturbances in the horizontal direction are caused by impurities on the sheet forming optics, the light distribution over the laser beam and particles sticking to the bottom of the pipe measurement section.

In the calibration of the frames the absorption of incoming light by the fluorescein present in the uniform concentration frames is not taken into account. Also in the measurement series the effect of absorption is neglected. The reason for that is that the error due to the correction for absorption is much larger than the maximum error due to absorption. This is caused by the fact that if a small error is made in the correction, the error in the result grows exponentially along the light ray. The

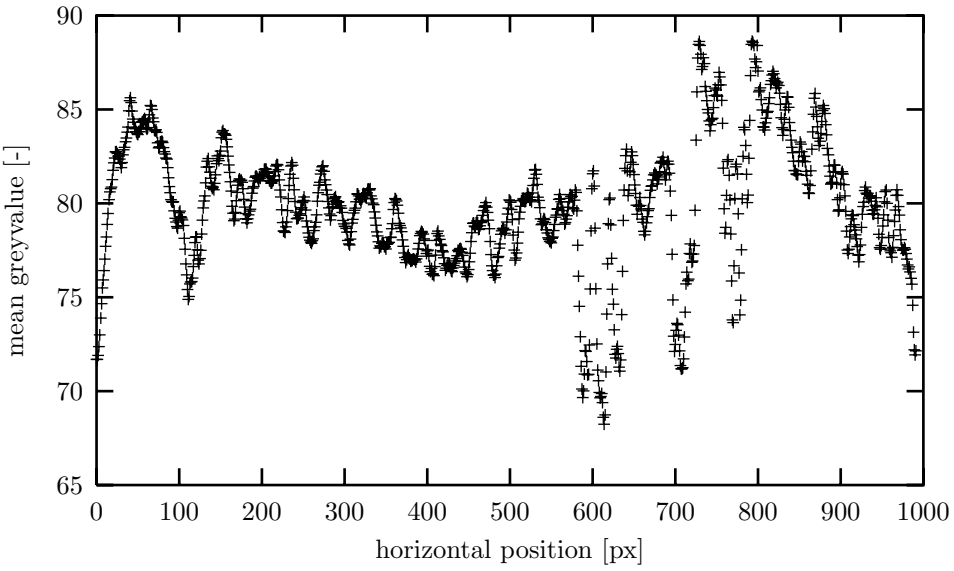

(a) horizontal profile

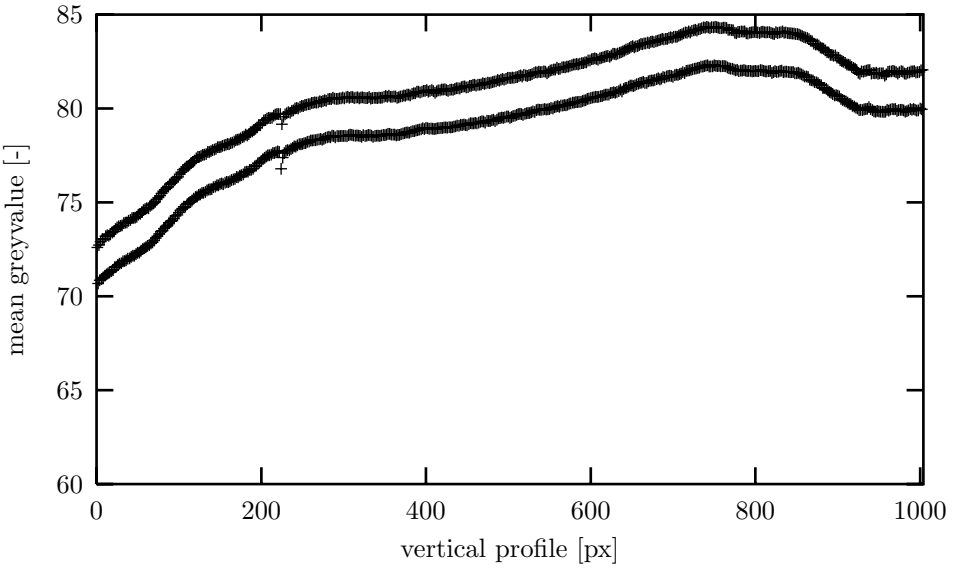

(b) vertical profile

Figure 3.15: The horizontal (a) and vertical (b) light intensity distribution of the uniform concentration pictures for measurements P2.

cameras that were used have 1004 lines, so an error of 0.01% for each line leads to an error of more then 10 % in the last pixels of the columns of the images. In the case of no correction, even in the case that the total amount of injected fluorescein is captured in a single frame, the extinction due to absorption by the fluorescein is only in the order of 1 percent.

3.3.3 Low-pass filter

If the scalar dissipation is computed, the gradient of the concentration field has to be computed on a pixel-to-pixel base. In doing so, the thermal noise in the pictures causes a high error level in the scalar dissipation fields. To remove this short wavelength noise, we apply to the concentration pictures a low pass filter. The filter used has the following form (Lele 1992):

$$\widetilde{c_n} = a_3 c_{n-2} + a_2 c_{n-2} + a_1 c_n + a_2 c_{n+1} + a_3 c_{n+2}, \tag{3.17}$$

with $a_1 = 10/16$, $a_2 = 4/16$ and $a_3 = -1/16$, $\widetilde{c_n}$ the resulting concentration at position n, and c_n the initial concentration at position n. This filter has a very sharp cut-off frequency. It therefore does not influence the larger scales. The frequency response of the filter is shown in figure 3.16 Since the filter is one-dimensional and our data fields are two-dimensional, it is applied first in the horizontal direction and then in the vertical direction. When a dissipation histogram is made, it follows that the noise peak moves significantly to lower values when filtering is applied while the maximum level of dissipation is not influenced. An example of the scalar dissipation pdf of a single LIF frame with and without filtering is shown in 3.17.

3.4 Combined measurement technique

In combining the two measurement techniques of PIV and LIF a few additional problems arise. Most of them are technical and are solved by using the correct hardware. They will be described in chapter 4. But there remains one problem with has to be treated first. As is clear from the description of the two measurement techniques given above, there is a difference in spatial resolution between PIV and LIF. Using a 32×32 pixel interrogation window, combined with a 50% overlap, the grid spacing of the PIV measurements is 16 pixels. LIF on the other hand gives concentration data at each pixel. We need this difference in resolution, because there is also a large difference in the smallest length scale between the concentration and the velocity field, as explained in section 2.2.1. The question arises how to treat this difference in resolution during computing the scalar flux terms in equation 2.23. The turbulent transport terms in the mass transport equations can be written in two ways. The first is the formulation as a real transport term, i.e. the correlation between velocities and concentration gradients. Second, with help of continuity, it

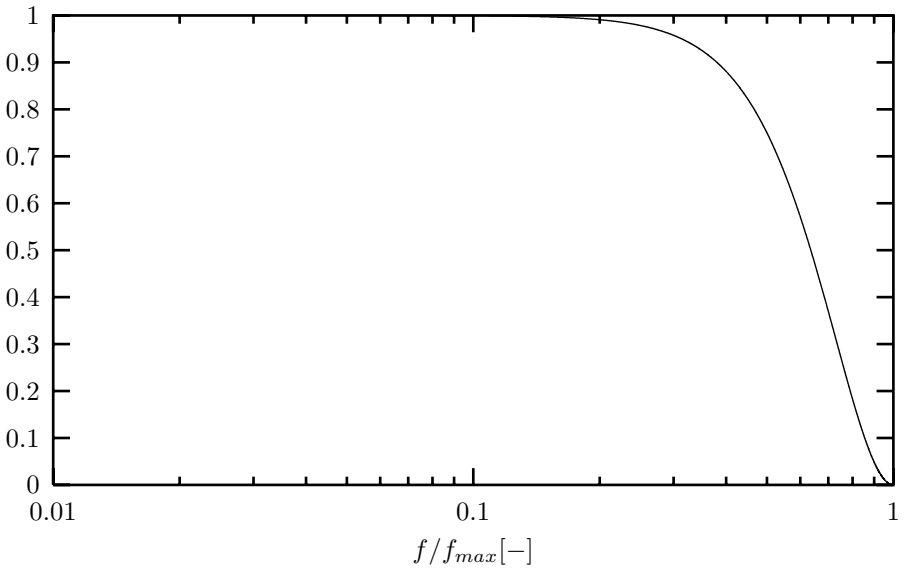

Figure 3.16: The spectrum of the low pass filter used. The frequencies are scaled with the maximum frequency, determined by the grid spacing.

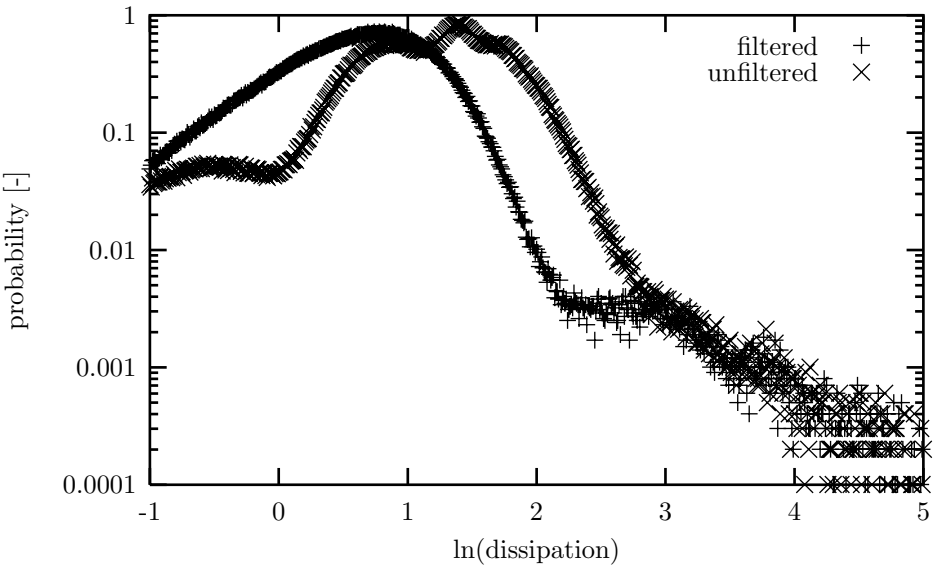

Figure 3.17: The pdf of the logarithm of the scalar dissipation of a single LIF frame with and without filtering.

can also be written as the spatial derivative of the correlation between concentration and velocities:

$$\overline{u'\frac{\partial c'}{\partial x}} \text{ or } \frac{\partial \overline{u'c'}}{\partial x}. \tag{3.18}$$

The computation of these terms can be done in two ways. The first one is to interpolate the velocity data on the same grid as the LIF data, multiply u' and c' and then do an ensemble average over all recorded image pairs and then take the spatial derivative. The second one is to average the LIF data on the PIV grid, do the correlation and then do the ensemble average. A sketch of the two methods is given in figure 3.18, in which a concentration signal, a velocity signal and the linear interpolation of the velocity in between the measurement points are shown.

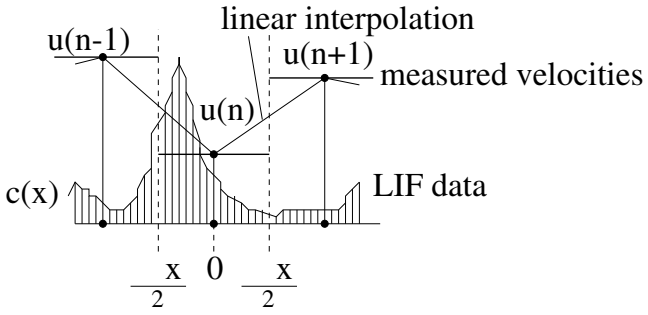

Figure 3.18: A sketch of the difference in resolution of the PIV and the LIF measurements.

Difference between averaging LIF data and interpolating PIV data
If we average the LIF data over an interrogation region, we can examine the difference between the two term in (3.18). between the two terms in (3.18). The first term in (3.18) works out as:

$$\left\langle u\widetilde{\frac{\partial c}{\partial x}} \right\rangle \tag{3.19}$$

with a tilde denoting an average over an area with the length of the grid spacing Δx of the velocity field, and $< a >$ denoting the expected value of variable a. Evaluating this equation around the position n leads to

$$\left\langle \frac{u_n}{\Delta x}\frac{\partial}{\partial x}\int_{-\Delta x/2}^{\Delta x/2} c dx \right\rangle \tag{3.20}$$

The integral and the differentiation cancel each other, so this can be written as

$$\left\langle \frac{u_n}{\Delta x}\left(c_{\Delta x/2} - c_{-\Delta x/2}\right)\right\rangle = \frac{\left\langle u_n c_{\Delta x/2}\right\rangle - \left\langle u_n c_{-\Delta x/2}\right\rangle}{\Delta x}. \tag{3.21}$$

If we average the LIF data over an interrogation region the second term in (3.18) works out as:

$$\left\langle \frac{\partial \widetilde{uc}}{\partial x} \right\rangle = \frac{\partial \langle u\tilde{c} \rangle}{\partial x} \tag{3.22}$$

Evaluating this equation around the grid position x_n this leads to

$$\left\langle \frac{(u_{n+1}\tilde{c}_{n+1}) - (u_{n-1}\tilde{c}_{n-1})}{2\Delta x} \right\rangle \tag{3.23}$$

or

$$< \frac{\langle u_{n+1}\tilde{c}_{n+1} \rangle - \langle u_{n-1}\tilde{c}_{n-1} \rangle}{2\Delta x} \tag{3.24}$$

As can be seen in equation 3.19 in the case of the real transport terms only the concentrations at the edges of the areas over which the concentrations are averaged are used. In the second case the average over the complete area is used. In the case of areas with a length of 16 pixels, this reduces the random noise with a factor of 4.

The spatial resolution of the first method however is twice as high as the spatial resolution of the second one. We think the higher accuracy of the second method to be more important as the higher resolution of the first method. The higher accuracy of the second method is demonstrated in figure 3.19 where the axial correlations at the first measurement position are shown. The first method is not able to predict the negative side peaks in the correlation whereas the second method is able to do so.

Effect of interpolation of the velocity field

Instead of averaging the LIF field over an interrogation area and compute the correlations afterwards, it is also possible to interpolate the velocity field on the same grid as the LIF data and then do the correlation. It is however computationally expensive to compute the term in the second way. The time needed for the computations will increase with at least two orders of magnitude. First the velocity fields have to be interpolated. After that the correlations have to be computed on the full resolution. The difference is expected to be small for small Δx. Besides, since the gradients are computed on a pixel to pixel base, the noise on the data will increase. Therefore we used averaging of the LIF data and not interpolation of the PIV data.

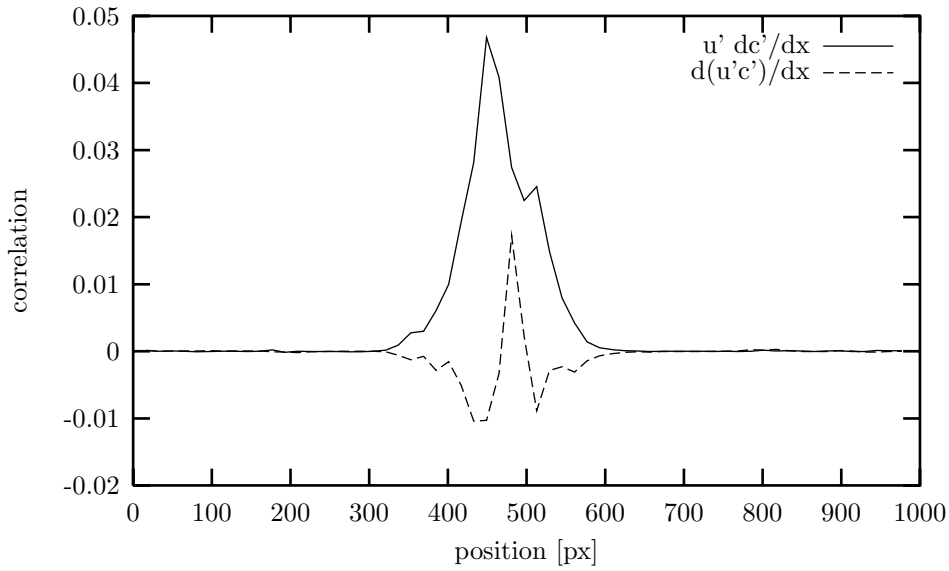

Figure 3.19: Comparison between $\overline{u' \frac{\partial c'}{\partial x}}$ and $\overline{\frac{\partial u' c'}{\partial x}}$

Chapter 4

Experimental setup

4.1 Introduction

The experimental setup used for our experiments was designed and built especially for combined PIV/LIF measurements. We therefore had the possibility to choose the dimensions of the setup in such a way, that all flow parameters fit as good as possible to the technical requirements of the measurement techniques. This is described in the first part of this chapter. In the second part a detailed description of the experimental setup is given. This description is divided in two parts. First we describe the flow facility, whereas second we consider the different measurement systems, which consist of an illumination system and a camera system coupled to a frame grabber. Some special attention is given to the design of the light sheet.

4.2 Experimental parameters

The objective of the measurements is to measure all spatial velocity and concentration scales in a plane through the centerline of a turbulent pipe flow at a Reynolds number of 5300 (based on the pipe diameter and the bulk velocity) with a point source of fluorescein placed at the centerline. A Reynolds number of 5300 is chosen because a data base from a DNS of a point source at the centerline of a turbulent pipe flow (Brethouwer *et al.* 1999) is available for comparison. The results of these experiments is given in chapter 5.
Besides the point source measurements a second experiment was done on a free jet containing fluorescein. The outflow diameter of the jet was 1 mm. The Reynolds number of the jet based on the outflow diameter and velocity, was 2000. The Reynolds number of the jet was equal to the Reynolds number used in a DNS by Boersma *et al* (1998). The setup used for the jet measurements and the results

from the measurements are presented in chapter 6.

PIV parameters

The Reynolds number of 5300 immediately determines the ratio of the largest and the smallest spatial scales in the flow as argued in section 2.3.1. With a camera of 1000×1000 pixels, an interrogation area of 32×32 pixels and a 50% overlap of the interrogation windows, a spatial resolution of 61×61 vectors can be achieved. This resolution is not sufficient to resolve all spatial velocity scales present in the flow since the ratio between the pipe diameter and the average Kolmogorov length scale is about 2.3×10^2. The difference between smallest resolved scale and Kolmogorov scale becomes slightly better if we realize that the mixing initially takes place in the central part of the flow where the Kolmogorov scales are slightly larger than the average Kolmogorov scale computed in section 2.3.1. Since we are studying a point source placed at the centerline of the tube, and the macro mixing is governed by the large scale fluctuations in the flow, this is not a major problem.

We want to simultaneously measure velocity and concentration fields. The two fields can be considered to be measured simultaneous if they are measured within one Kolmogorov time scale.

The dimension of the pipe should be large enough so that an injection mechanism can be implemented without disturbing the turbulent pipe flow too much. The thinnest stainless steel needle with sufficient stiffness has an outer diameter of 1 mm (thinner needles are too fragile). The larger eddies in the flow, which are of the order of 0.1 pipe diameter, should be preferably an order of magnitude larger than the diameter of the injection needle. Given a 1 mm injection needle and the other requirements to be met, a pipe diameter of 50 mm was chosen.

In order to support our choice of a tube of 50 mm, we make a comparison between tubes with a diameter of 50 mm and a diameter of 100 mm. In table 4.1 the values of the main parameters of interest are given for both pipe diameters. Values are shown for a Reynolds number based on pipe diameter and bulk velocity of 5000 and 100.000. One of parameters considered is the eddy turnover time defined by

$$T = 0.1D/u_* \tag{4.1}$$

The wall friction velocity in the tube is estimated with help of Blasius' experimental formula (e.g. (Fox & McDonald 1985))

$$u_* = \frac{U_{mean}}{\sqrt{2}}(0.79\mathrm{Re}^{-1/4})^{1/2} \tag{4.2}$$

The displacement of a flow structure during one eddy turnover time is then given by

$$\Delta_1 = TU_{mean} \tag{4.3}$$

As can be seen from the table, in the case of a 100 mm tube at a Reynolds number of 5000 the displacement of the flow in between 2 successive frames with the cameras

Table 4.1: The most important characteristic scales for Reynolds numbers of 5000 and 100000, and for pipe diameters of 5cm and 10cm.

D (cm)	5		10	
Re	5000	100000	5000	100000
U_{mean} (m/s)	0.1	2.0	0.05	1.0
Q (l/s)	0.2	4	0.4	8
displacement of a particle in between two exposures.				
δ (mm)	3.3	67	1.7	33
δ (D)	0.067	1.3	0.017	0.33
δ (pixels)	68		17	
Eddy turnover time				
u_* (m/s)	0.0069	0.094	0.0034	0.047
T (s)	0.73	0.053	2.9	0.21
Structure displacement				
Δ_1 (m)	0.073	0.11	0.15	0.21
mixing length				
L (m)	0.23	0.33	0.45	0.66

running at full speed, is only 17 pixels. The typical displacement of the particles in one frame for PIV measurements should be 8 pixels, so in that case we can almost do a cross correlation between successive images. Since the eddy turn-over time is 2.9 s, we need 87 frames to measure one eddy turn-over time. Since the amount memory available is limited, and we want to obtain converged statistics we think that this is a bit oversampeled. So a pipe diameter of 100 mm is too large. In the case of a pipe diameter of 50 mm, the displacement of the particles in between 2 exposures is 68 pixels and it takes 22 frames to measure one eddy turn-over time. A particle moving through the field of view is captured about 14 times. For these reasons a pipe diameter of 50 mm was chosen.

LIF parameters

Until now only the consequences of the choice for a certain pipe diameter for the PIV measurements were considered. Let us now have a look on the experimental parameters for the LIF measurements.

The most simple model for the mixing process is the mixing length model which supposes that the mixing is proportional to a factor K equal to

$$K = u_* l \tag{4.4}$$

with l the typical size of an eddy, being $0.1D$. The spreading σ of the source as

function of the downstream position X is then given by

$$\sigma^2 = 2K\frac{X}{U_{mean}}, \tag{4.5}$$

where U_{mean} is the mean velocity at the location of the source. The scalar in the pipe is supposed to be fully mixed if the spreading σ becomes equal to $1/4\ D$. The distance from the source at which $\sigma = 1/4D$ is therefore called the mixing length. This implies that the mixing length L is given by

$$L = \frac{DU_{mean}}{3.2u_*} \tag{4.6}$$

As mentioned in section 2.2.1 the smallest temporal scale for the scalar mixing is the Batchelor time scales. The Batchelor time scale for a 50 mm tube with fluorescein as a scalar at a Reynolds number of 5000, is 25 ms.

For making pictures of the flow, however, not the Batchelor time scale, but the convective time scale of a concentration structure is the most important scale. This time scale is defined as the time needed to transport a concentration structure over a distance of one Batchelor length scale by the local mean flow speed. This is in the case of a flow with a Reynolds number of 5000 and a pipe diameter of 50 mm:

$$\frac{\lambda_D}{U} = 0.032 \text{ ms} \tag{4.7}$$

So in the ideal case, if all the concentration length scales need to be resolved, the exposure time of the LIF measurements should be less than 0.032 ms. Since the cameras used are not able to resolve all concentration scales, not the convection time of the Batchelor length scale, but the convection time of the image of the concentration structures over one pixel of the camera would preferably be the maximum exposure time. In recording the pictures over a complete pipe diameter, the convection time of 1 pixel at a Reynolds number of 5300 is approximately 0.5 ms. If possible the LIF exposure time should therefore not exceed this 0.5 ms to avoid any blurring of the images due to moving of the structures during the exposures. This maximum exposure time for the LIF measurements decreases with increasing maximum flow velocity.

4.3 Flow facility

A schematic drawing of the setup is given in figure 4.1. The flow facility consists of a 6 meter long perspex pipe with an inner diameter of 50 mm. The pipe is mounted on a steel framework supporting the pipe every meter. The framework is placed on rubber feet to make it less sensitive to vibrations. The pipe can be aligned in both horizontal and vertical directions. The alignment is done with the aid of a

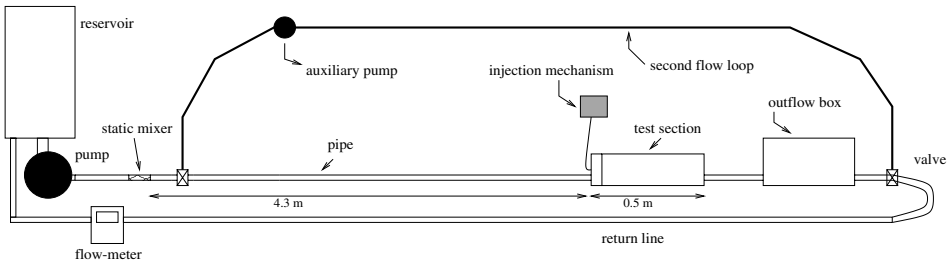

Figure 4.1: A schematic overview of the flow facility.

laser beam. At the entrance of the tube a static mixer is placed to make sure that a symmetric and swirl-free velocity profile is obtained. At a distance of 4.3 meters downstream of the static mixer the injection device for fluorescein is placed. With a length of 86 pipe diameters between the static mixer and the injection device, the turbulent flow at the location of the injection can be expected to be fully developed (Schlichting 1979).

This is checked by both LDV and PIV measurements of the velocity profile without the injection mechanism. The results are compared with previously done measurements with PIV (Westerweel *et al.* 1996) and LDV (Tahitu 1994) measurements, and with the results of a DNS (Eggels *et al.* 1993). The results are shown in chapter 5 figure 5.1. The injection device will be further described in section 4.3.2.

4.3.1 General setup

The injection device is placed at the entrance of the measurement section This measurement section is needed for distortion free access for the optical measurement techniques such as PIV and LIF. At the end of the pipe an outflow chamber is placed. The pipe can slide into the outflow box which makes it possible to mount for example an injection mechanism. One can simply disconnect a pipe section, slide the pipe partially into the outflow box, mount the injection mechanism and then reassemble the pipe.

With an electromagnetic flow meter the volume flux is measured. The flow meter is mounted at the end of the return pipe. The return pipe leads to two reservoirs. Each reservoir can contain up to 150 liter of water. The system volume without the reservoirs is approximately 61 liter. The total system volume is therefore about 350 liters. The reservoirs are mounted such that it is possible to pump the contents of one reservoir via the pipe into the other reservoir. This is useful in the case of a flow with chemical reactions. In our case no chemicals were added to the flow and therefore the fluid was just circulated.

To be able to calibrate the LIF measurements the measurement section has to be filled with a fluorescein solution with a known uniform concentration. In order to

Table 4.2: A summary of the most important data of the experimental setup.

system volume	350 l
volume calibration loop	25 l
pipe length	6 m
pipe diameter	50 mm
entrance length	4.3 m
length measurement section	25 cm
wall thickness glass cylinder	1.8 mm
inner diameter glass cylinder	50.8 mm
pump type	dp-pumps dpv2-10
pump capacity	0.6 l/s ($\mathrm{Re} = 15 \times 10^3$)
frequency modulator	ABB ACS600

be able to reduce the amount of fluorescein needed to do so, a second flow loop with a reduced volume was induced in the facility. When using this second flow loop not the complete system volume of 350 liters has to be filled with the uniform fluorescein solution. As indicated in figure 4.1, turning the valves at the beginning and the end of the main pipe, the reservoirs and the return pipe are separated from the main pipe, and a circulation is possible through a small tube. An auxiliary pump forces a constant flow through the pipe and outflow chamber. This second loop has only a volume of approximately 25 liters. By injecting 60 ml of a fluorescein solution with a concentration of 20 mg/l in the outflow chamber the calibration loop is filled with a uniform fluorescein concentration which is high enough to measure the light intensity distribution for the calibration process, discussed in 3.3.2.

The pump used for driving the main flow is a centrifugal pump manufactured by Duivelaar Pompen (dp-pumps dpv2-10). The pump speed is controlled by a frequency converter (ACS 600 Frequency Converter, by ABB). The pump is mounted with a plastic hose to the entrance of the pipe so that transport of vibrations caused by the pump is reduced.

The auxiliary pump used for driving the calibration loop is a small centrifugal Iwaki Magnet Pump. The maximum flow rate of the pump is 16 liter per minute at zero pressure difference, which is enough to force the flow through the pipe to be turbulent, and this is necessary to maintain a sufficient mixing of the injected fluorescein in the pipe volume.

All relevant data for the total setup are summarized in table 4.2

4.3.2 Injection device

The injection of fluorescein in the turbulent pipe flow should be done with a minimal disturbance of the flow. Therefore, the fluorescein is injected through a thin L-

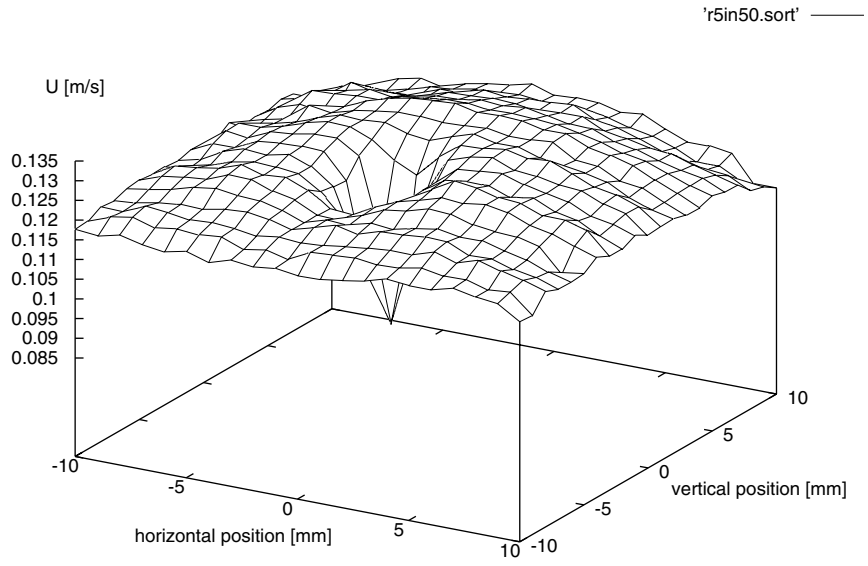

Figure 4.2: The two dimensional axial velocity profile just behind the injection needle

shaped needle with an outer diameter of 1.0 mm. The inner diameter was about 0.5 mm. Since the fluorescein is injected in the wake of the needle, a isokinetic injection of the fluorescein is impossible. This is clearly shown in figure 4.2 where the two dimensional axial velocity profile in the center part of the pipe is given at a position just behind the needle. This profile is measured in the plane perpendicular to the flow direction, with the injection mechanism present but without the injection of fluorescein. The injection of the fluorescein should be laminar to prevent mixing by the injection in stead of by the turbulence in the pipe.

The needle is mounted between the last pipe section before the measurement section and the measurement section as sketched in figure 4.3. The length between the beginning of the measurement section and the first measurement position is 12.5 cm. The injection needle has a length of 10 cm in the horizontal direction. This 10 cm is needed to bridge the distance between the junction between the pipe and the measurement section, where the injection needle enters the set-up, and the first measurement position. The horizontal part of the needle is also needed to reduce the influence of the wake of the vertical part of the injection needle. Visual inspection showed that no movement of the needle could be seen during the experiments, e.g.

due to the turbulence in the pipe. A sketch of the injection needle and it's mounting is given in figure 4.3.

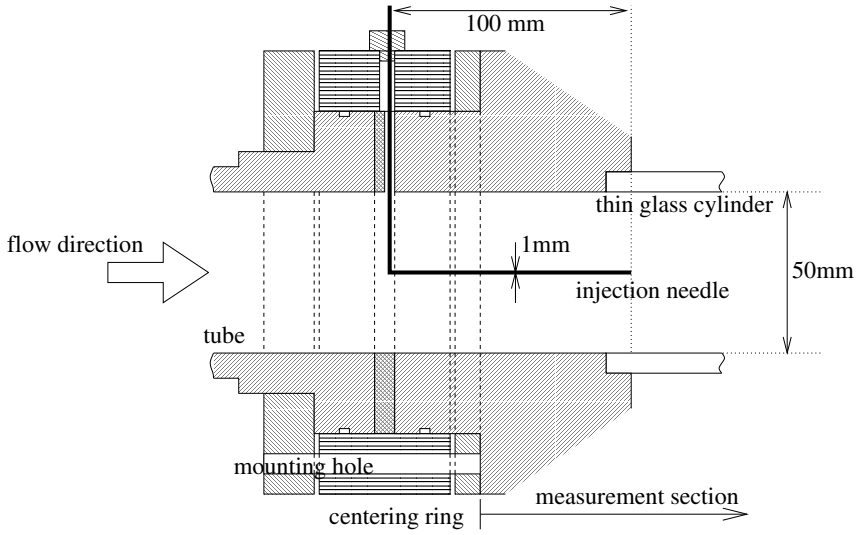

Figure 4.3: A sketch of the mounting of the injection needle.

It is important to know the exact fluorescein flux. The injection of the fluorescein through the needle, with a known concentration, is carried out by a stepper motor that drives a traversing table on which a syringe is mounted. The speed of the motor is controlled by a constant voltage supplied to a voltage-to-frequency converter that drives the stepper motor. This procedure is followed to obtain an injection velocity, and therefore a fluorescein flux, which does not depend on the friction of the syringe or the static pressure in the pipe. The inner diameter of the syringe is 21.6 mm. A calibration curve of the speed of the syringe as function of the input voltage is given in figure 4.4. As can be seen the speed of the syringe is a linear function of the input voltage, although a small offset is found. Based on this curve and the inner diameter of the syringe the volume flux of fluorescein can be computed.

4.3.3 Measurement section

To avoid the optical distortion of the round tube, we need a rectangular measurement section filled with water that encloses the round pipe. Within this box the pipe is replaced by a thin glass cylinder with an inner diameter of 50.8 mm and a thickness of 1.8 mm.

With the measurement section used, a small amount of deformation is still left due the difference in index of refraction between water and the inner cylindrical

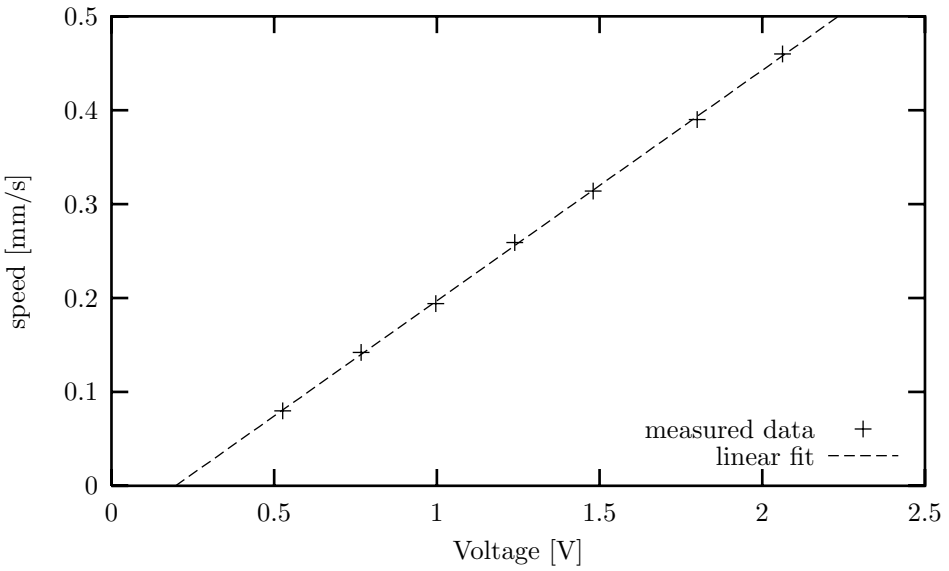

Figure 4.4: The calibration curve of the speed of the syringe as function of the input voltage.

tube. Calculations however show that the deformation in the region the where the measurements are done, is well within the measurement inaccuracy. These calculations are based on ray tracing in the measurement section using Snellius law for each surface, where the lens in front of the camera is supposed to cause no deformation. In figure 4.5 the computed difference between the real position in the tube and the actual position are shown as function of the distance from the cylinder wall. As can be seen distortion becomes smaller than 0.05 mm for distances more than 1.5 mm from the wall. The field of view from the camera during the measurements stopped at a distance of 2.5 mm from the wall, so all image distortions due to the difference in index of refraction are less than 0.05 mm. This is about the size of one pixel and can therefore be neglected.

The inner diameter of the glass cylinder is slightly larger than the diameter of the pipe. The difference in cross section is 3%. The junction between the pipe and the glass tube is smooth and has a small angle so we expect that no vortex shedding will take place. The difference in diameter between the glass cylinder and the tube is so small that there is no measurable influence on the velocity profile as can be seen in figure 4.6. The velocity profile shown is measured using an LDV system. The measured velocities are computed with and without the correction for the deformation by the glass cylinder. With the correction applied to to the position, at 0.4 mm from the wall the measurements are still on the theoretical

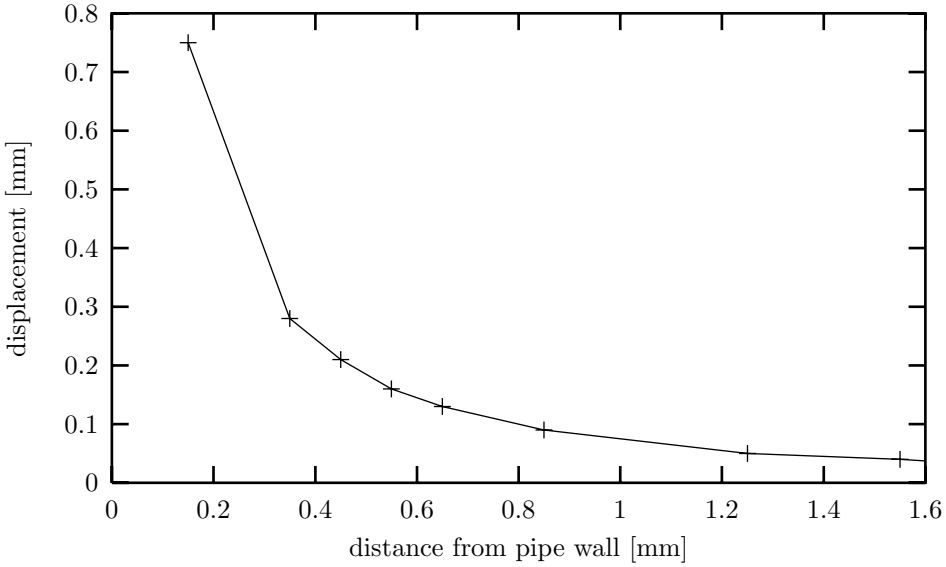

Figure 4.5: The difference between the real and the observed position in the tube due to refraction in the glass cylinder.

curve.

The outside of the measurement section is made of four glass plates, mounted in an stainless steel frame. An expanded view of the measurement section is given in figure 4.8. The glass plates are mounted with steel clamps as shown in this figure.

The size of the glass plates is 315×90×9 mm. The thickness of the glass plates was determined by the fact that the plates have to be optically flat. Glass windows are used to be able to withstand the pulsed YAG-lasers. (Tests with the YAG beam entering a perspex box showed deformation of the surface and bubbles appearing inside of the perspex.)

With the measurement section we have solve the optical deformation problem, but also some new problems appear. If a laser light sheet enters the measurement section, a small fraction of the light will be scattered at each surface that the beam crosses, e.g. the air-glass surface at the bottom of the measurement section, and the glass water surface at the other side of the glass wall. When the light sheet reaches the top of the measurement section, also a water-glass and a glass-air surface are crossed as is sketched in figure 4.7. The scattered light will reflect on the surface of the tube and appear in the measurement frames as bright lines. At the position of these lines no PIV measurements can be done because of over-exposure. To partially solve this problem, two plates are mounted in the inside of the measurement section at the side where the laser beam enters and at the top where the beam exits the

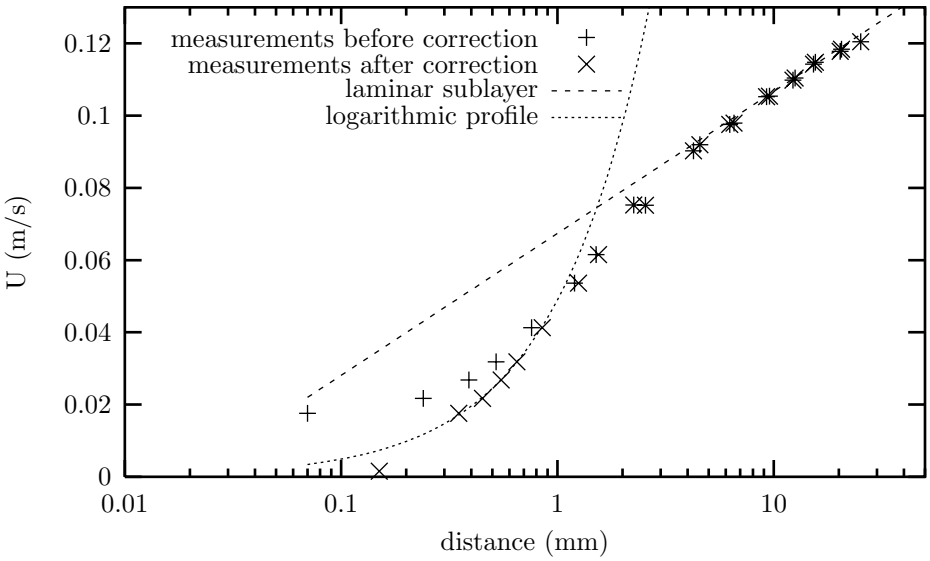

Figure 4.6: The velocity profile before and after correction for image distortion due to the glass tube.

measurement section. In the middle of the plates we made a slit of 1 mm wide, which is about twice the thickness of the light sheet. The laser light sheet passes through this slit. The reflected light will be blocked by the plates as shown in figure 4.7. The geometry of the plates is shown in the expanded view of the measurement section given in figure 4.8.

However, with these slits not all reflection problems were solved: some light will be scattered by the blunt edges of the slits, and also the wall of the thin glass cylinder will scatter light when the light sheet passes through the test section. Some of these reflections will still produce lines in the measurement frames. The effect of these problems can be reduced by using larger tracing particles for the PIV. Larger particles scatter more light, so that the lens aperture of the camera for the PIV measurements can be chosen smaller, which reduces the brightness of the reflection lines in the measurement frames. The intensity of these reflections is proportional to the power of the laser. The intensity of the light scattered by a particle is proportional to the power of the laser multiplied by the cross section of the particle. So if the particle diameter is doubled the intensity of the light scattered by the particles increases with a factor of 4. The aperture of the lens can therefore be reduced, causing the relative effect of the reflection lines to decrease. At the other hand, by doubling the particle diameter, the volume fraction of the particles increases with a factor of 8. If the particles used for the PIV are too

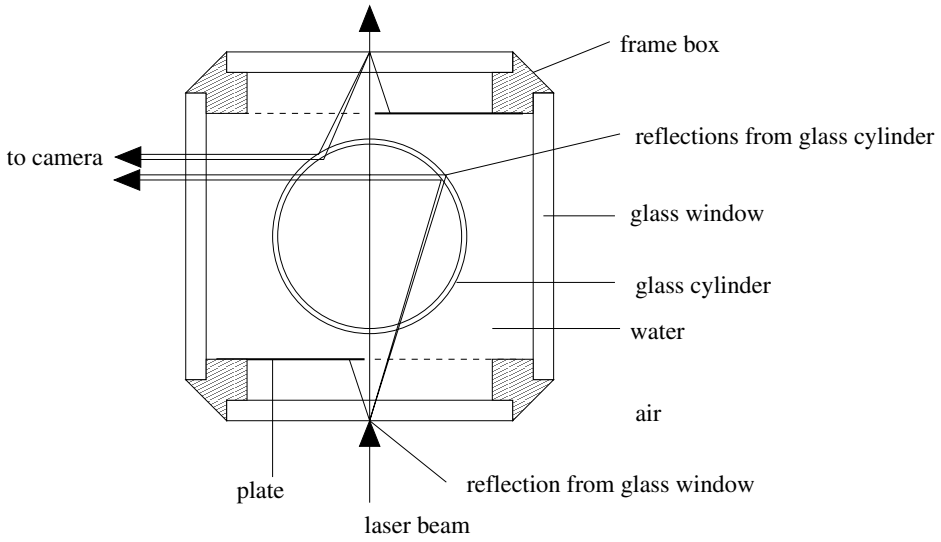

Figure 4.7: A sketch of the effects of the slits on the reflection problem.

big or the volume fraction of the particles is too high, a problem will occur with the LIF measurements. The particles should be at least an order of magnitude smaller than the thickness of the light sheet. If the particles are too big, they will cause a shadow in the LIF light sheet, in which no concentrations can be measured. Besides this shadow effect, the particle density should be so small that the decay of the light intensity of the light sheet caused by the scattering by the particles is negligible. Also the amount of scattering by the particles of the light emitted by the fluorescein should be kept small. In our case where the particle diameter is 5μm, they are small enough compared with the thickness of the light sheet which is 5 mm. The volume fraction of the particles is also very low ($\mathcal{O}(10^{-6})$), and therefore the problems mentioned above do not arise. An example of a recorded PIV image is given in figure 4.9. As can be seen some reflection lines are still present in the frames.

4.4 Laser light sheet

4.4.1 Gaussian beam optics

In this section we consider the design of the laser sheet. The laser beam is governed by the equations for Gaussian beam optics which are different from the standard equations for geometrical optics. Here we give only a short description of the consequences of the Gaussian beam optics and for a more detailed discussion we refer

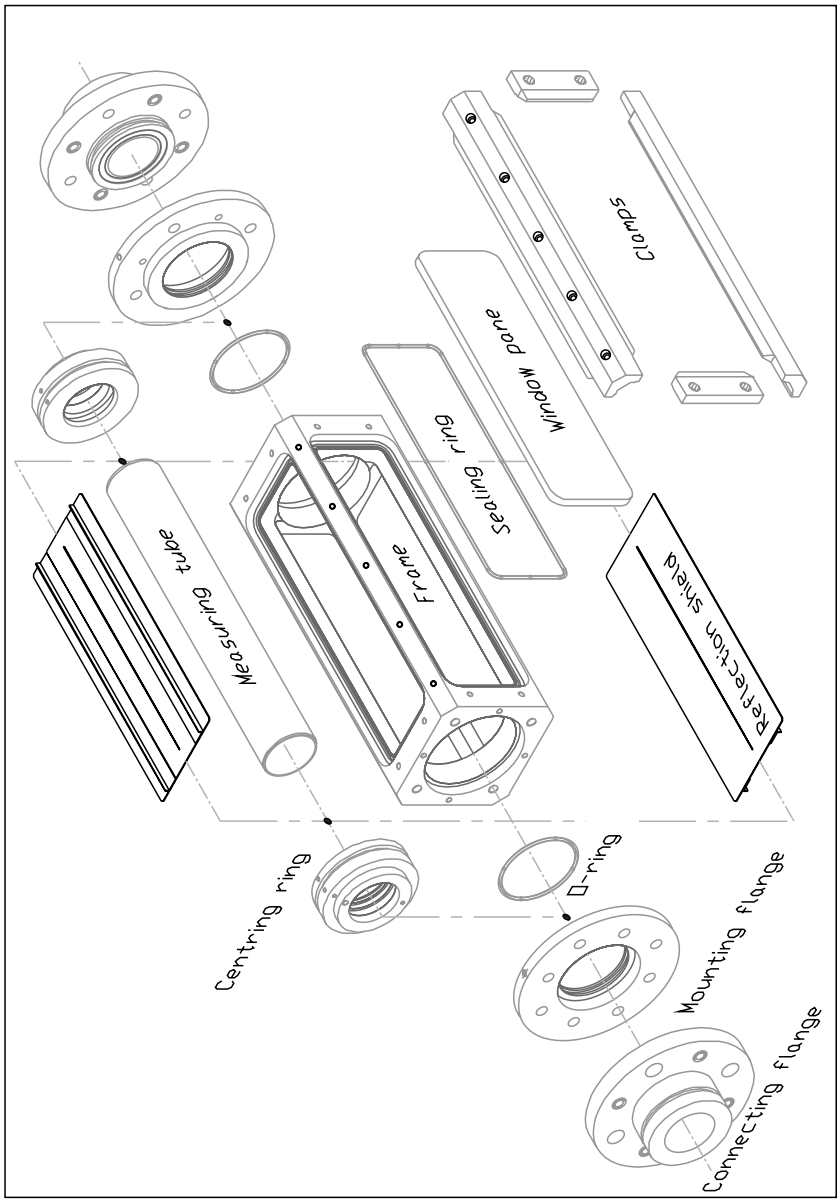

Figure 4.8: An expanded view of the measurement section.

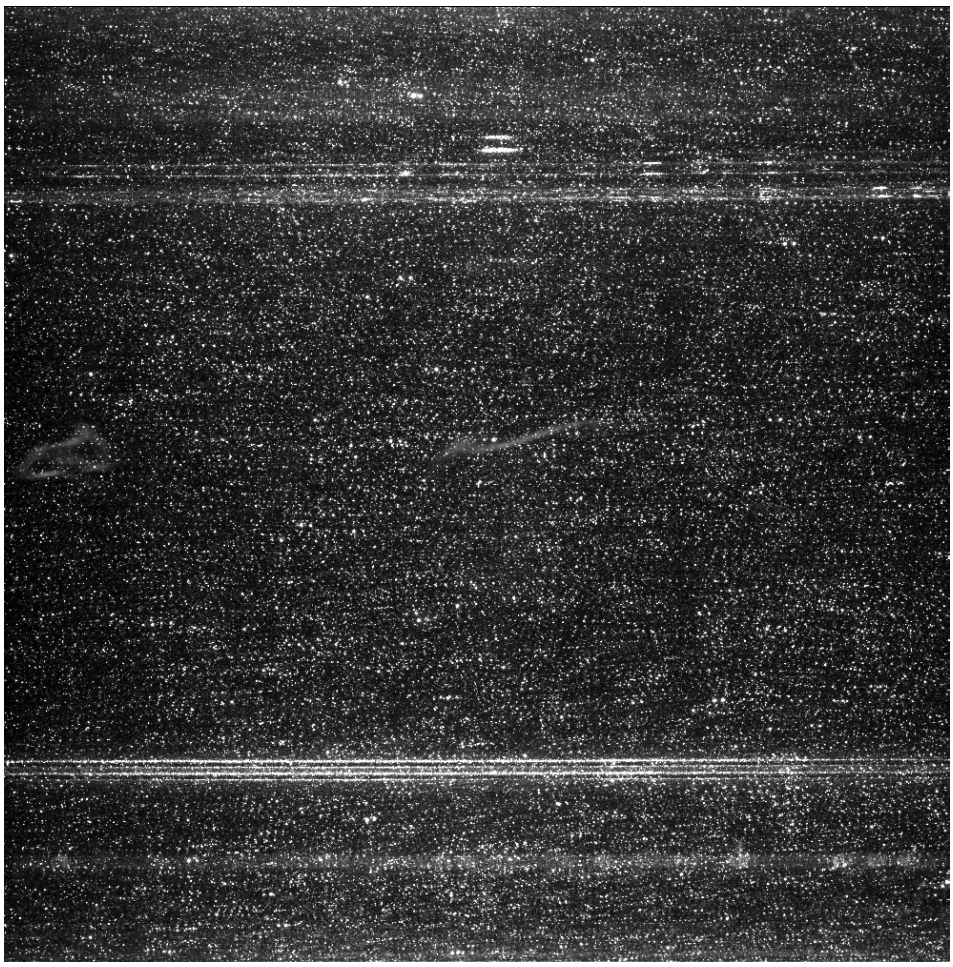

Figure 4.9: An example of a recorded PIV image. Size of the image: 992x1004 pixels, length: 45 mm. The reflection lines appear as horizontal bright lines

to Durst & Stevenson (1977).

When a laser beam passes a positive lens, the beam does not converge to a point, but to a minimum radius. This minimum radius is called the waist of the laser beam, and depends on the angle of convergence of the beam far away from the waist. The length over which the diameter of the beam changes with a factor $\sqrt{2}$ is called the Rayleigh length. The waist radius and the Rayleigh length are related to each other by the following relation:

$$Ra = \frac{\pi w_0^2}{\lambda} \tag{4.8}$$

in which w is the radius of the waist, λ is the wavelength of the light and Ra is the so called Rayleigh length of the waist.

The lens equation for a Gaussian beam is given by:

$$\frac{1}{z_2\left(1+\frac{\pi^2 {w_2}^4}{\lambda^2 {z_2}^2}\right)} + \frac{1}{z_1\left(1+\frac{\pi^2 {w_1}^4}{\lambda^2 {z_1}^2}\right)} - \frac{1}{f} = 0, \tag{4.9}$$

in which z_1 is the distance of the object waist to the lens, z_2 is the distance of the image of the waist to the lens, λ is the wavelength of the light, w_1 is the radius of the waist before and w_2 is the radius of the waist after the lens. A sketch of the situation is given in figure 4.10

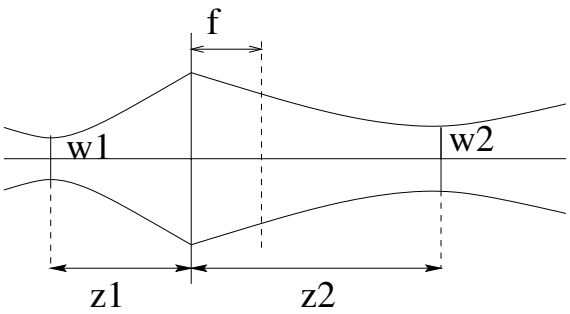

Figure 4.10: A schematic overview of the image of a waist by a lens.

The relation between the radius of the waist before and after the lens is given by:

$${w_2}^2\left(1+\frac{\lambda^2 {z_2}^2}{\pi^2\,{w_2}^4}\right) - {w_1}^2\left(1+\frac{\lambda^2 {z_1}^2}{\pi^2 {w_1}^4}\right) = 0. \tag{4.10}$$

4.4.2 Design of the laser light sheet

To be able to do accurate PIV and LIF measurements, a thin and non-diverging light sheet is needed. A thin light sheet is needed in order to resolve the smallest

velocity scales and as much of the concentration scales as possible. A parallel light sheet is required to prevent large differences in light intensity as function of the position in the light sheet. These two requirements however are in contradiction to each other, since a light sheet with is non-diverging over a large distance implies a thick light sheet. So a compromise should be found.

To obtain a thin light sheet, the waist of the laser sheet should be positioned at the measurement position. The width of the sheet should be slightly larger than the field of view of the camera, which in our case is the pipe diameter, 50mm at maximum. The incoming laser beam has a diameter of at least 6 mm. The shape of the YAG beams is not circular and therefore no exact beam diameter can be given. To be independent of the orientation of the beam the minimum beam width was used in the computations, since in that case we are sure that the resulting light sheet is not too small.

A light sheet can be considered as parallel if the Rayleigh length is of the order of the size of the field of view of the camera, therefore a Rayleigh length of 50 mm was chosen. In that case the length over which the light sheet grows to $\sqrt{2}$ the thickness of the waist lies at 50 mm on both sides of the waist. A Rayleigh length of 25 mm would cause an increase of the thickness of the sheet with a factor of $\sqrt{2}$ moving from the position of the waist at the centre to the walls. Such an increase in thickness would imply a significant decrease in intensity, which is not acceptable. In the case of Ra=50 mm the increase in thickness of the light sheet over the pipe diameter is only a factor 1.12. The waist of the light sheet is in this case 0.2 mm.

An other condition to be satisfied for the optical setup is, that it is not allowed to have a focal point (a waist with a short Rayleigh length) or focal line present in the beam path. Due to the high power of the YAG lasers the presence of a focal point would immediately cause dissociation of air molecules. Even a focal point of a reflection of 4% of the full power of the YAG lasers (200 mJ/pulse, pulse duration 6 ns) is enough to cause such ionisation.

Finally it is required that the total length of the optical setup does not exceed about 0.7 m in order to mount the optical setup on the optical plate that we have available. The optical plate has a width of 0.5 m and a length of 1 m. On this plate also the 2 cameras for doing PIV and LIF measurements have to be mounted. On the other hand the position of the waist has to be far enough behind the last lens so that it can be positioned at the centerline of the tube inside the measurement section. Approximately 25 cm is needed for this distance.

To create a parallel light sheet with a prescribed width, Rayleigh length and at a prescribed position of the waist, at least two lenses are needed. Here we have chosen for a setup with three lenses as sketched in figure 4.11. The extra lens gives the opportunity to modify the thickness of the light sheet by moving the lens without changing the other lenses. The last lens is chosen to be spherical. A cylindrical lens would have been more straightforward but also much more expensive. Now the effect of the last lens on the position and width of the waist has to be taken into

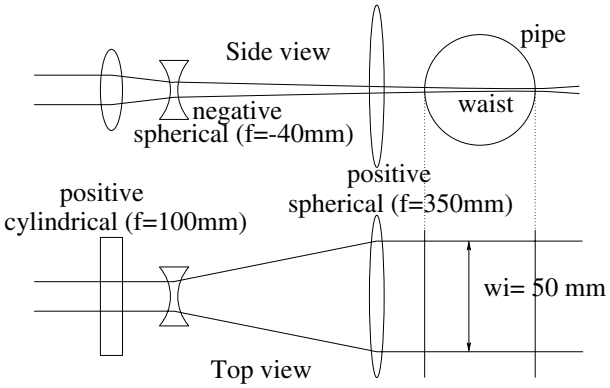

Figure 4.11: A schematic overview of lenses used to create the light sheet.

account too. In the case of a cylindrical lens, the lens would only effect the width of the light sheet. The width of the light sheet is determined by the ratio of the focal lengths of the last positive spherical lens and the negative spherical lens. The ratio of the diameter of the incoming beam and the width of the light sheet is 8.3, so the minimal ratio between the lengths of the focal depths of the lenses used should be 8.3 too. The lenses have to be placed in so called f-f position. This means that the focal points of the lenses are at the same position. The length of the optical setup is determined mainly by the focal length of the last lens.

The final computation of the positioning of the lenses was done with Maple. After some trial and error and optimization, a combination of a 100 mm positive cylindrical lens and a 40 mm negative spherical lens appeared to be a good combination for creating the prescribed waist. Because the ratio of the focal lengths of the negative and the last positive lens should be at least 8.3, the focal length of the last lens should be at least 350 mm. In that case the position of the waist is positioned 24 cm behind the last lens. If a lens with a larger focal depth is used the position of the waist moves towards the lens. A larger focal depth will give problems in positioning the waist in the center of the pipe. A smaller focal depth results in a too small width of the laser light sheet. Therefore a 350 mm lens seems the optimal choice. The computed distance between the cylindrical and the negative lens is 38.7 mm. The distance between the negative and the positive lens has to be 310 mm. The cylindrical lens is mounted on a small traversing table with a micrometer adjustment.

4.5 Measurement system

Next we consider the measurement system, which consists of three lasers, two cameras and a data acquisition system. First the lasers re described. Then the camera and the data acquisition system are presented. In the last part of this section the details of the PIV and the LIF systems are given and the timing diagram for the whole setup is described.

4.5.1 Lasers

The illumination system for the PIV and LIF measurements consist of three light sources and a set of sheet forming optics. The light sources are the 488 nm line of an Argon-ion laser for the LIF measurements and two Q-switched frequency-doubled Nd:YAG lasers for the PIV measurements.

The Argon-ion laser is a Spectra-Physics series 2000 laser with a total output of 5 W continuous. This laser emits light at multiple wavelengths (see figure 4.12). The maximum power of the 488 line of the Argon-ion laser is 2.4 Watt. The Argon-ion beam has a waist of approximately 1 mm.

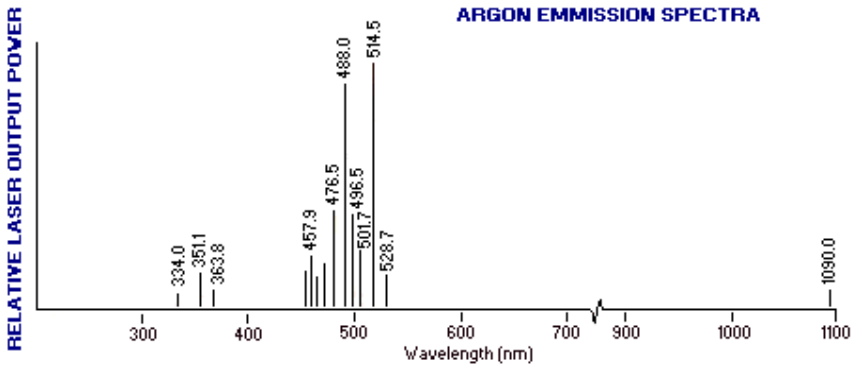

Figure 4.12: The light emission spectrum of an Argon-ion laser.

The Nd:YAG lasers are Quanta-Ray lasers manufactured by Spectra-Physics. The Nd:YAG lasers have a frequency of 1064 nm. A harmonic generator is used to obtain pulses with a wavelength of 523 nm. The Nd:YAG lasers have a pulse frequency of 30 Hz, a pulse length of 6 ns and a pulse energy of 200 mJ at a wavelength of 532 nm. The diameter of the YAG-beams is approximately 7 mm. Although lasers are used with an optical setup to make the beams more Gaussian, the cross sections of the beams are found to be not perfectly circular. An observation of the shape of the beams is given in figure 4.13. This picture is made by catching a laser shot on a piece of non-illuminated developed Polaroid film.

Table 4.3: A summary of the most important data of the lasers used.

Nd-YAG laser	pulsed
manufacturer	Quanta-Ray
pulse frequency	30 Hz
pulse energy	200 mJ
pulse duration	6 ns
waist	≈7 mm
Ar^+ laser	continuous
manufacturer	Spectra-Physics
type	series 2000
power	2.4W in 488nm line
waist	≈1 mm

The polarization directions of the light of the two YAG beams are orthogonal with respect to each other. An overview of the specifications of the two lasers is

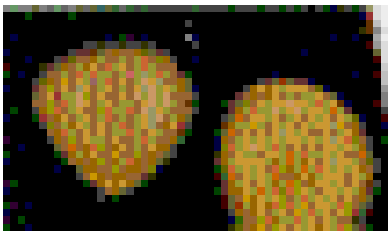

Figure 4.13: The shape of the YAG beams.

given in table 4.3.

To be able to combine the laser beams first we have to expand the Argon-ion beam to the same diameter as the YAG beams. This is simply done with two lenses with focal lengths of -20 and 80 mm respectively, which are placed such that the focal points of the lenses coincide. Just behind this beam expander an electro-optical shutter is placed. This shutter is needed to prevent the presence of fluorescence light to disturb the PIV measurements and to prevent saturation of the fluorescein during the LIF measurements. The shutter consists of two parts. The first part turns the polarization direction of the beam over an angle of 45 degrees if the shutter is switched on. The second part is a polarization prism. This prism blocks the beam if it is rotated over 45 degrees. If the beam is not rotated, it reduces the intensity of the beam with a factor of 2.

Behind the shutter the Ar^+ and the Nd:YAG beams are combined. This is done with a specially designed filter which reflects the 488 nm light from the Argon-ion laser and which is transparent for both polarization directions of the YAG laser.

The difficulty in combining the two YAG beams with the Argon-ion beam is that the wavelengths of the lasers are quite close to each other combined with the fact that both polarization directions of the YAG lasers have to be transmitted. Besides that the power of the YAG-lasers is so high that no beam-splitter cube can be used. The glue in between the two halfs of the cubes can not resist the power of the beams. To be able to combine the beams a filter was designed which has to be used at an angle of attack which deviates from the usual 45 degrees with about a factor of two. With the normal angle of attack no coating could be made with the required properties. Besides that the cut-off frequency of the filter is adjustable by varying the angle of attack of the beams. In our case the angle of attack had to be 22 degrees as shown in figure 4.14. The filter was designed and manufactured by OptoSigma. A sketch of the complete optical setup is shown in figure 4.15.

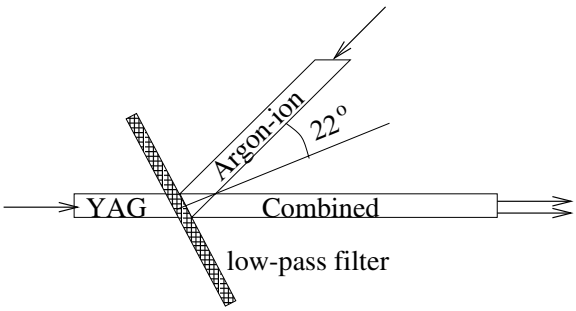

Figure 4.14: A sketch of the filter for the combination of the two beams.

The optics are placed in such a way that the sheet forming optics and the cameras can be traversed along the setup without moving the optics used to combine the different laser beams. In this way measurements can be done at different positions along the pipe without realigning the optics. The cylindrical lens is mounted on a small traversing table. By traversing this lens the position and thickness of the light sheet can be modified.

As mentioned before the polarization directions of the two YAG beams are perpendicular to each other. The amount of light scattered by a small particle depends on both the angle between the beam and the observer and on the polarization direction of the beam. The the camera direction is perpendicular to the light sheet. The polarization direction of each YAG beam has an angle of 45 degrees with the light sheet as sketched in figure 4.16. In this way the amount of light scattered by a particle is equal for both beams and thus equally bright particle images are seen by both cameras.

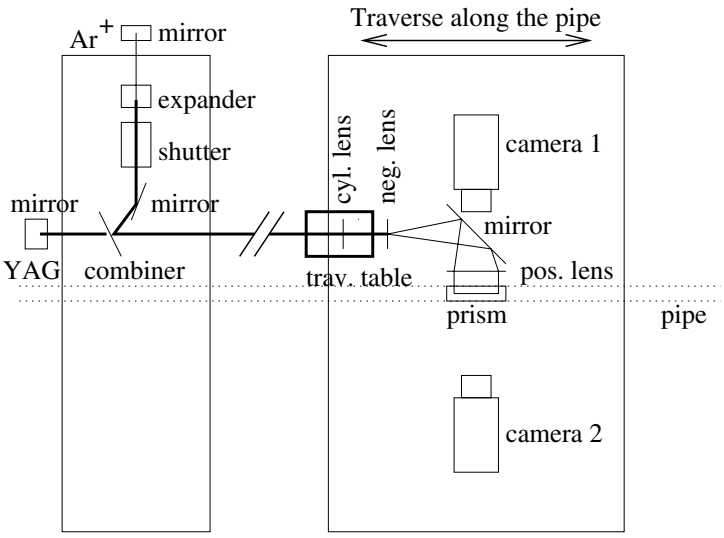

Figure 4.15: A schematic overview (top view) of the optics used to create a light sheet (not to scale). The right hand table can be traversed along the pipe.

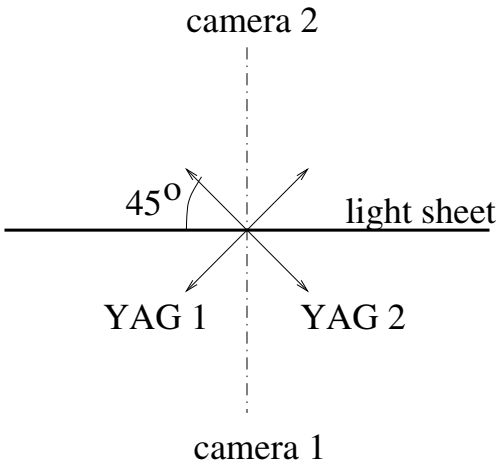

Figure 4.16: The polarization of the two YAG beams with respect to the light sheet.

4.5.2 Alignment of the laser sheets

A good alignment of the two YAG and the Ar^+ laser sheets is very important for the reliability and quality of the measured data. If the two YAG laser sheets are not properly aligned, no doubly exposed particles will be seen, and therefore no displacement can be measured. If the LIF sheet is not aligned correctly with the PIV sheets, no reliable correlations between concentration gradients and velocity fluctuations can be measured.

A first, rough, alignment of the two PIV light sheets is done visually, this means that first the beams are adjusted until they appear to be aligned visually by observing their images on the entrance window of the test section. The next step is to make PIV images of a slow laminar flow and optimize the amount of doubly exposed particles observed on the monitor screen. The problem with the YAG laser sheets is that the YAG beams do not have a nice circular cross section. This causes the sheets to be asymmetric, and this is one of the reasons for bad vectors in the PIV measurements.

4.5.3 Cameras and image acquisition system

The PIV and LIF images are recorded with two 992×1004 pixel CCD cameras (Kodak ES-1.0), connected to a pipeline processor. The pixels are square and have a center-to-center spacing of 9 μm. The maximum frame rate of the cameras is 30 Hz.

A CCD camera consists of a two dimensional array of light sensitive elements, or 'pixels'. These elements build up a charge which is proportional to the light intensity (i.e. number of photons) falling on the CCD element. After a certain time interval the charge of the elements is read out and stored. In this way a light intensity distribution as it falls on the CCD chip can be measured. The collected charge is discretized by an 8 bit analog-to-digital converter, so a resolution of 256 gray values is obtained. The charge on the elements grows linearly with the amount of light and therefore the grey values can be interpreted as a linear function of the light intensity. Tests showed that the noise level in case of no illumination of the CCD is about 1 grey value. The pixels have a fill ratio of 20%. Using micro lenses the effective fill ratio of the pixels is increased to about 60%. The effect of the fill ratio on the measurements has been discussed in section 3.2.4.

The Kodak cameras use a so called interline transfer. This means that before the recorded image is transfered to the computer, which takes about 32 ms, it is stored in an extra buffer present on the CCD chip. The latter step takes only a few nano seconds. It is therefore possible to start the exposure of the next frame only a few micro seconds after the exposure of the first one.

The Kodak cameras that we use can be operated in three modes, the triggered mode, the free run mode and the dual frame mode. In the 'triggered mode' the

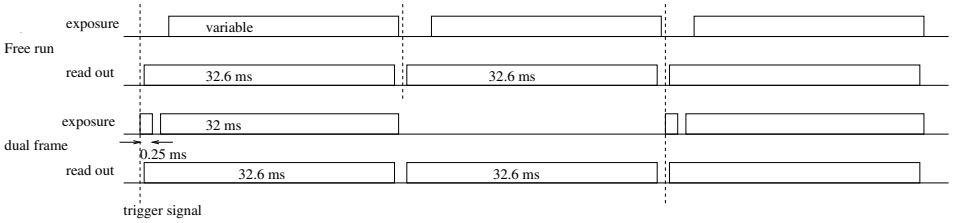

Figure 4.17: A schematic picture of the exposure and readout timing in the free run and dual frame mode of the Kodak cameras.

shutter of the cameras is opened after an external trigger pulse. The maximum frequency of the cameras is coupled with the required exposure time. This maximum frequency is given by

$$f_{max} = \frac{1}{32.6 \text{ ms} + \text{exposure time}}. \tag{4.11}$$

In the 'free run' mode no trigger is needed. In that case the cameras run at a frequency of 29 Hz. Although no trigger is needed, it is still possible to provide the cameras with a trigger signal with a frequency in between 29.5 and 30.5 Hz. In this mode we have both cameras running at nominally 30 Hz without restrictions for the exposure time. In this triggered 'free run' not the beginning of the exposure of the cameras, but the start of the data transfer to the computer is triggered. The result is that the exposure of the cameras ends just before the trigger signal.

In the "triggered double exposure" mode, or "dual frame" mode, two frames are recorded with a separation time of only a few micro seconds. The first frame has a fixed exposure time of 0.25 ms, the second exposure time has a fixed exposure time of about 32 ms. During the second exposure, the first frame is transferred to the computer. During the point source measurements the camera was in triggered mode, for the jet measurements we used the dual frame mode. A schematic picture of the exposure and readout timing in the free run and dual frame mode is shown in figure 4.17.

The image acquisition system consists of two pipeline processors, one for each camera, that are used to read out the CCD chips of the cameras and store the images. The image acquisition system stores the images in a 256 Mb video memory consisting of eight 32 Mb memory boards (DATACUBE MEGASTORE-32). The system host computer is a SUN SPARC workstation.

To be able to display the full pipe diameter on the CCD chip a micro Nikkor 55 mm lens was used. With this lens images can be recorded with a magnification up to 0.5 without using extension rings. This lens was used within its designed specifications, so we expect optimal image quality. If a normal Nikkor 55 mm lens would have been used, extension rings would have been needed to obtain the

Table 4.4: Data sheet for the cameras used.

lens:	micro Nikkor
focal length:	55 mm
camera:	Kodak ES2
resolution:	992×1004 active pixels 256 grey values
pixel size	$9 \times 9\mu$m
frequency:	
free run:	30 ± 0.5 Hz
triggered:	minimum: 0
	maximum: $\frac{1}{32.6 \text{ ms} + \text{exposure time}}$

desired magnification. This would possibly have decreased the image quality. With the lens and a CCD sensor with a dimension of 9 mm, an object size of 18 mm can be reached. The measurements were done with a magnification of 0.20 (see section 4.5.6). With this magnification and a CCD chip of 9×9 mm^2, an object field of 46×46 mm is viewed. The exact value of the magnification was determined by making an image of a pattern of horizontal and vertical lines with a line spacing of 1 mm.

To be able to make sharp images of the light sheet the focal depth of the camera system should be at least equal to the thickness of the light sheet. The focal depth in the object plane is given by (Adrian 1991)

$$\delta z \approx 4 \left(1 + \frac{1}{M}\right)^2 \lambda f^{\#2} \tag{4.12}$$

λ the wavelength of the light, $f^{\#}$ the lens aperture and M the image magnification defined by

$$M = \frac{b}{v} \tag{4.13}$$

where b is the image distance, and v the object distance. The LIF measurement were done with an $f^{\#}$-number of 2.8, resulting in a focal depth of 0.6 mm, which is comparable with the depth of the light sheet. Most PIV measurements were done using $f^{\#} = 8$, resulting in a focal depth δz=5 mm. This is an order of magnitude larger than the light-sheet thickness.

4.5.4 Alignment of the cameras

To align the two cameras the following procedure was followed:

- First the two cameras are placed at the same distance at each side of the pipe. The distance from the pipe is determined by the required magnification and the lens.
- One of the cameras is aligned with the pipe as good as possible. This can be done by placing a grid at the centerline of the pipe or by measuring the vertical component of a turbulent flow, which should be zero on average.
- Align the second camera visually as good as possible. This can be done by looking at the display of the two cameras with a slow laminar flow present in the pipe, and check if particles enter and leave the field of view of the two cameras at the same time and position.
- Acquire a series of images with the two cameras running simultaneous with one of the YAG lasers in operation.
- Flip one of the two images horizontally (left/right).
- Do a cross correlation between the images of the two cameras. If the alignment of the cameras is good, the displacements resulting from the cross correlation are small. If the measured displacements are too big (larger than e.g. three pixels) the measured vector field can be used to correct the position of the camera.

A sketch of the camera positions with respect to the pipe and the optics creating the light sheet is shown in figure 4.15. In figure 4.18 an example of a vector field resulting from a cross correlation between the two cameras is shown. For reference a vector corresponding to a displacement of three pixels is drawn at the top of the image. All displacements except for some outliers (in this case only 1, but usually about 10) are smaller than 3 pixels. This means that the maximum misalignment of the cameras in the object plane is 0.14 mm in case of an image size of 45 mm. This is only 0.1 times the size of an interrogation area, and much smaller than the typical size of an eddy in the flow and therefore neglected.

4.5.5 DPIV system

To be able to do PIV measurements, besides a camera and a light source suitable particles are required as described injection 3.2. The particles used for the PIV measurements are Durcal particles with a nominal diameter of 5 μm and a density of 2.7 kg/l (Borleteau 2000). Only 1 gram of particles was added before the measurements. With a system volume of 350 l this leads to a volume fraction of 1.1×10^{-6}. This is almost equal to the maximum particle volume fraction which is acceptable as mentioned in 3.2.

It is checked if adding one gram of Durcal particles to the flow results in a suitable particle density. With the density and the particle diameter given, 1 gram

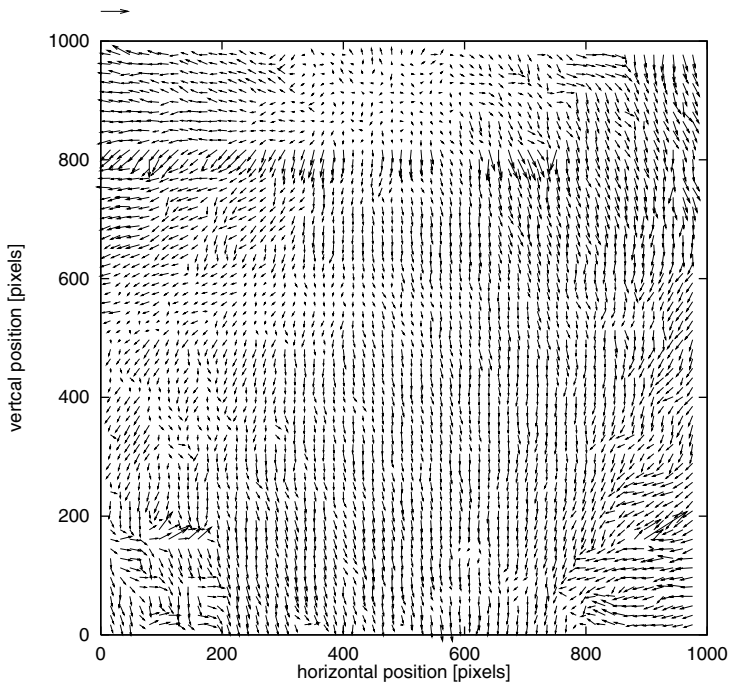

Figure 4.18: The misalignment of the two cameras. The vector at the top of the image has a length of 3 pixels. Mean length of the vectors is 0.94 pixels with an rms of 0.3 pixels.

of particles contains 6×10^9 particles. With a system volume of 350 liters a particle density of 1.6×10^7 particles per liter, so a mean number density of 16 particles per mm^3 is obtained. With a light sheet with a thickness of about 0.5 mm and an interrogation area of 1.6×1.6 mm^2, the average number of particles in each interrogation area is expected to be 21. This is larger than the minimum particle density as given by Keane & Adrian (1993).

To check if the particles are not too big, the settling velocity of the particles is computed and compared with the fluid velocity. The Stokes settling velocity v_s of the particles is given by

$$v_s = \frac{1}{18} \frac{\rho_p - \rho_w}{\rho_w} \frac{gd^2}{\nu}, \tag{4.14}$$

where v_s is the stokes settling velocity, ρ_p is the particle density, ρ_w is the density of water, ν is the kinematic viscosity of water, g is the gravitational acceleration and d is the particle diameter. The resulting settling velocity is 2×10^{-5} m/s, which is 4 ordes of magnitude smaller than the fluid flow velocity, and therefore negligible. Also the limitation for the time scale of the particle in relation to the time scale of

turbulence given by (3.5) is obeyed.

4.5.6 Scaling of the velocity data

The data processing program that we use, returns the measured particle displacement Δx in pixels. To obtain the velocity in meters per second the displacement in pixels should be multiplied by the size of a pixel d_r on the CCD chip and then be divided by the image magnification M times the time delay between the two exposures Δt:

$$u = \frac{\Delta x d_r}{M \Delta t}. \tag{4.15}$$

As mentioned in section 4.5.3 the center to center spacing of the pixels on the CCD chip equals 9 μm, with 1004 pixels in the vertical direction. The time delay used during the measurements was 3.5 ms. The relation between displacement in pixels and velocities in meter per second therefore becomes (assuming a constant image magnification):

$$u = 5.03 \times 10^{-4} \Delta x \tag{4.16}$$

4.5.7 Outliers

As mentioned in section 3.2.5 not all particle displacements are estimated correctly and the result is so-called outliers. These outliers are detected using the median test also discussed in section 3.2.5. An example of the number of discarded vectors as a function of the threshold value is given in figure 3.8. Above a certain value of the discard level the number of discarded vectors increases rapidly. The threshold value used was chosen just above this value. Looking at the result after correction, this procedure detected most of the wrong vectors. As can be seen in figure 3.8, even at a very high threshold values still 20% of the vectors is marked as an outlier. Usually 5% outliers is seen as the upper limit of outliers at which a measurement is still useful. In the present data however, most outliers are caused by the reflection lines present in the recorded PIV images or are present near the right edge of the image, where due to the non-circular shape of the YAG-beams the overlap between the two PIV light sheets appears to be bad. The number of outliers in the central part of the tube is acceptable.

The procedure used to compute the velocity fields of which the results are presented in the next chapter is:

1. Do ordinary autocorrelation
2. Remove outliers as described above and replace them by linear interpolation
3. Do cross-correlation with same image using the results of step 2 for the image shift

4. Remove outliers as described above

The procedure and background of step 3 are presented in section 3.2.6.

4.5.8 LIF system

In front of the camera for the LIF measurements an extra shutter is placed to prevent damage of the CCD chip in the camera by the light of the YAG lasers during the combined PIV/LIF measurements. The CCD-arrays can be permanently destroyed when over-exposed. This is due to damaging of the amplifiers at the edge of the CCD-chip. (Roper Scientific, priv. comm.). Even with the CCD not activated, the high intensity of the reflections from the YAG laser can cause damage. The lens aperture of the camera for the PIV recordings is much smaller and therefore no problems are expected to arise for that camera. The shutter that we use, is an electro-optical FLC shutter, operated by a Displaytech model DR50 FLC driver. The same driver was used to operate the shutter in the Argon-ion beam (see 4.5.1).

4.5.9 Timing

The general timing diagram of the lasers and the cameras is given in figure 4.19. The

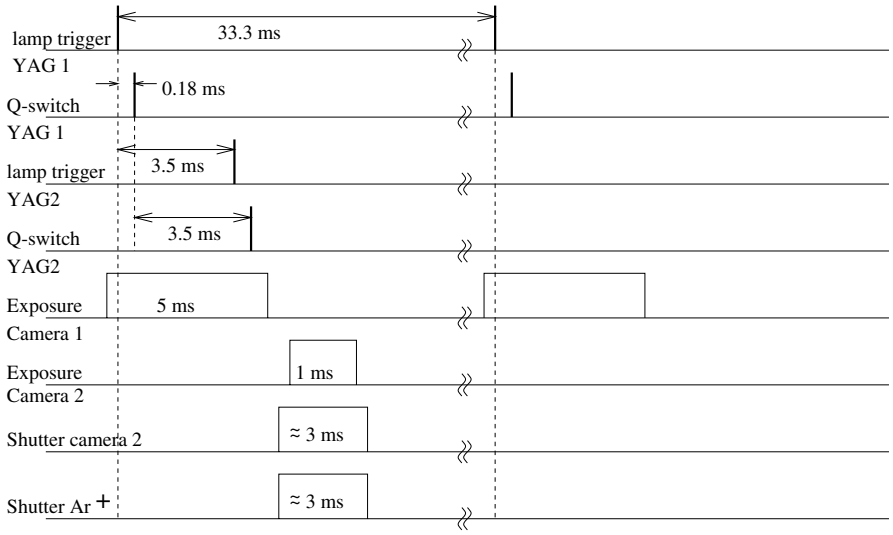

Figure 4.19: The general timing diagram used during the combined measurements.

timing of the YAG lasers is done with a five-channel digital delay/pulse generator (Stanford Research Systems, Inc. Model DG535). The PIV camera was triggered

by one of the channels of the five-channel digital delay/pulse generator. As the exposure of the cameras takes place just before the trigger signal, the trigger pulse for the PIV camera was placed 0.5 ms behind the lamp trigger of the second YAG laser pulse. The pulse for the shutter in the beam of the Argon-ion laser was generated using a WAVETEK pulse generator. The pulse generator was triggered by the timer box of the YAG lasers at the same time as the PIV camera. The second camera used for the LIF measurements was triggered by the end of the pulse for the Argon-ion laser.

Chapter 5

Results: point source measurements

In this chapter the results of the measurements on the point source geometry are presented. First we look at the velocity measurements, and afterwards the concentration measurements will be presented. Finally the combined PIV/LIF measurements will be discussed.

5.1 Statistics of the velocity field

5.1.1 Velocity field without injection mechanism

To test the flow facility and the PIV system, LDV and PIV measurements were done in the measurement section without the injection mechanism. This means that we are considering a fully developed turbulent pipe flow. If at the measurement position the flow is indeed fully developed and the PIV system is working correctly, the results of the measurements should agree with other measurements and computations of the same flow, at the same Reynolds number (5300).

The results are shown in figure 5.1. The results shown are the data points in the upper and the lower half of the pipe, with the points of the lower half mirrored with respect to the centerline of the pipe. The result shows that our data for the velocity profile are symmetric with respect to the centerline. Our measurements are in the same figure compared with previously done PIV (Westerweel *et al.* 1996) and LDV (Tahitu 1994) measurements, and with results from a DNS (Eggels *et al.* 1993). In the mean velocity profile the size of the error bars is of the order of the size of the symbols, and can therefore hardly be seen. It follows that for the mean velocity all the results agree very well with each other within the statistical error

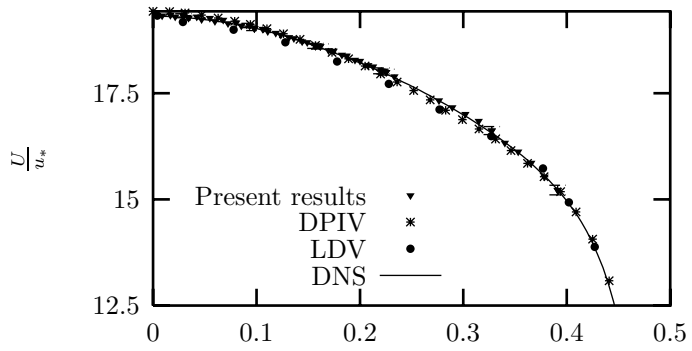

(a) mean velocity

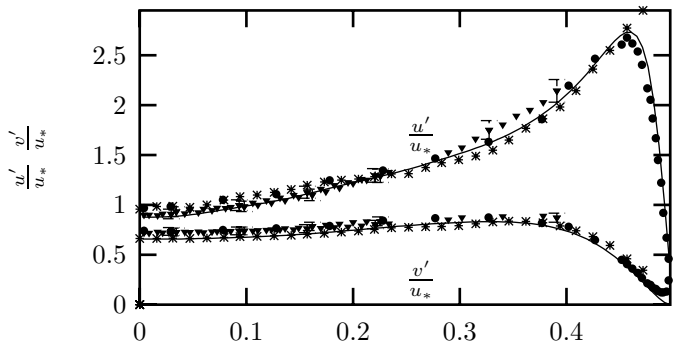

(b) turbulence intensity

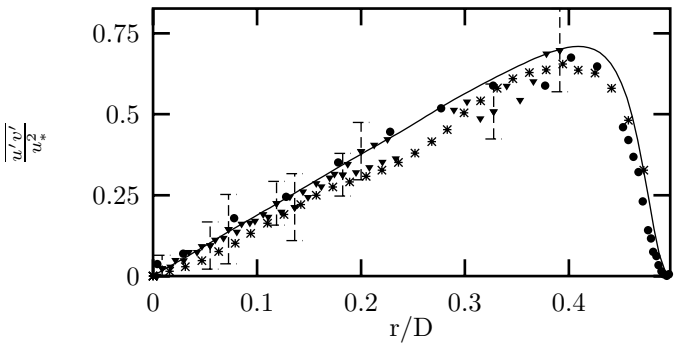

(c) Reynolds stress

Figure 5.1: The turbulent velocity profile of the pipe flow without injection mechanism in the measurement section. The present results are compared with previously done PIV (Westerweel *et al* 1996) and LDV measurements (Tahitu 1994) and with a DNS (Eggels *et al.* 1993). Figure (a) shows the mean velocity, figure (b) shows both the axial and the radial rms velocities, and figure (c) the Reynolds stress.

Table 5.1: A overview of the experimental conditions.

label	Pos. (D)	Re	$u*$ (m/s)	T (^oC)	Φ-inj. (mm^3/s)
PIV/LIF					
P1	0.5–1.5	$5.23 * 10^3$	$7.02 * 10^{-3}$	24.6	74
P2	1.5–2.5	$5.30 * 10^3$	$7.11 * 10^{-3}$	23.6	74
P3	2.5–3.5	$5.25 * 10^3$	$7.05 * 10^{-3}$	23.3	75
P4a	3.5–4.5	$5.28 * 10^3$	$7.08 * 10^{-3}$	23.8	74
P4b	3.5–4.5	$5.28 * 10^3$	$7.08 * 10^{-3}$	21.1	74
P5	4.5–5.5	$5.30 * 10^3$	$7.02 * 10^{-3}$	21.9	74
LDV					
LDV pos. 1	2.0	$5.4 * 10^3$	$7.3 * 10^{-3}$		0
LDV pos. 2	4.0	$5.0 * 10^3$	$6.9 * 10^{-3}$		0

of the PIV measurements. Our measurements for the radial turbulence intensities are a few percent higher than the results of the DNS, but they are in agreement with the LDV measurements of Tahitu. This difference could be due to a resolution problem in the DNS or due to the presence of some noise in the measurements.

For both the rms-velocities and especially the Reynolds stresses, the scatter in our data increases significantly for radial positions larger than 0.25D. This is caused by the reflections mentioned in section 4.3.3. Outside the regions where the reflections are present the PIV are reliable and in good agreement with the other observations.

5.1.2 Velocity field with injection mechanism

Combined PIV/LIF measurements were done at 5 positions downstream from the injection point. The measurement positions, are listed in table 5.1. An overview of the experimental parameters is given in table 5.2. In this subsection the results of the PIV measurements are presented. In particular the influence of the injection mechanism on the velocity field is investigated. The results of the PIV measurements are compared with LDV measurements done at two positions downstream from the injection point. To be able to investigate the differences with the velocity field without injection mechanism, the results are compared with the results of the DNS (Eggels *et al.* 1993).

For each measurement position, the PIV measurements produce a mean velocity profile, both a radial and an axial rms velocity profile, and a turbulent stress profile following the method described in section 3.2.7. The results are shown in figure 5.2. We see that data are lacking between -0.30D and -0.25D and between 0.25D and 0.30D. The reason is the reflection in the PIV images which are so strong that no data could be collected. For a description of the origin of the reflections see section

Table 5.2: Experimental parameters.

pipe diameter	50	mm
light sheet depth	0.8	mm
exposure time delay (PIV)	3.5	ms
exposure time (LIF)	1.5	ms
injection concentration	10	mg l^{-1}
recording frequency	30	Hz
total recording time (1608 frame pairs)	51.6	s

4.3.3. Similar effects were found in the experiments without injection. In addition to the PIV measurements we also did LDV measurements. The results of both measurement techniques are compared in figure 5.3. In this figure the mean and rms velocities are shown for measurement positions P2 and P4 (see table 5.1). In the center region of the tube the results are statistically the same. Near the edges of the tube there are some differences which could be caused by the slight difference in Reynolds number or a difference in radial alignment.

Figure 5.2a shows a deviation of the measured profiles from the undisturbed velocity profile resulting from the DNS. In figure 5.1 it was found that this DNS profile is in good agreement with the undisturbed velocity profile. The differences between the results from our measured velocity profiles with the DNS is therefore caused by the disturbance of the injection needle on the velocity profile. This agrees with our setup. For the upper half of the pipe (negative r values) where the injection mechanism is located, the velocities are slightly lower than the velocities obtained from the PIV measurements. For the lower half of the pipe the opposite is the case. The defect on the profile is in the upper half of the pipe larger than in the lower half of the pipe. This is caused by the fact that in the upper half of the pipe the velocity profile is disturbed by the wake of the vertical part of the injection needle. This wake decays only slowly with the downstream position of the pipe and seems to be present for all measurement positions.

Each curve in figure 5.3 is the result of averaging over the streamwise length of the measurement positions. The rms-velocities are computed using the mean velocities in this figure. Just behind the injection point, however, the velocity field is not homogeneous in the streamwise direction, so the mean velocity is not constant in the streamwise direction. The velocity rms profiles are therefore over-estimated. In figure 5.4 the 2D mean velocity profile in the whole measurement domain at the first measurement position P1 behind the injection point is plotted. It can be seen clearly that the disturbance from the injection needle decreases as a function of downstream position. In the 2D graph the region where reflections occur is excluded although still some disturbances are evident near the edges of the excluded region.

In figure 5.5 the u-rms velocities based on the streamwise averaged mean velocity is compared with the rms velocities based at the local mean velocities at

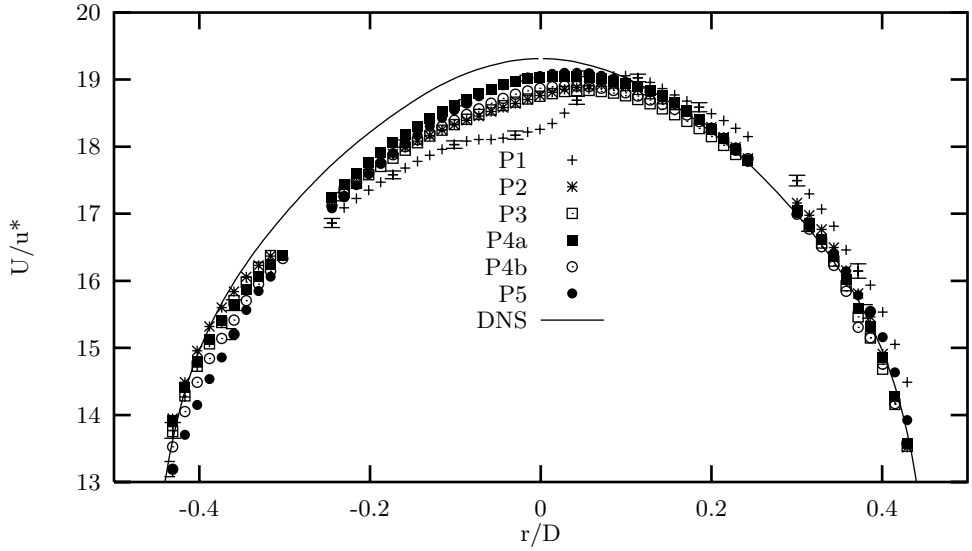

(a) mean velocities

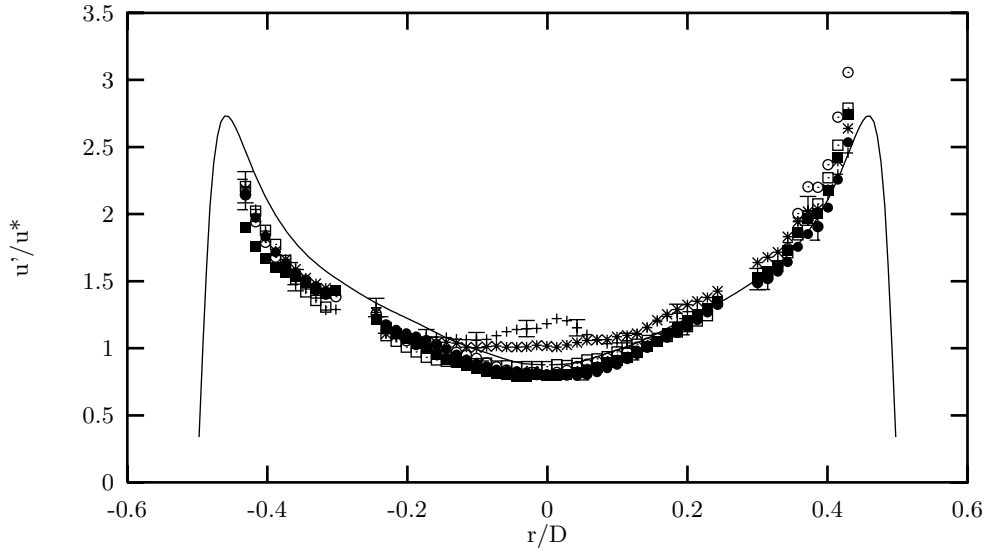

(b) axial rms velocities
Figure 5.2 (continued)

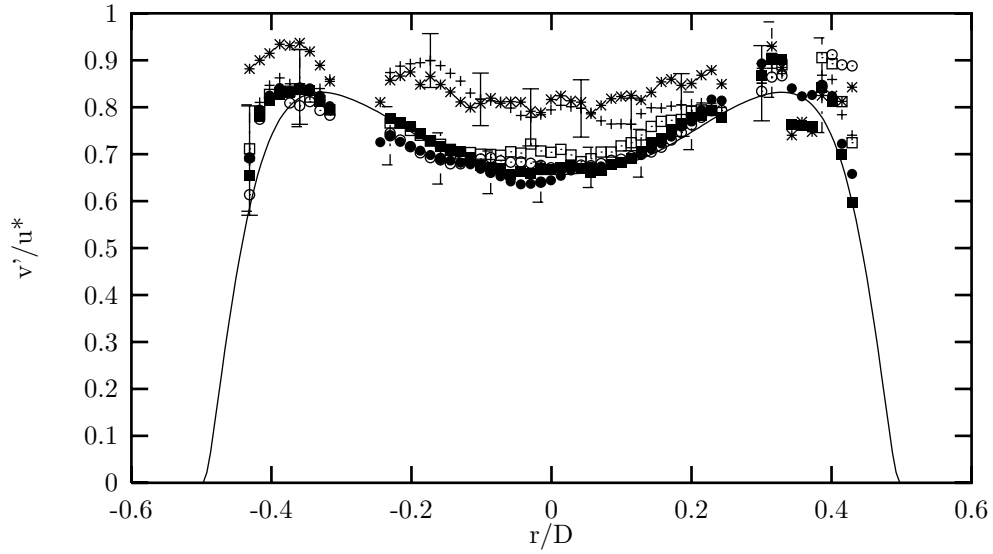

(c) radial rms velocities

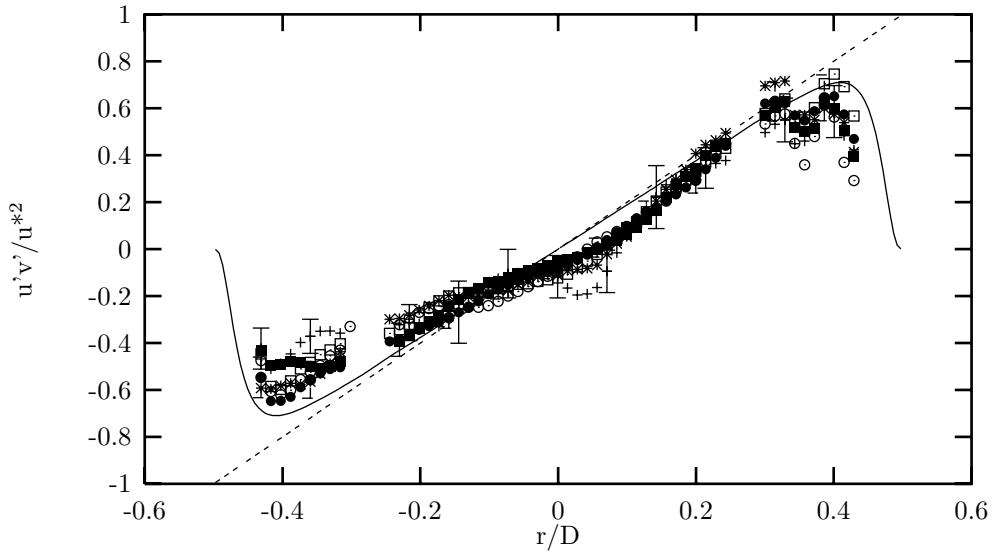

(d) Reynolds stresses

Figure 5.2: The velocity statistics at several distances from the injection point. In a the mean velocity profiles are given, b shows the rms velocities, c shows the measured Reynolds stresses. All measurements are compared with a DNS and DPIV measurements without injection. Symbols and legend refer to table 5.1.

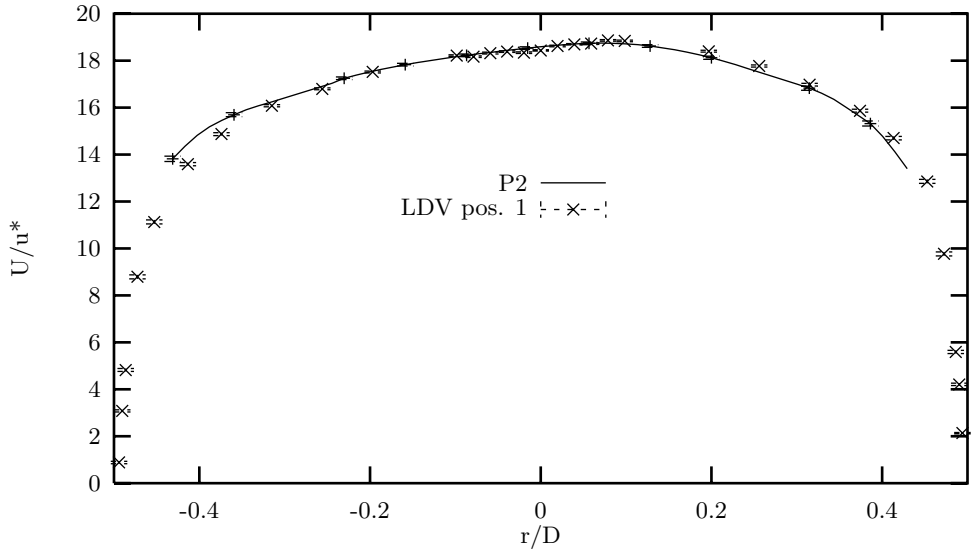

(a) mean velocities at P2

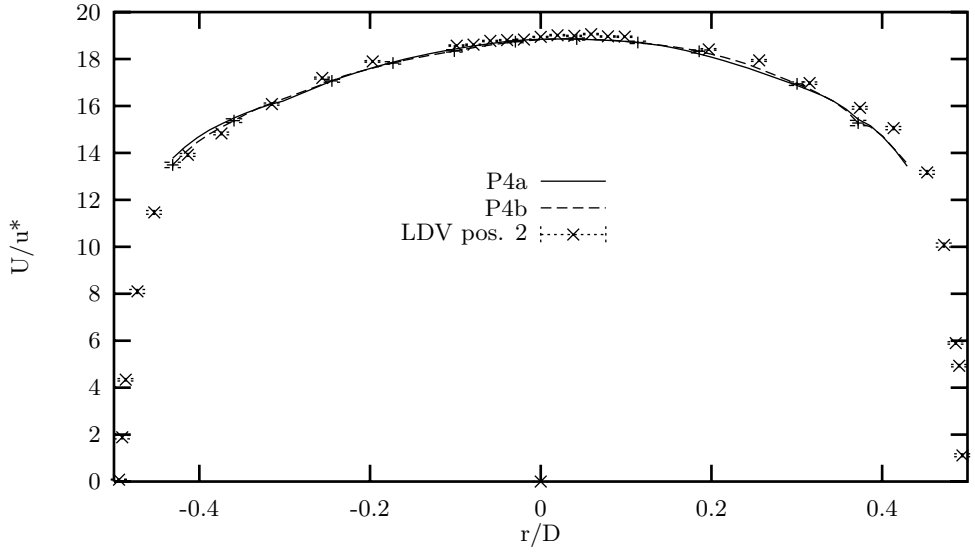

(b) mean velocities at P4
Figure 5.3 continued

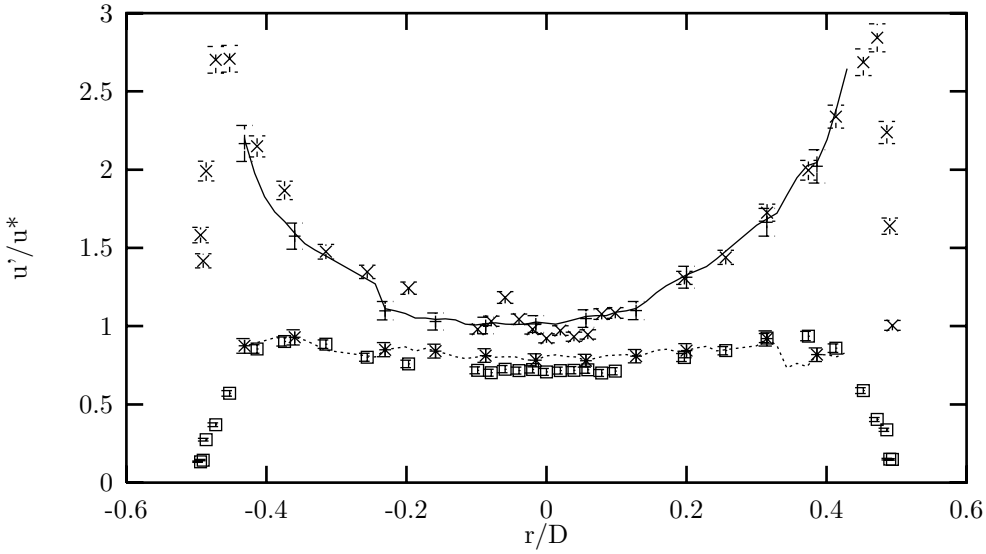

(c) rms velocities at P2

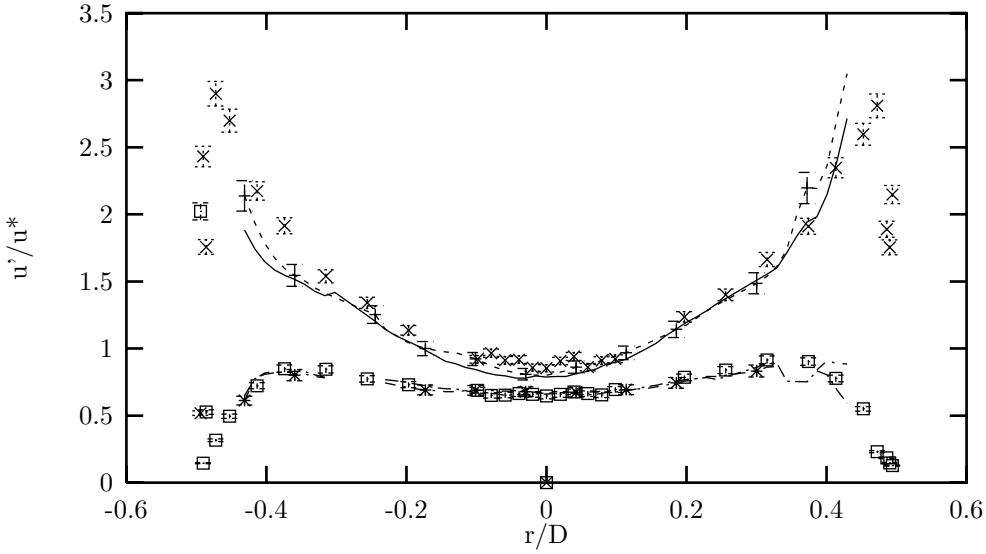

(d) rms velocities at P4

Figure 5.3: Comparison of the the results from PIV and LDV measurements. For measurement positions P2 and P4 both mean and rms velocities are shown.

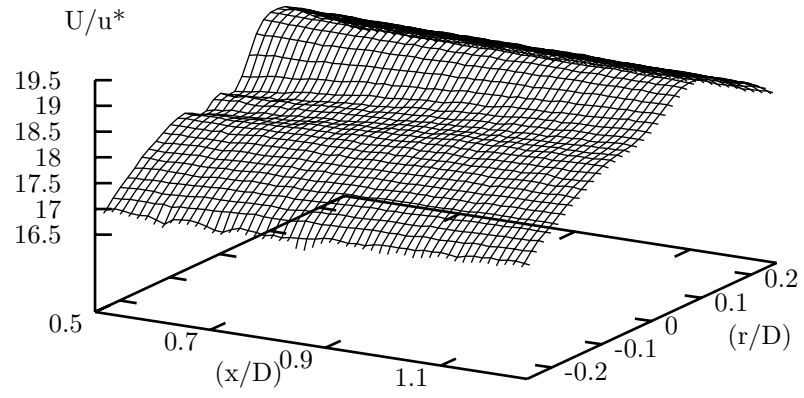

Figure 5.4: The two dimensional velocity profile for $\mid r \mid /D \leq 0.25$ between 0.5 and 1.25 pipe diameters behind the injection point (measurement position P1).

4 measurement positions in the streamwise direction. As can be seen the locally computed rms velocities, at most positions, are lower than the global rms values. The only position at which the local u-rms values are significantly higher than the rms values based on the streamwise averaged mean velocity is near the centerline, for positions near the injection devise. These high rms-values are attributed to the wake of the horizontal part of the injection needle.

In figure 5.6 the two dimensional rms-field in the central part of the pipe at measurement position P1 is shown. The local rms values show a clear decrease in the downstream direction. This would be due to the decay of the wake of the horizontal part of the injection needle as has been discussed in relation to figure 5.4.

5.2 Statistics of the concentration field

Next we discuss the statistics of the concentration field of the point source, obtained with help of the LIF measurements. As discussed before the concentration measurements were done simultaneously with the PIV measurements.

The most important parameters for the LIF measurement are listed in table 5.2. The injection concentration is determined by adding a precisely determined

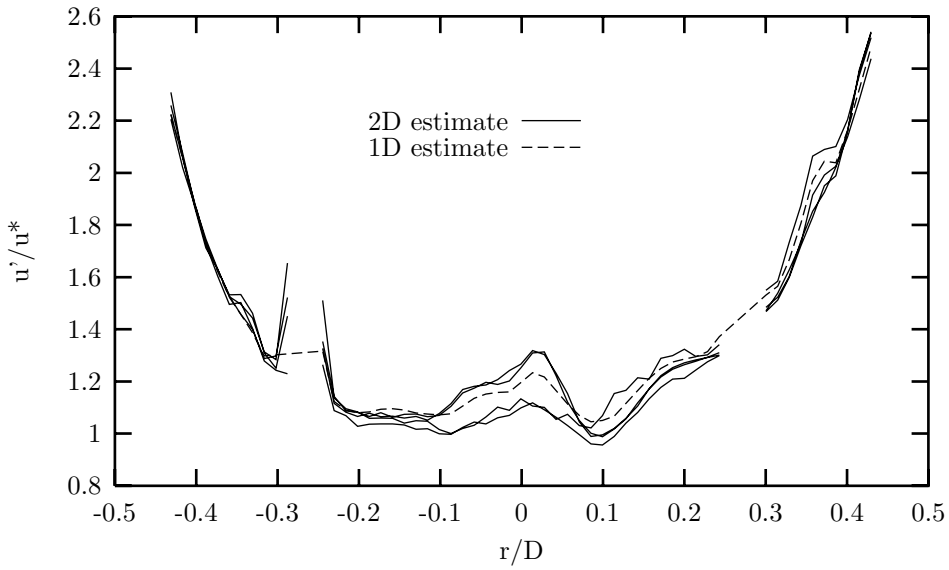

Figure 5.5: The u-rms velocities based on a single mean velocity (1D estimate) compared with the local rms velocities at 4 measurement positions in the streamwise direction (2D estimate).

Table 5.3: An overview of the most important parameters of the LIF measurements.

injection concentration	10 mg/l
uniform concentration	0.07 mg/l
LIF exposure time	1.5 ms

amount of fluorescein to a known amount of water such that a concentration of 10 mg/l is obtained. For the calibration of the LIF measurements a solution with a uniform concentration of 20 mg/l is made. From this solution 90 ml is added to the secondary flow loop as described in section 4.3. The exact uniform concentration is not known, since the volume of the secondary flow loop is difficult to determine due to the presence of a pump with unknown volume and some other parts of the setup of which the exact volume is not known. However, our estimation for the uniform concentration is 0.07 mg/l.

5.2.1 Mean concentration

From the two dimensional LIF data we computed the concentration statistics using the technique described in section 3.3.2. Results for the centerline concentration

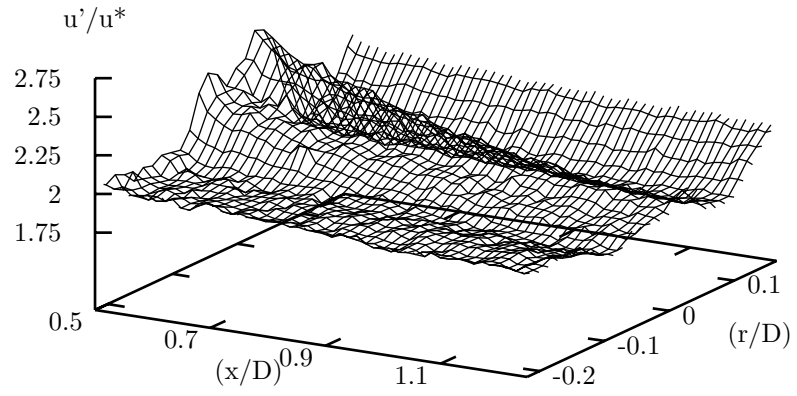

Figure 5.6: The two dimensional profile of the rms velocity fluctuations at the first measurement position. The downstream position is at the right hand side. Results are shown for $0.5 < x < 1.25$ and $-0.25 < r/D < 0.15$.

and the spreading of the plume are compared with the results of a DNS of a flow with the same geometry (Brethouwer 2001) and the results of the simple mixing model presented in section 2.4.1. Main differences between the DNS and the experiments are the absence of disturbances in the velocity field due to an injection mechanism and a much lower Schmidt number in the DNS (1 in the DNS, 2075 in the experiments). The effect of these two differences of the DNS and LIF on the mean concentration at the centerline are assumed to be small.

The centerline concentration is estimated by fitting the a Gaussian profile through the measured mean concentration profile at each measurement position. This mean concentration field was computed by first computing the concentration fields on a pixel to pixel to base. The resulting concentration fields are locally averaged on the same grid as the PIV fields. These locally averaged concentration fields are averaged over time. From the resulting Gaussian profile both the centerline concentration and the width of the plume are estimated. In figure 5.7 the centerline concentration is shown in the first five pipe diameters behind the injection point. The results are compared with the results of a DNS done by Brethouwer *et al.* (2000). Starting from $x/D \approx 1$ experiments and the DNS data agree very well. For $x/D < 1$ the DNS data underestimate the experiments. This is caused by the fact that in the DNS the small point source used in the experiments could not be resolved numerically.

As can be seen the centerline concentration follows a $1/x^2$ curve over the first two and a half pipe diameters behind the injection point, as expected from the mixing model presented in section 2.4.1. After 2.5 pipe diameters the slope of the log-log plot becomes less steep and a $1/x$ curve can be fitted as expected from the theory, assuming homogeneous turbulence near the centerline of the pipe. If a $1/x$ curve is fitted through the DNS data for $x/D > 2.5$ the coefficient of the curve is 0.30. If the same is done for the LIF data the coefficient becomes 0.31. The difference is only 3%. Concidering the inaccuracy in the LIF measurements, this difference is not significant. The inaccuracy in the LIF measurements is clearly demonstrated by the difference in the results for measurement P4a and P4b, which can be seen in figure 5.7 between x/D=3 and x/D=4. These differences can be caused by a slightly different injection or calibration concentration and a small difference in the position of the injection needle.

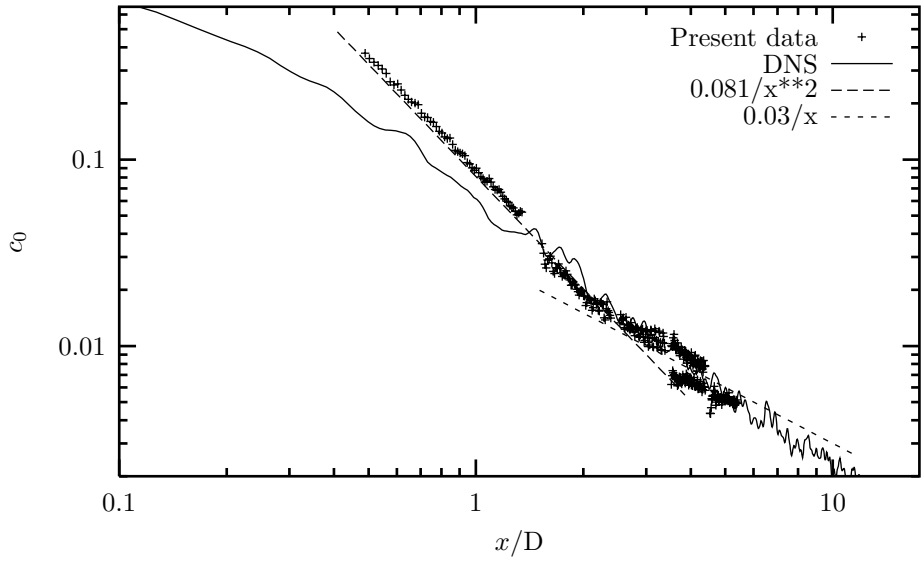

Figure 5.7: The mean concentration at the centerline as function of the distance from the injection point. Besides the measurements a $1/x^2$ fit through the measurements and the results of a DNS (Brethouwer *et all* 1999) are shown.

In figure 5.8 we show the dispersion parameter σ of the mean concentration distribution as a function of the distance from the point source. The measurement results and the DNS agree very well for positions $x/D > 1$ behind the injection point. The line resulting from the DNS lies always within the scatter of measured data. The differences for small distances behind the injection point are caused by differences in the initial conditions as mentioned above. In the simulation the initial

concentration profile has a Gaussian shape with a standard deviation of 8.5×10^{-3} D. This is done because the numerical scheme used is not able to handle large concentration gradients. As described in section 4.3.2, in the experiments fluid with a constant fluorescein concentration is injected through an injection device with a diameter of approximately 0.01 D, so that the source strength can be considered constant. Brethouwer (2000) defines for the DNS the width σ of the mean concentration profile as

$$\sigma^2 = \frac{1}{2}\frac{\int_0^\infty r^3 \overline{c} dr}{\int_0^\infty r \overline{c} dr} \tag{5.1}$$

With this definition the width of the initial cylindrical concentration profile is 2.5×10^{-3} D. For the difference in initial spreading between the DNS and the experiments a correction can be applied by using a slightly different virtual origin of the scalar source. There will however always be a difference between the experiments and the DNS, due to the fact that in the numerical simulation the initial concentration profile has a Gaussian shape whereas in the experiments an uniform concentration is injected. Besides that the pipe flow is disturbed by the injection mechanism and this will also cause some difference with the numerical simulation. As can be seen in figure 5.8 the initial differences between experiments and simulations seems to disappear after 0.7 D behind the injection point.

For positions far downstream of the injection point the standard deviation obtained from the Gaussian fit through the measurement points will give a too high estimate for the spreading. This is due to the fact that the experimental value for the standard deviation of the concentration profile should be based on a profile with a finite width due to the finite size of the pipe. The maximum spreading according to the definition in equation 5.1 is found for a uniform concentration profile in the pipe cross section. This maximum value becomes equal to 0.25 D. If for $x/D > 2.5$ the expected relation for the width as function of the distance is fitted for both the DNS and the LIF data, the width of the plume in the DNS becomes 7% larger than the width obtained in the experiments. Owing the large scatter on the data, this difference might be not significant.

In figure 5.9 we show the concentration profiles scaled with the centerline concentration and the dispersion parameter as determined above. Only the first three measurement positions behind the injection point are shown. As can be seen there is a quite good fit to the Gaussian similarity profile. The scatter in the data increases for further downstream position. If a Gaussian profile is fitted to the scaled data over the range $-4 < r/\sigma < 4$, the rms of the residuals is 0.030. For positions P2 and P3 this increases to 0.057 and 0.065 respectively. This is small compared with the statistical error at the centerline which is about 0.2 at measurement position P2 and P3. Based on these results, it can be concluded that for the mean concentration the DNS and the LIF measurements agree well. The results are also in agreement with the simple mixing model presented in 2.4.1. The influence of the molecular

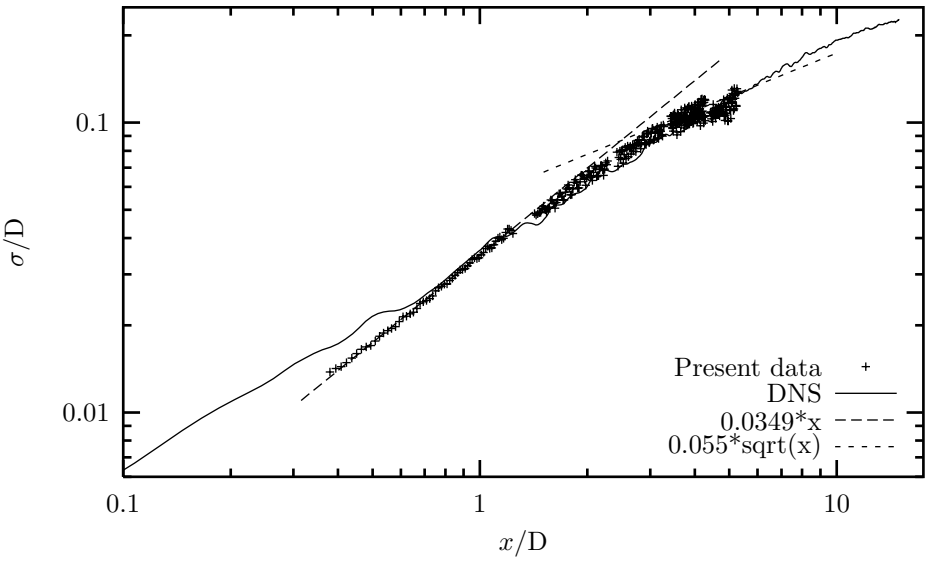

Figure 5.8: The standard deviation of the width of the plume as function of the distance to the injection point. Besides the measurements the result of the DNS and the fitted curves originating from the simple mixing model are shown.

diffusion on the macro mixing is therefore negligible, which was expected.

In figure 5.10 we show the decay of the centerline concentration and the dispersion parameter for two different Reynolds numbers. The Reynolds numbers are 5300 and 10000. Data are given only for the region from 0.5 to 2.5 pipe diameters behind the injection point. For positions further from the injection point the data for the highest Reynolds number are not reliable enough to be presented since the scatter on the data was of the same order of magnitude as the data. Due the fact that the turbulence intensities in the center region of the pipe for the two Reynolds numbers are almost equal, the differences in macro mixing behavior is expected to be small. The differences in centerline concentration can be caused by a slightly different fluorescein concentration during injection, or during calibration. Also the misalignment of the light sheet has an influence on the measured centerline concentration. Maximum differences in uniform concentration are about 5%. Since the spreading and the shape of the centerline decay over one measurement position is not influenced by the absolute concentrations, these differences are accepted. The difference in dispersion parameter for small values of x/D is probably caused by a small misalignment off the light sheet with respect to the plume, causing a slightly lower measured spreading of the plume for Re = 5300.

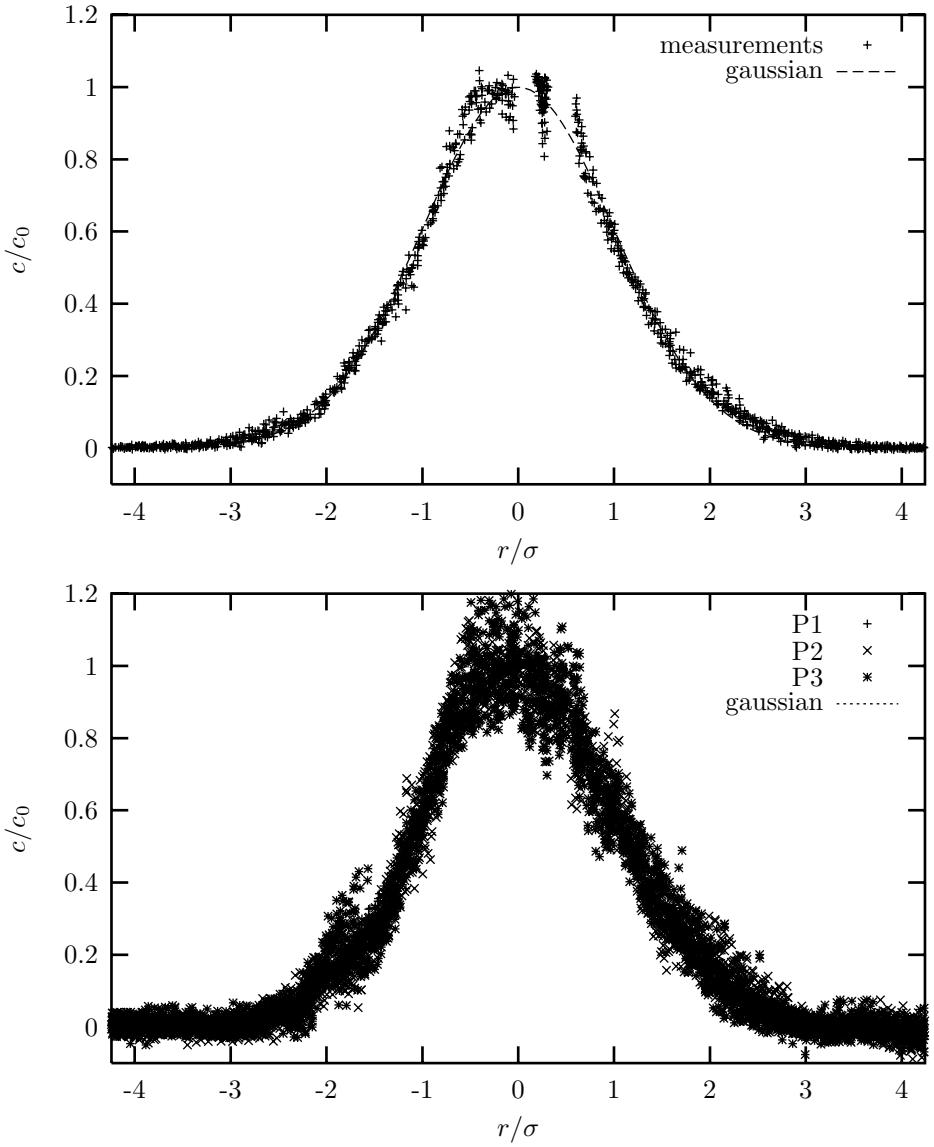

Figure 5.9: The scaled mean concentration profiles at several distances from the injection point. In the upper figure the concentration profiles at the 61 streamwise positions of P1 are shown. In the lower figure the concentration profiles of P1, P2 and P3 are shown.

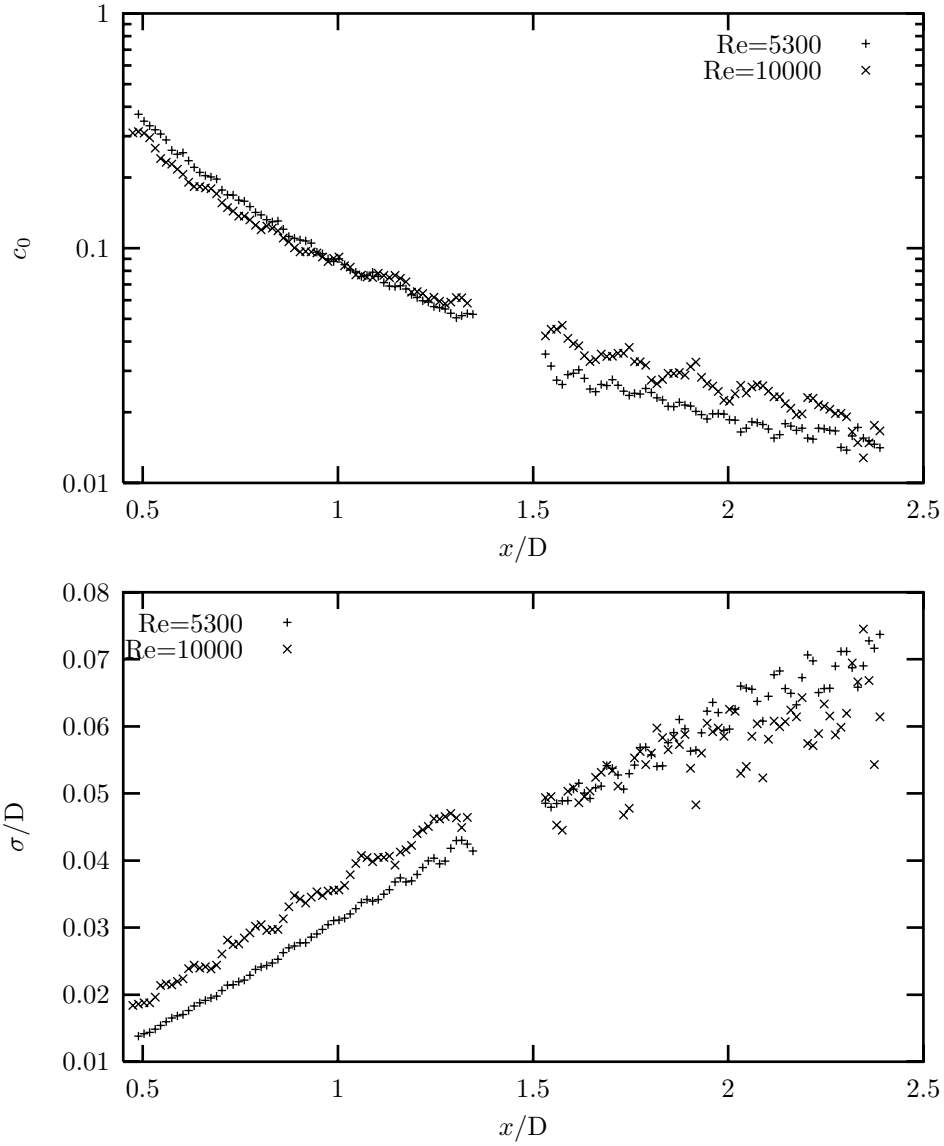

Figure 5.10: The decay of the centerline concentration and the spreading of the point source for Reynolds number 5300 and 10000.

5.2.2 Concentration rms

For the first three measurement positions behind the injection we have computed the rms of the concentration fluctuations. The results are compared with the DNS data by Brethouwer. In the same way as for the mean concentrations we have also fitted these concentration rms data to a Gaussian profile. A concentration profile scaled with the resulting parameters for position P2 is given in figure 5.11. Due

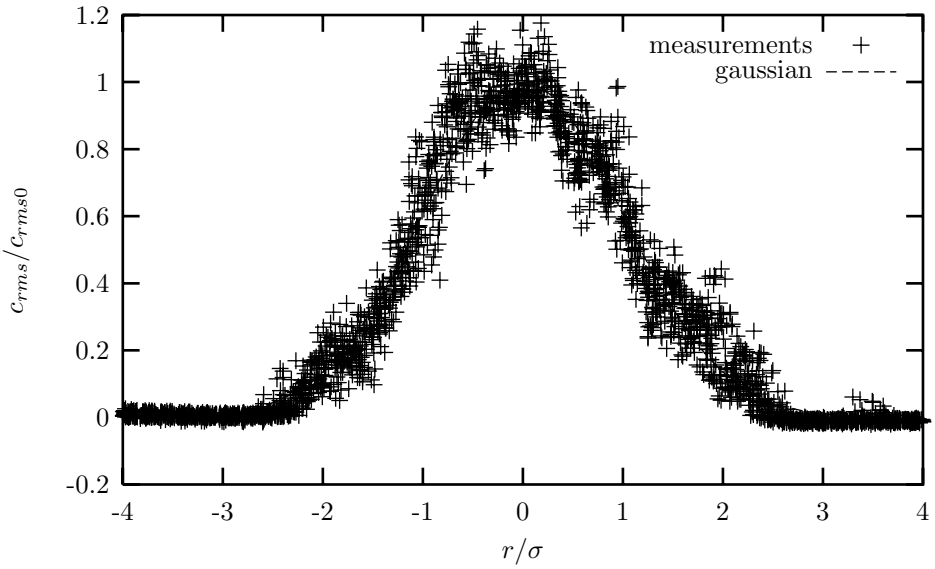

Figure 5.11: The scaled mean concentration rms profile for measurement position P2

to the intermittent character of the concentration (see section 5.2.3) and the high Schmidt number the expected concentration rms is about an order of magnitude larger than the mean concentration values.

In figure 5.12 the rms values on the centerline as obtained by the Gaussian fit, are plotted as function of the distance from the injection point. In figure 5.13 these values are divided by the centerline concentrations to obtain a relative centerline concentration rms. In figure 5.14 the two-dimensional profiles of the rms are shown, scaled with centerline concentration. The radial direction is scaled with the width of the plume determined from the mean concentration profile.

The concentration rms relative to the centerline concentration shows initially an increase with downstream position. This is in agreement with results presented by others. For instance Brethouwer (2001) presents the results of a DNS of a passive scalar in a turbulent pipe flow with a Schmidt number of 0.7 (see figure 5.15). From figure 5.12 it follows that in our measurements the ratio between the rms and the

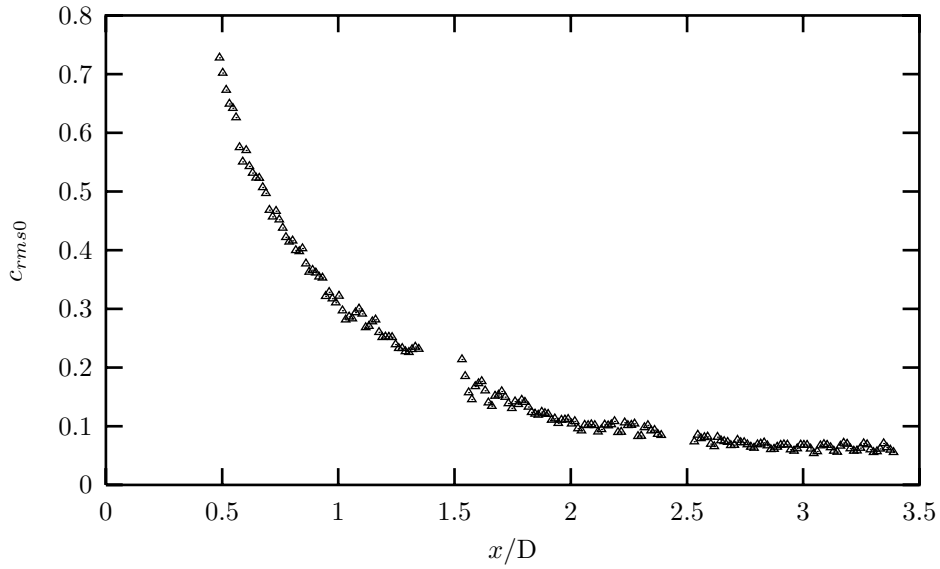

Figure 5.12: Centerline values of the rms concentration fluctuation c_{rms0} as a function of the distance from the injection point.

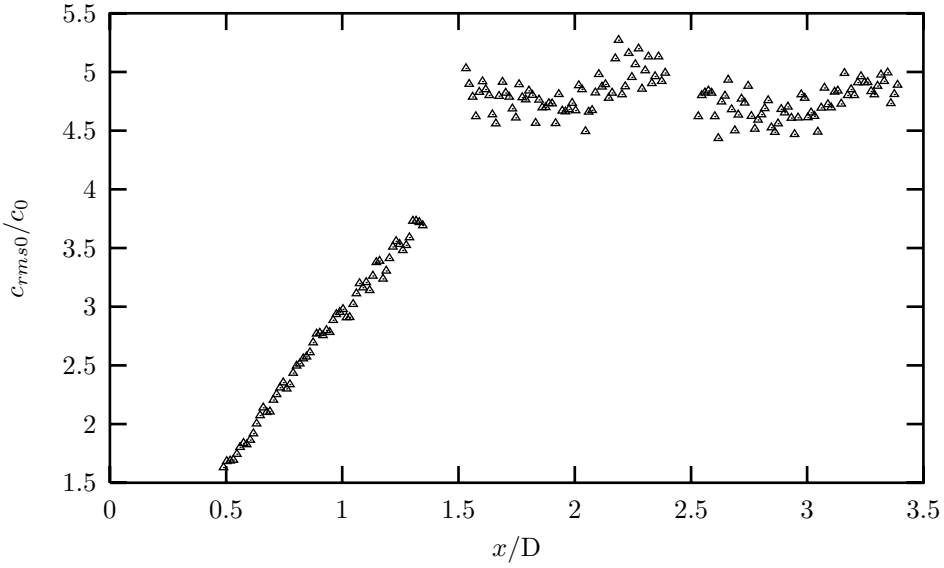

Figure 5.13: Centerline values of the relative rms concentration fluctuation c_{rms0} as a function of the distance from the injection point.

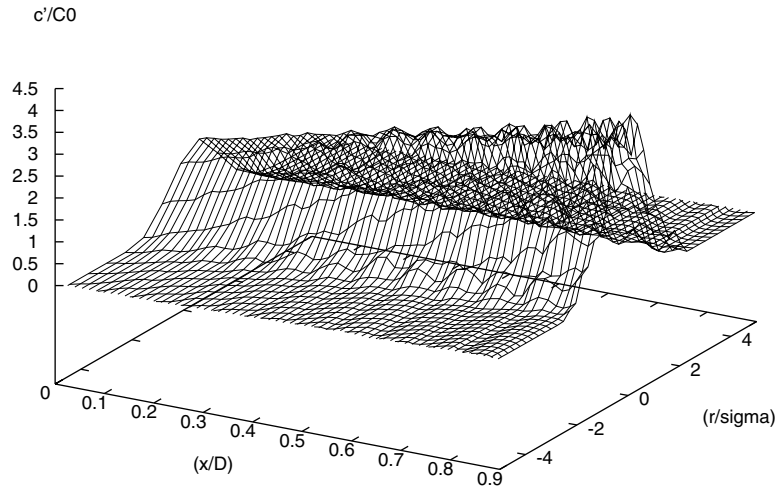

Figure 5.14: A two dimensional representation of the concentration rms scaled with the centerline concentration.

mean centerline concentration increases from 1.5 at 0.5 diameter after the injection point to 5 at 3.5 diameters. In the computations of Brethouwer this ratio increases

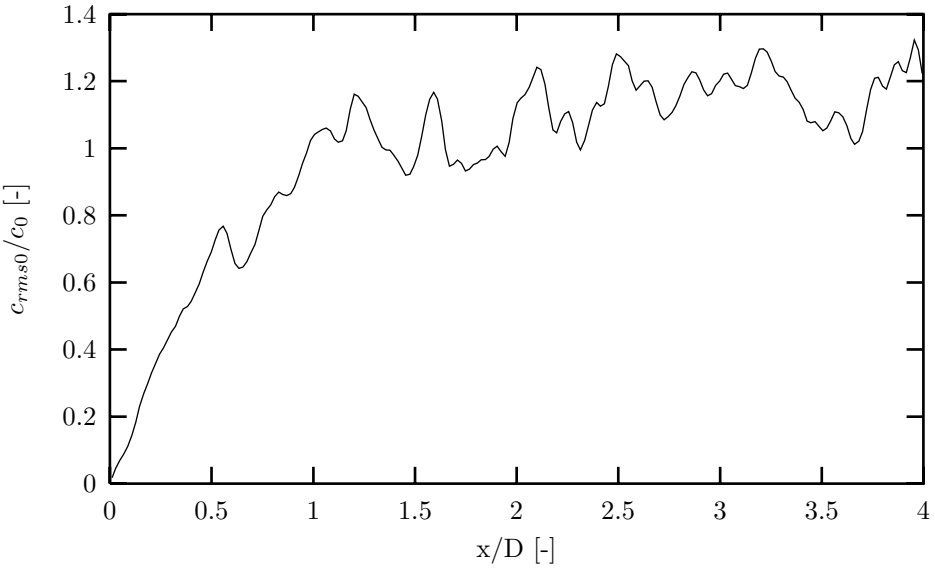

Figure 5.15: Centerline values of the relative concentration rms as function from the distance from the injection point as presented by Brethouwer (2001).

from 0.7 to 1.3 over the same region. In other words our rms values are much larger than those obtained from the DNS. This difference in relative concentration rms is caused by the difference in Schmidt number between the computations and the measurements.

5.2.3 Intermittency

As was shown in the previous section, the rms of the concentration in a large part of the measurement domain is larger than the mean concentration. One of the reasons for this high concentration rms and therefore for the poor convergence of the concentration statistics is the high level of intermittency of the concentration field. For high Schmidt number flows, the decay of the mean concentration in the radial direction is not due to lower instantaneous concentration values but mainly due to a decay of the probability to find fluorescein at a certain position. This phenomena can be described using the intermittency of the concentration signal. Let us therefore consider the intermittency I, which is defined as the probability of

the concentration c to be larger than a certain threshold value ϵ_c, so:

$$I = p(c > \epsilon_c). \tag{5.2}$$

The threshold value that was chosen is only slightly larger than the amplitude of the background noise of the concentration signal. The intermittency profile shown in figure 5.2.3 is an average over the streamwise direction of measurement position P2. In the same figure we also plot a scaled mean concentration profile computed from the same data. The data are scaled such that they have the same magnitude as the intermittency data. In the scaled concentration profile shown, the difference between the odd and even lines of the camera can be seen. Due to a difference in background grey value between odd and even lines there is a small offset between the values obtained. We could have corrected for this effect by, in this case, shift the values of the even lines up, such that outside the plume the concentration is zero. As can be seen the shape of the intermittency profile and the measured concentration profile is the same. It can also be seen that at the centerline only concentrations are measured during 4% of the total measurement time. Towards the cylinder walls this percentage decreases to zero. The threshold value for the concentration which was used to determine the intermittency curve shown, was 3 times the mean concentration at the centerline. This however does not mean that a lot of samples containing concentration are neglected. If the mean centerline concentration is divided by the intermittency at the centerline an estimation can be made of the mean concentration of the samples containing fluorescein. This conditional mean concentration appears to be more that 8 times the threshold value used. Maximum concentration levels are even more then 30 times the threshold value. From this result it can be concluded that the concentration pdf of the measurements has probably the same shape for different radial positions with only a different height of the background noise peak.

It is not that surprising that this result is found. The turbulence around the centerline of a pipe flow is almost homogeneous, so a unit of dye containing fluid is statistically deformed in the same way everywhere. All points on the profile have almost the same distance from the injection point, so the time the fluid is deformed by the flow at a certain position downstream of the injection is almost equal for all radial positions. If no turbulent mixing would have been present the spreading of the plume by molecular diffusion would have been about 0.1 mm at the end of measurement position P2. This is at least 5 times smaller than the thickness of the light sheet. Due to the turbulence the original line of fluorescent dye, with a diameter of less than one millimeter, will be deformed into sheet like structures with a thickness which is much smaller than the original thickness of plume and the thickness of the light sheet. The measured concentration distribution is therefore probably largely determined by the light intensity distribution over the depth of the laser sheet.

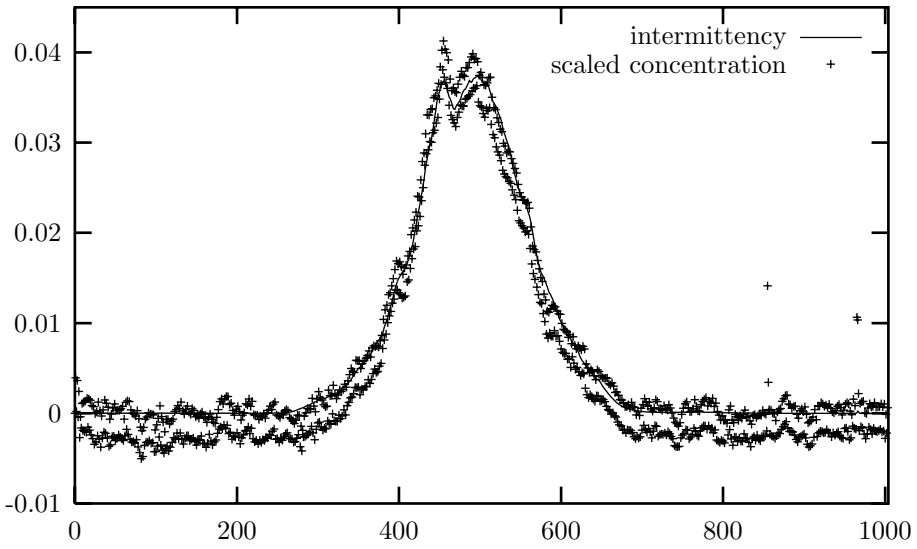

Figure 5.16: The intermittency profile of series P2 compared with the scaled concentration profile of the same series.

5.2.4 scalar dissipation

From the instantaneous concentration field we estimated the scalar dissipation, which is considered in this section. The reliability of the results for the scalar dissipation is discussed.

In figure 5.17 an example of a concentration structure and the corresponding estimation of the squared scalar derivative distribution ($\chi = \left[\frac{\partial c'}{\partial x}\right]^2 + \left[\frac{\partial c'}{\partial r}\right]^2$) is shown. Before computing the scalar derivatives first the data were filtered with the filter described in section 3.3.3. The concentration values corresponding to the isolines of the concentration structure increase linearly, the values corresponding to the isolines of χ increase exponentially. The isolines for χ span more than 3 decades. The χ structures are organized in sheet like structures as reported by Buch & Dahm (1996).

In figure 5.18 the mean scalar dissipation at the P2 position averaged over the complete series is shown. The dissipations are computed on a pixel to pixel basis after filtering with a low-pass filter as described in section 3.3.3.The resulting dissipation fields were locally averaged on a 16x16 pixel grid to reduce the statistical noise. In figure 5.19 the rms of the dissipation is given for the same measurement position. The figures do not show a smooth decrease as function of the downstream

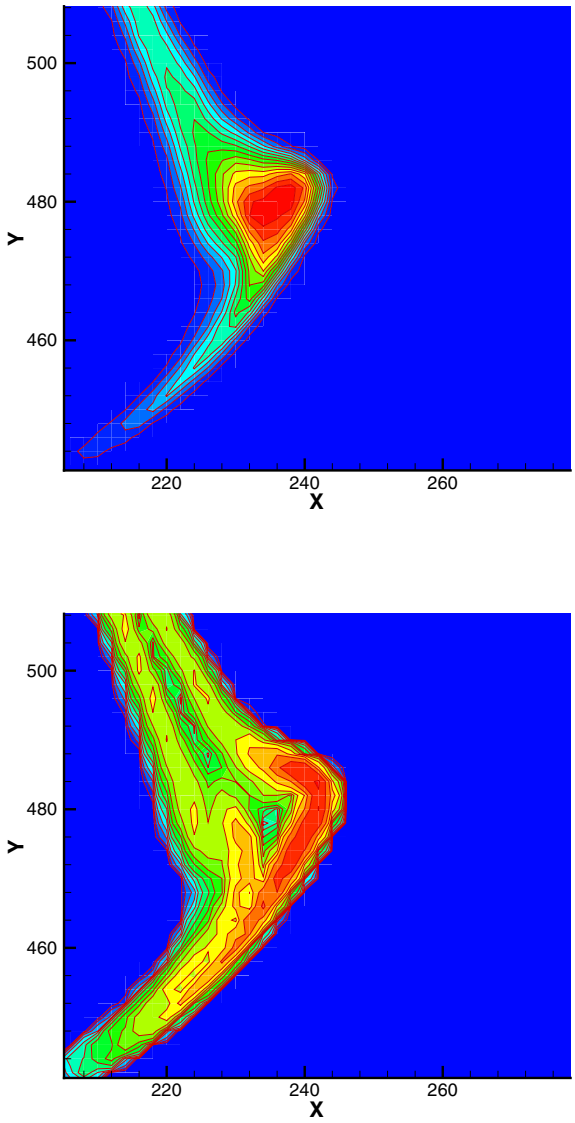

Figure 5.17: An example of a concentration structure and its squared scalar derivative distribution. The upper figure shows the concentration structure with contour lines with a linear increase. The lower figure shows the squared scalar derivative distribution with contour lines with an exponential increase.

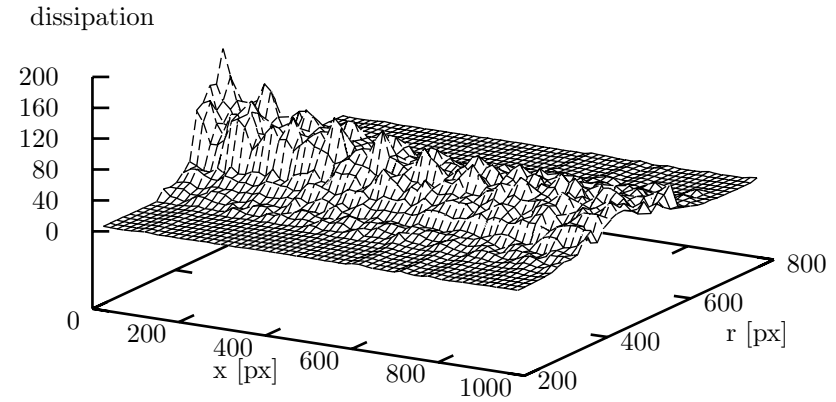

Figure 5.18: The mean scalar dissipation distribution at measurement position P2.

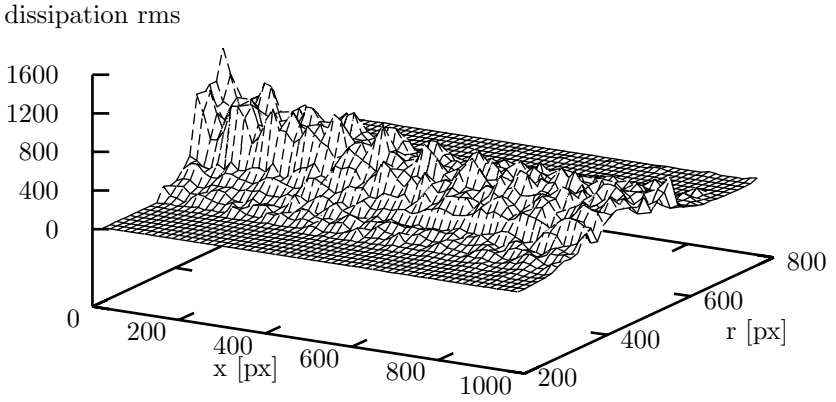

Figure 5.19: The scalar dissipation rms distribution at measurement position P2.

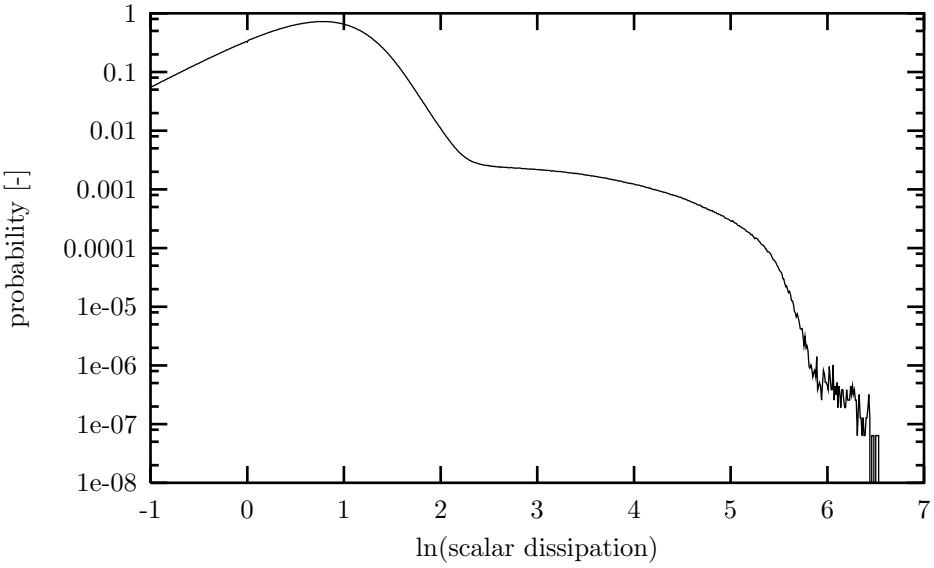

Figure 5.20: The pdf of the 2D scalar dissipation at measurement position P2

position, but are rather peaked. This is caused by the fact that due to the logarithmic behavior of the scalar dissipation the effect of individual structures with very high scalar derivatives can still be seen, so we are still far from a statistical convergence. This peaked behavior of the dissipation causes the rms-values of the scalar dissipation to be an order of magnitude larger than the mean dissipation values. In figure 5.20 the pdf of the logarithm of the dissipations of the same measurements is given. The large peak in the left hand side of the figure is caused by the background noise on the images. The shape of the scalar dissipation distribution is determined by a number of factors. The first is of course the actual scalar dissipation distribution. But besides that also the thickness and shape of the light sheet plays a role. Since the thickness of the light sheet is more than an order of magnitude larger than the Batchelor length scale, whereas the size of the pixels is about equal to the Batchelor length scale (see section 2.2.1), it is not possible to solve the complete range of concentration gradients present in the flow. The measured concentration gradient will therefore partially be determined by the orientation and location of the fluorescein structure inside the light sheet. Besides that it must be mentioned that only two of the three concentration gradients in the flow are measured, so not the real scalar dissipation but its 2D projection of the scalar dissipation is computed. The shape of the noise peak is determined by the frequency response of the filter used to suppress the noise (see section 3.3.3). The maximum scalar dissipation that

can be measured, is determined by the pixel size of the camera. Since the size of the pixels is almost equal to the Batchelor scale of the flow, the maximum concentration gradient measured is at most equal to the maximum of the measured concentration divided by the size of a pixel. Besides that the gradients in streamwise direction are reduced by moving unsharpness, since the movement of the fluorescein structures is more than one pixel during the LIF exposures.

5.3 Combined PIV/LIF measurements

The PIV and the LIF measurements presented in the previous sections were measured simultaneous. A sample of a pair of simultaneously recorded PIV and LIF pictures is shown in figure 5.21. No particle images can be seen in the LIF frame. The LIF measurements were therefore not affected by the PIV measurements. In the PIV frame the fluorescein structure can vaguely be seen. This is caused by the fact that the absorption of fluorescein is small but not zero at the wavelength of the YAG lasers as follows from figure 3.14. So there is some fluorescence due to light from the YAG-lasers and since no filter is placed in front of the PIV camera to remove this light, the structures appear in the PIV frames. The maximum of the grey values appearing in the LIF frame is about 230. The maximum of the grey values appearing in the PIV frame on the same position is about 130, which should be compared with the background grey value of about 50. These high values appear only in regions where the structures are in the streamwise direction, so the influence of the two exposures by the YAG-laser is summed. In order to test whether the influence of the LIF structure on the PIV measurements can be neglected, tests were done in which the LIF structure in the PIV frame is enhanced by adding a fraction of the LIF frame to the PIV frame. The resulting vector field is subtracted from the original vector field and the lengths of all vectors of this difference field are summed. This sum is a measure for the difference between the two fields. Besides that the effect on the number of outliers detected is investigated. As expected the difference in length of the original vector field and the vector field with a fraction of the LIF image added grows as a function of the added fraction of the LIF-frame as shown in figure 5.22.

If the number of outliers is plotted as a function of the added fraction of the LIF image, an unexpected result is found, shown in figure 5.23. The number of outliers detected in the images decreases as a function of the added fraction. Only after adding the LIF image 5 times to the PIV image the number of outliers increases again. If a number of vector fields is studied it is clear that the reduction of the number of outliers does not take place in the regions where fluorescein is present, but is spread all over the frames. On the contrary, in the regions where fluorescein is present, the number of outliers rather increases as function of the added fraction of the LIF image. First it was checked whether this phenomena of a decreasing

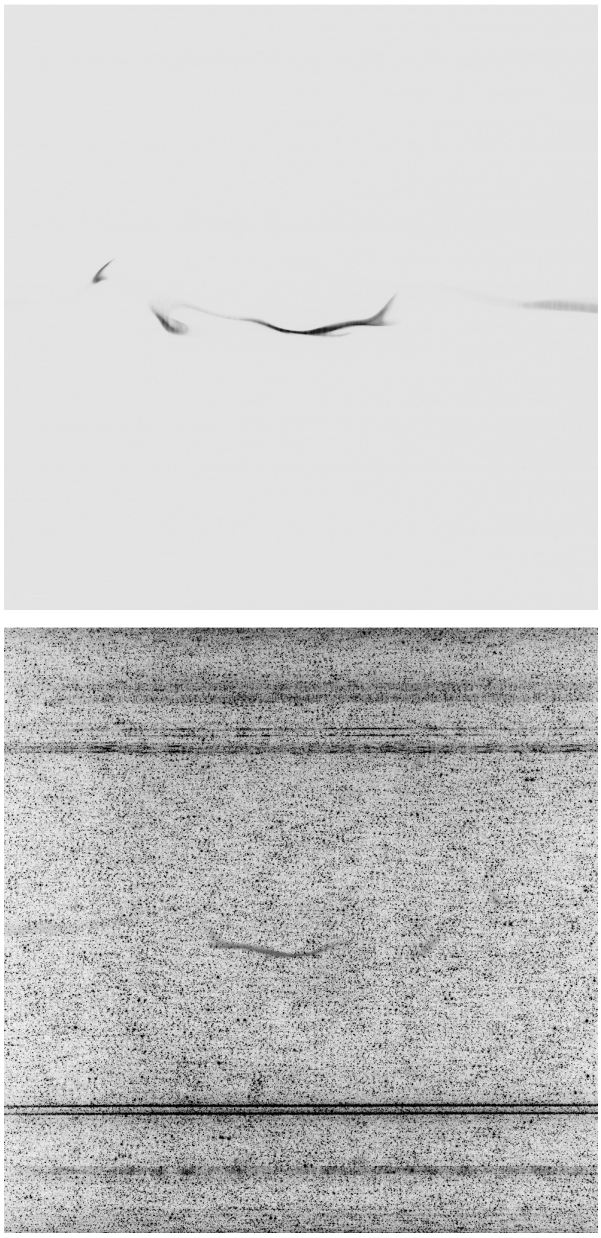

Figure 5.21: An example of a corresponding LIF and PIV frame. The upper frame is the LIF, the lower frame is the PIV frame.

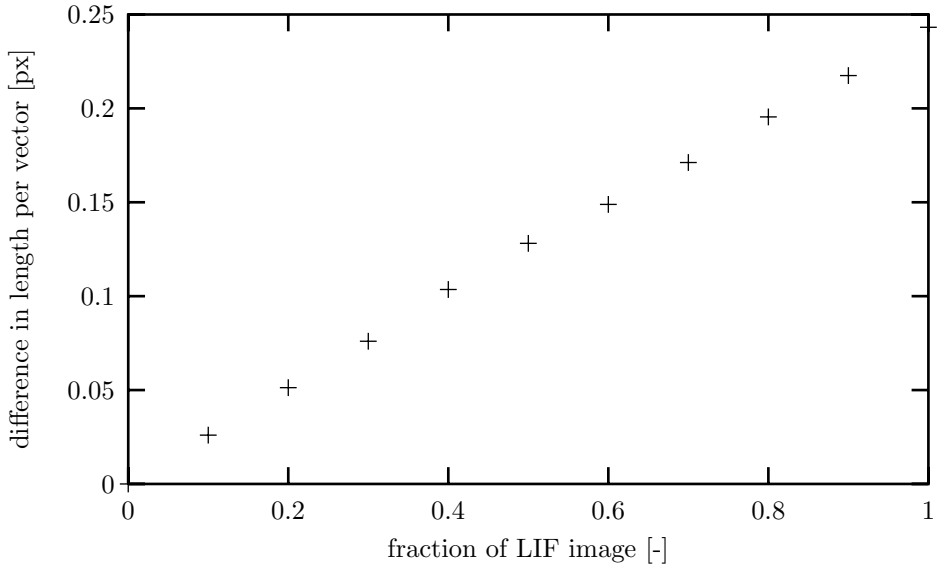

Figure 5.22: The difference in length of the total vector field (with sputious vectors) divided by the number of vectors, as function of the fraction of the LIF frame added to a PIV frame.

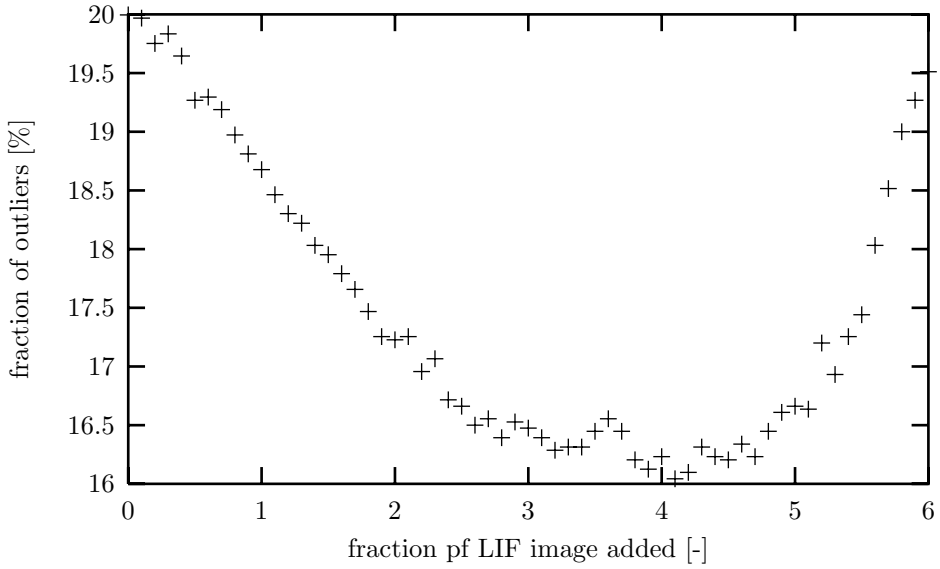

Figure 5.23: The number out outliers detected as function of the fraction of the LIF image added. The discard value used was 0.6

number of outliers was caused by the fact that the odd and even lines of the two camera systems are read out by different pipeline processors which can have a slightly different gain and offset. By adding the LIF frames (which are almost black, so consist of a background only) it is not impossible that the difference in background between odd and even lines in the LIF images compensates the difference in background between odd and even lines in the PIV images. When however the greyvalue distributions of the odd end even lines are plotted, they appear to be on top of each other as can be seen in figure 5.24. This figure shows the averaged greyvalue distribution for the odd and even lines of 10 frames for the first 100 greyvalues. Besides, the grey value distribution of the odd lines of a single frame are plotted. As can be seen all three lines show the same structure. Apparently some grey values are more likely to occur than others. If this was not the case, the average over 10 frames should have been smoother than the result for the single frame. This will act as source of error in the PIV measurements. If now part of a LIF frame is added to the PIV frame, the greyvalue distribution appears much smoother, as shown in figure 5.25. This probably explains the reduction in the amount of outliers in adding LIF images to the PIV frames. The change in the difference in length of the vectors calculated from the original PIV frame and the modified PIV images is probably mainly due to the reduction in the number of outliers. Although these results seem to give an opportunity to improve the quality of the PIV measurements done with these cameras in the future, they do not give the desired insight to the influence of the fluorescein structures present in the PIV frames on the velocity measurements.

In the PIV frame clearly some bright lines can be seen. These lines are the reflections described in section 4.3.3 and cause the gap in the velocity profiles shown.

In figure 5.26 a series of 4 successive combined velocity/concentration fields is shown. Because no fluorescein is present near the wall, only the center region of the pipe is shown. The velocity vectors shown are the real velocities minus a constant displacement which is almost equal to the maximum velocity of the flow. As can be seen, the LIF structures are recorded several times before they leave the measurement volume. It is therefore possible to look at the development of these structures as a function of time. As was mentioned in section 5.2.3 the growth of the structures due to diffusion when they are transported by the mean flow over a distance of 100 mm is only 0.1 mm. The growth of the structure near the right edge of the figures is much larger than this value and must be therefore due to fluid motion in the direction perpendicular to the light sheet.

5.4 Measured scalar fluxes

In this section we consider the results for the turbulent transport terms or scalar fluxes. The best way of computing these turbulent transport terms is investigated.

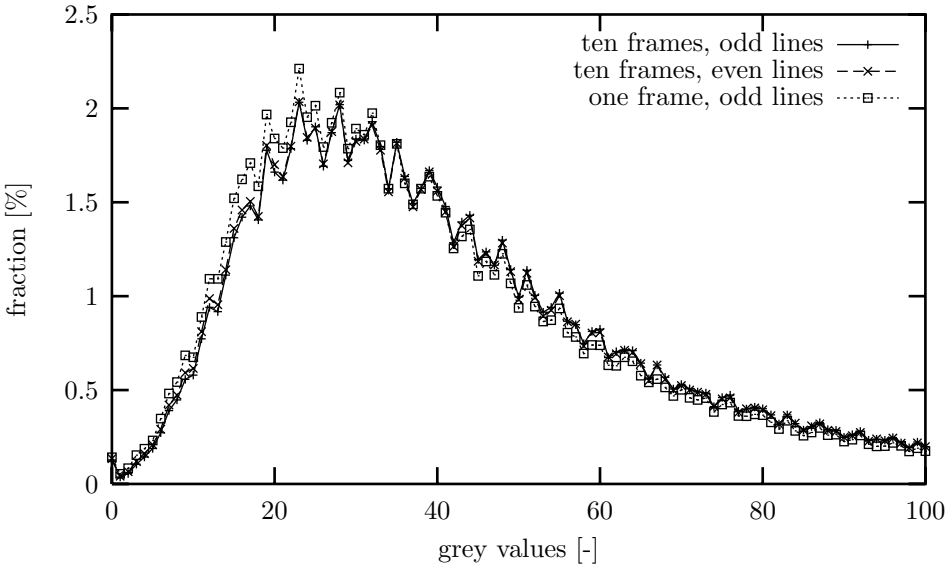

Figure 5.24: Averaged grey value distribution of the odd and even lines of 10 PIV frames, together with the greyvalue distribution of the odd lines of one PIV frame.

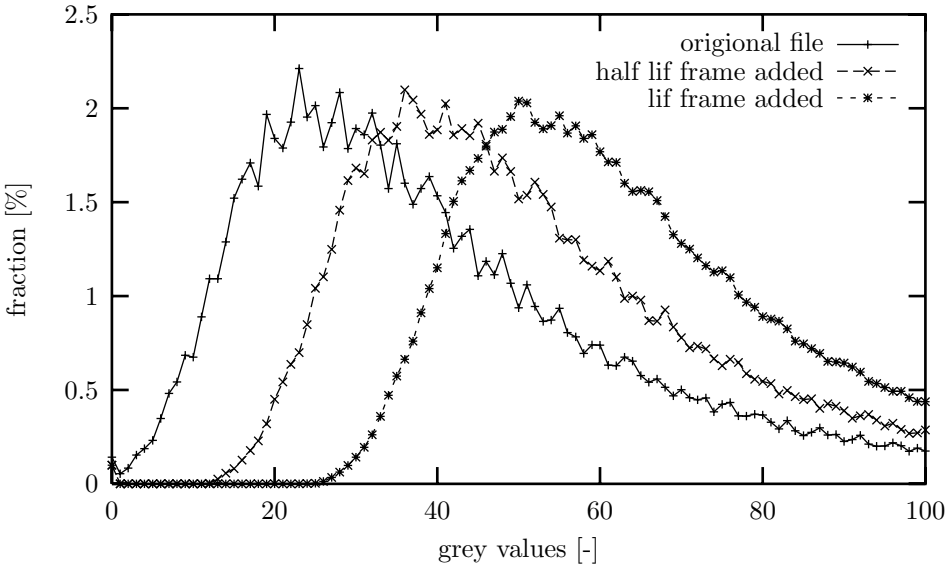

Figure 5.25: Greyvalue distribution of a PIV frame, a PIV frame with half a LIF frame added and a PIV frame with one LIF frame added.

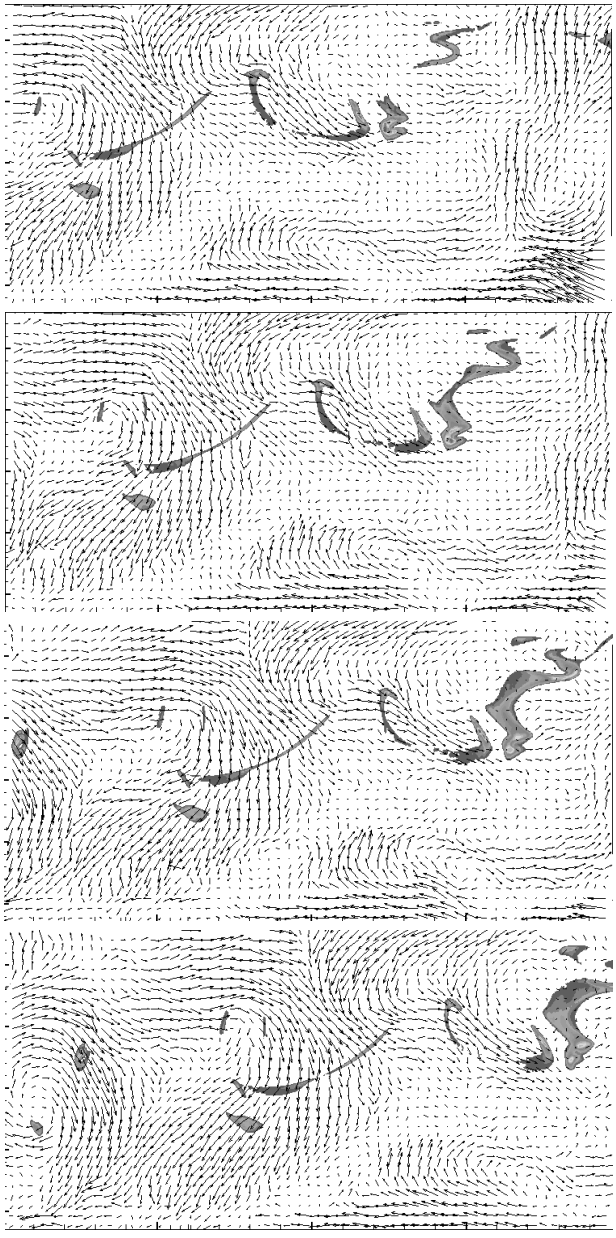

Figure 5.26: A small series of combined PIV-LIF measurement. The flow is from left to right. The length of the domain shown is 45 mm. A constant displacement is subtracted from the vector fields. The evolution of the structures due to the 3D effects in the flow field can be seen.

The accuracy of the measured transport terms is estimated by comparing them with transport by the mean flow.

Several methods of computing the scalar fluxes were tested. All methods were tested on the first or the second measurement position. Usually the velocity fluctuations are computed with respect to the mean velocity averaged over the streamwise direction for all the measurement frames. This is done with the idea in mind that the velocity field is a function of the radial position only. For a position not too far downstream from the injection needle, the wake of the needle is still significantly present in the flow field (see figures 5.4 and 5.6, section 5.1.2). So in that region the velocity field is a function of both the radial and the streamwise position. The first method examined in computing the correlation is not to use velocity fluctuations with respect to the streamwise averaged velocity field, but the velocity fluctuations computed with respect to the local mean velocity. This will remove the effect that the development of the mean velocity field in the streamwise direction is incorporated as a velocity fluctuation. In figures 5.27 and 5.28 the results for the computed axial and radial correlation between the velocity and the concentration gradient at measurement position P1 are shown. As can be seen there is no significant difference between the curves except for three data points at the centerline. For all other points the differences are well within the statistical error in the data. The error bars shown represent the scatter of the data over the streamwise direction of the averaged correlation fields over one measurement position, supposing that all 61 measurement points in one measurement position in the streamwise direction are independent. Due to the fact that in reality the different downstream positions are correlated, this gives an lower limit of the sampling error. If there would have been an effect of the streamwise development of the mean velocity, this would have been most significant near the injection point. Far from the injection point the velocity profile becomes even more uniform in the streamwise direction. It can therefore be concluded that the effect of the streamwise development of the mean flow is not important for the other measurement positions. In the results for the turbulent transport presented in this chapter, for measurement position P1 the local mean velocities are used, whereas for the other measurement positions the streamwise averaged mean velocities are used in the computation of the velocity fluctuations used for estimating the concentration-velocity correlations.

The peak in the transport terms is located not exactly at the centerline of the pipe. This is caused by the fact that the injection mechanism was not exactly at the centerline of the pipe. The asymmetry of the data is caused by the asymmetry in the flow caused by the injection mechanism which is shown in section 5.1.2.

As was mentioned in chapter 2, the Reynolds-averaged mass-transport equation can be written in several ways. The effect of these two formulations on the estimation of the turbulent transport is investigated. First, tests were done using the following form of the equation (for a fully developed turbulent pipe flow, i.e.

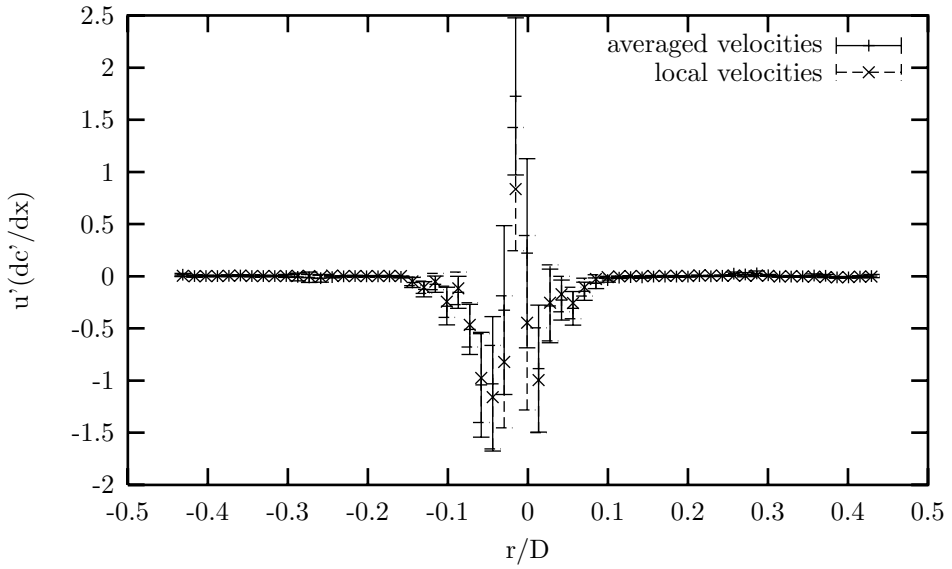

Figure 5.27: Comparison of axial correlations computed using locally averaged velocities and axially averaged velocity fields

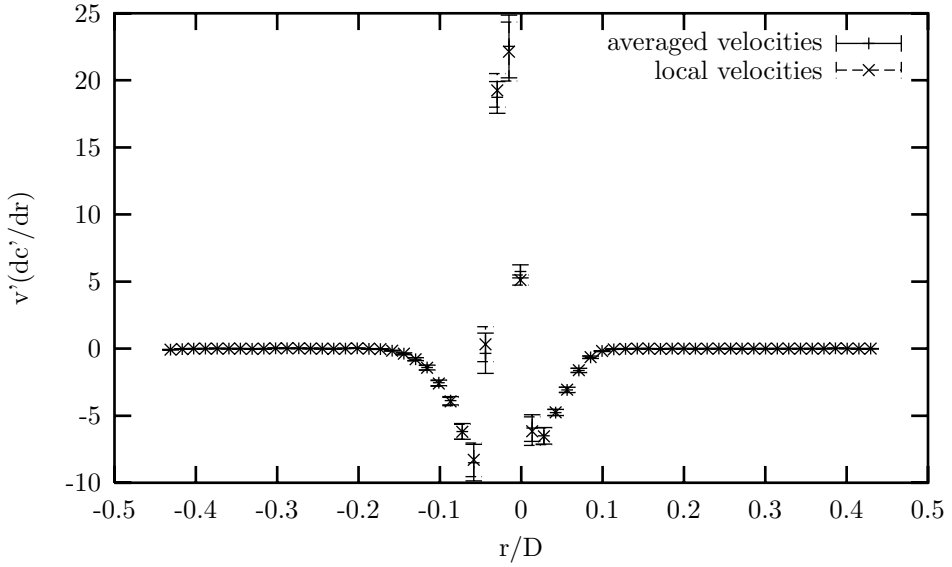

Figure 5.28: Comparison of radial correlations computed using locally averaged velocities and axial averaged velocity fields

$U_r = 0$):

$$U_x \frac{\partial \overline{c}}{\partial x} = -\overline{u'_x \frac{\partial c'}{\partial x}} - \overline{u'_r \frac{\partial c'}{\partial r}} + \mathcal{D}\left\{ \frac{\partial^2 \overline{c}}{\partial x^2} + \frac{1}{r}\frac{\partial}{\partial r}\left(r \frac{\partial \overline{c}}{\partial r} \right) \right\}. \tag{5.3}$$

To compute the first two terms at the right-hand side of the equations, first the concentration field has to be differentiated in space. This is done at a pixel to pixel base. After the differentiation the gradient fields are averaged on the same grid as the velocity fields were measured. The last step in the computation of the correlation is the multiplication of the velocity fluctuation and the concentration gradient fields and average over all fields.

Using continuity (5.3) can be written in an alternative way:

$$U_x \frac{\partial \overline{c}}{\partial x} = -\frac{\partial \overline{u'_x c'}}{\partial x} - \frac{1}{r}\frac{\partial r \overline{u'_r c'}}{\partial r} + \mathcal{D}\left\{ \frac{\partial^2 \overline{c}}{\partial x^2} + \frac{1}{r}\frac{\partial}{\partial r}\left(r \frac{\partial \overline{c}}{\partial r} \right) \right\}, \tag{5.4}$$

or

$$U_x \frac{\partial \overline{c}}{\partial x} = -\frac{\partial \overline{u'_x c'}}{\partial x} - \frac{\overline{u'_r c'}}{r} - \frac{\partial \overline{u'_r c'}}{\partial r} + \mathcal{D}\left\{ \frac{\partial^2 \overline{c}}{\partial x^2} + \frac{1}{r}\frac{\partial}{\partial r}\left(r \frac{\partial \overline{c}}{\partial r} \right) \right\}. \tag{5.5}$$

Written in this way the correlations can be computed by averaging the concentration fields on the grid of the velocity field, multiply them with the velocity fluctuation fields, average the resulting correlations and then carry out the differentiation on the averaged correlation between concentrations and velocity fluctuations. Processed in this way, the axial correlations change dramaticly with respect to the computational method used to obtain the terms in (5.3). The radial correlations (which are an order of magnitude larger than the axial correlations) do not change very much. In our opinion the correlations computed in the second way are more accurate and therefore only these results are shown. Although the results of the second method are more accurate the statistical error on the axial correlations is so large that the results are just barely statistical significant at the first measurement position. At the the second measurement position the axial correlations are of the same order as the statistical error.

In figure 5.29 the scalar transport by the mean flow is shown at the measurement positions downstream from the injection point. All results are streamwise averages of the locally computed correlations over the image width(i.e., 0.9 D). Especially for the terms containing streamwise gradients this streamwise averaging is necessary to be able to present sufficiently converged data. However, due to this streamwise spatial averaging an error is made when the correlations develop in the streamwise direction. This error is small when the streamwise development of the correlations is small. This is not the case for the first measurement position. As shown in figure 5.29 the height of the curves decreases rapidly with the downstream direction. The reason for that is the $1/x^2$ decay of the centerline concentration as found in figure 5.7. In figure 5.30 the total turbulent transport is shown. In figures 5.31 and 5.32 the contributions of the axial and the radial transport terms are shown separately.

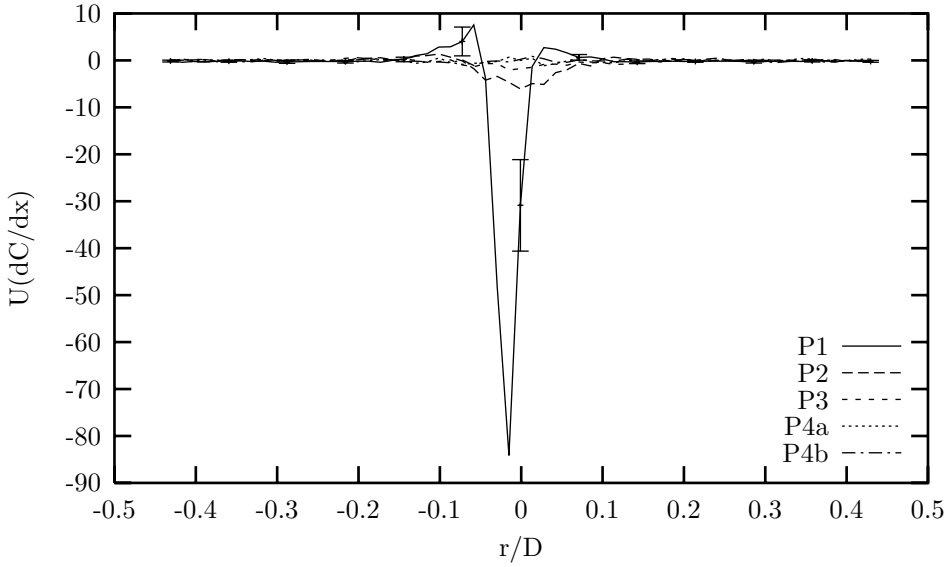

Figure 5.29: The product of the mean concentration gradient in the streamwise direction with the mean velocity at several distances from the injection point

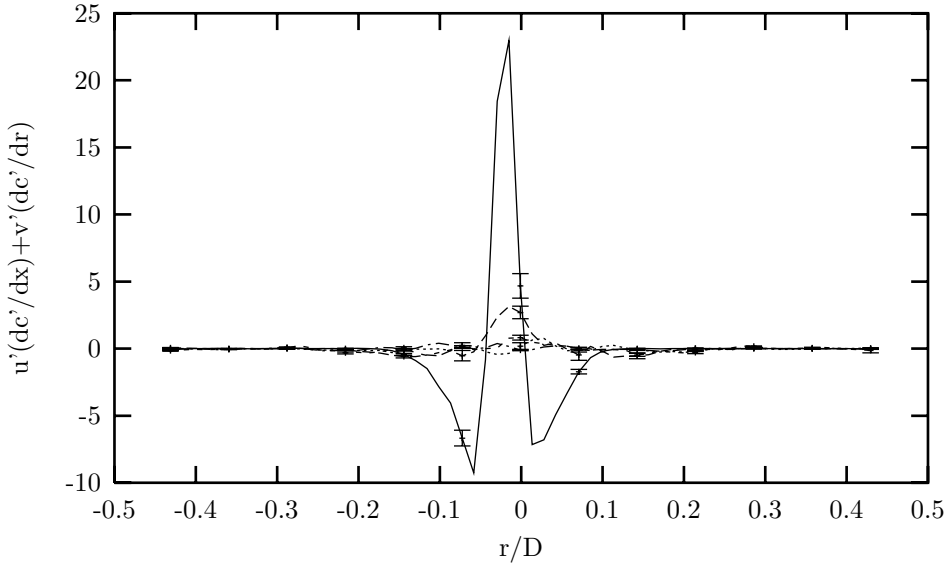

Figure 5.30: The total measured cross correlation terms at several distances from the injection point.

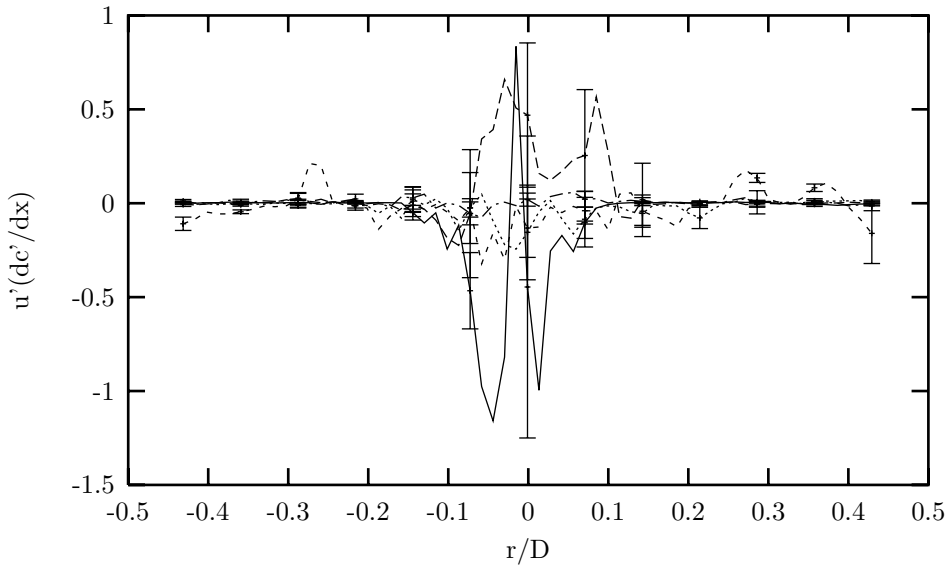

Figure 5.31: The measured axial cross correlation terms at several distances from the injection point.

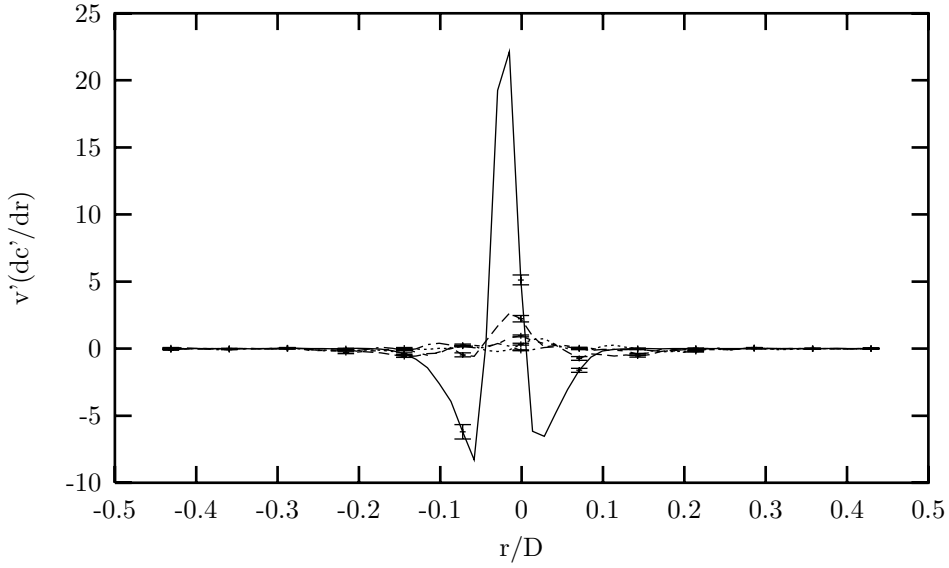

Figure 5.32: The measured radial cross correlation terms at several distances from the injection point.

As can be seen in figures 5.32 and 5.31 the uncertainty in the axial correlations seems to be much larger than the uncertainty in the radial correlation. This is mainly due to the fact that gradients in the streamwise direction are much smaller than gradients in the radial direction.

In figure 5.4 we compare for each downstream position the transport by mean advection with the sum of the turbulent transport terms. The difference between both transport terms at the first measurement position is quite large. For the other positions the difference decreases in proportion to the downstream position, but the noise increases.

The reason for the large discrepancy between the mean advection and the turbulent transport terms just after the injection point are the huge radial gradients present just behind the injection point. The gradients are calculated on a rather coarse grid compared to the width of the plume. The only way to solve this problem is to compute and present the gradients on a pixel to pixel base instead of on the 16×16 pixel grid used now.

As can be seen in figure 5.11 in which the concentration profile scaled with the local mean centerline concentration and the local standard deviation of the plume is shown, the concentration profile is equal to a Gaussian profile. The centerline concentration shows a $1/x^2$ decay as illustrated in figure 5.7, whereas the width of the plume grows linearly with the distance from the injection point (see figure 5.8). The mean concentration profile can therefore indeed be written according to the theoretical result presented in section 2.4.1 equation 2.34:

$$\overline{c(x,r)} = \frac{SU}{2\pi(\overline{u_r'^2} + \overline{u_\phi'^2})^{\frac{1}{2}} x^2} e^{\frac{-U^2}{2\overline{u_x'^2}} \frac{r^2}{x^2}}, \tag{5.6}$$

as derived in section 2.4.1. In this equation S is the source strength of fluorescein, U is the mean centerline velocity and u_i' is the fluctuating velocity component in the i direction. If we now use the parameters obtained in section 5.2.1 for the centerline concentration and the spreading of the plume, equation 5.6 becomes:

$$\overline{c(x,t)} = \frac{2.025 \times 10^{-4}}{x^2} e^{-\frac{r^2}{2(0.0349x)^2}}, \tag{5.7}$$

As can be seen, the estimated spreading rate scales with the axial turbulence intensity. The fitted value for this quantity is, according to the results presented in figure 5.8, equal to 0.0349. If we compare this with the results obtained from the PIV and LDV measurements we see that the actual value for the axial turbulence intensity level is about 0.045 (see section 5.1.2).

The modeled centerline concentration makes it possible to estimate the source strength of the point source used. To be able to do so, first the radial and the tangential turbulence intensity have to be estimated. The tangential turbulence intensity at the centerline of a turbulent pipe flow is assumed to be equal to the radial

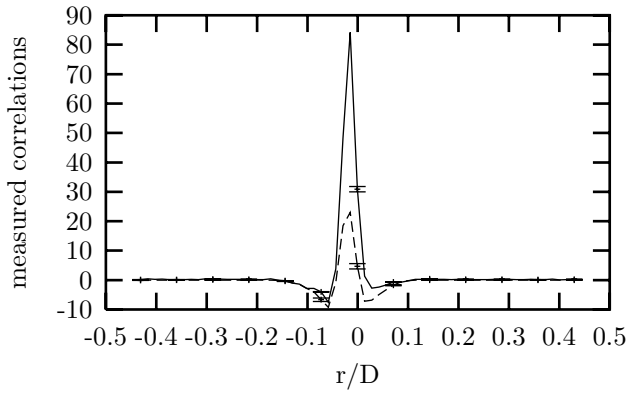

(a) Position P1

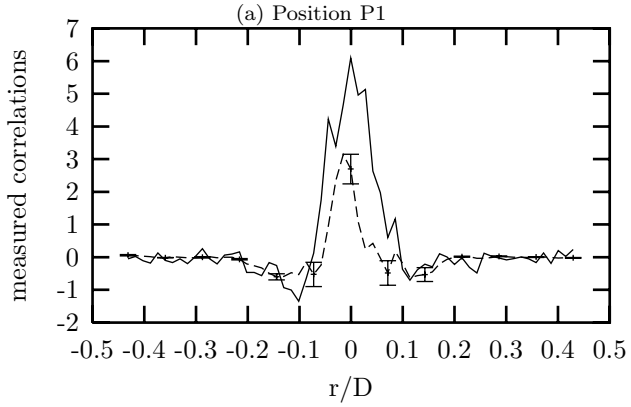

(b) Position P2

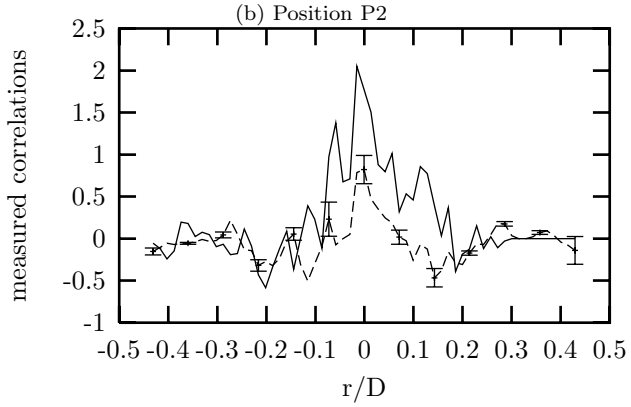

(c) Position P3

Figure 5.33 continued

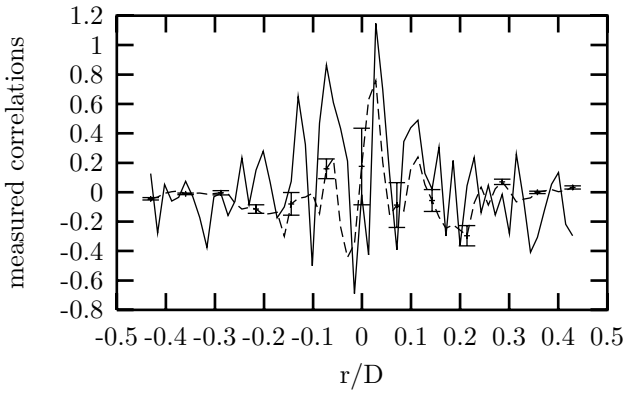

(d) Position P4a

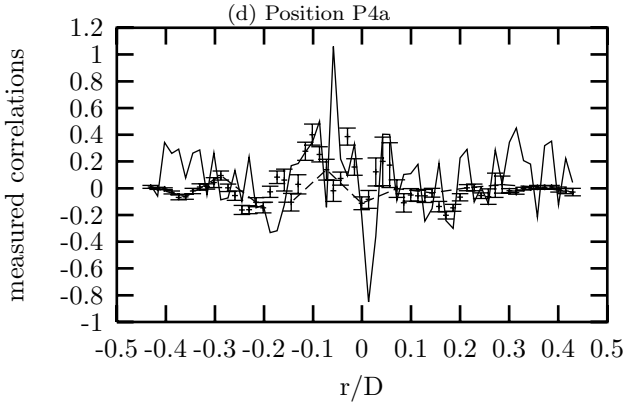

(e) Position P4b

Figure 5.33: Comparison of the summed radial and axial correlation with the product of the mean profiles, solid lines represent the product of the mean profiles, dashed lines represent the summed correlations.

turbulence intensities. With the measured radial centerline turbulence intensity of 0.034 the estimated source strength of fluorescein becomes 6.2×10^{-5}.

From the concentration profile given in (5.7)the derivative of the concentration with respect to x can be calculated:

$$\frac{\partial c}{\partial x} = -4.05 \times 10^{-4} \, \frac{e^{(-410 \, \frac{r^2}{x^2})}}{x^3} + \frac{0.166 \, r^2 \, e^{(-410 \, \frac{r^2}{x^2})}}{x^5} \tag{5.8}$$

Since in the derivation of this equation the flow is supposed to be uniform multiplication of this equation by the velocity, is equal to the transport by the mean flow.

We also carried out experiments at a Reynolds number of 10.000. In figure

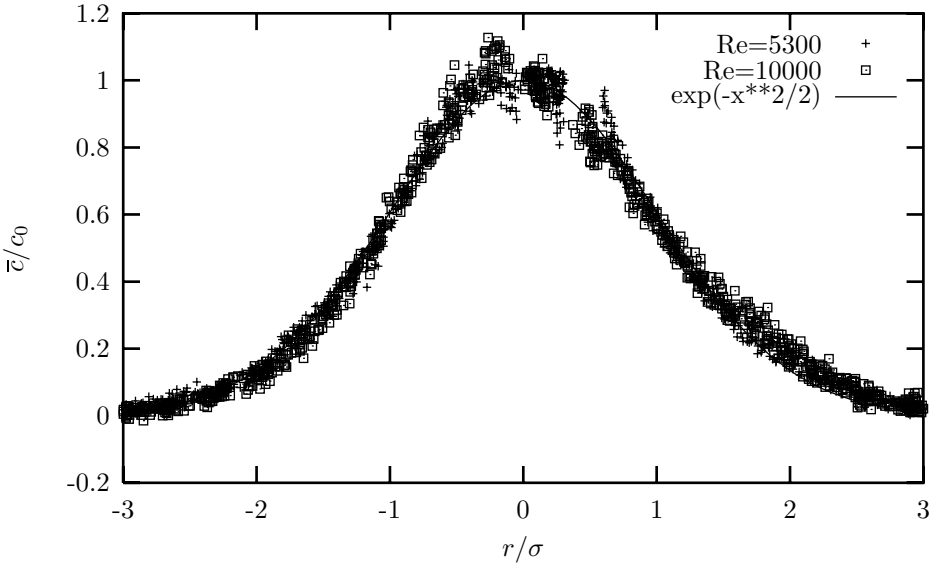

Figure 5.34: A comparison between the mean concentration profiles at two different Reynolds numbers.

5.34 the results for the mean concentration profiles of the two Reynolds numbers are compared. Due to the fact that near the centerline the characteristics of the turbulence are expected to become independent of the Reynolds number, the results are expected to collapse.

In figure 5.35 the correlation between the radial velocity fluctuations and the concentration $\overline{v'c}$ for the two Reynolds numbers are shown, scaled with the measured centerline concentration and the width of the plume. The correlation profile appears to collapse when it is scaled with the amplitude and the width of the concentration plume. According to the gradient transport theory, the radial transport should scale with the derivative of the mean concentration with respect r. The expected shape of the scaled correlation function is therefore:

$$c_1 \eta e^{-\eta^2/c_2^2} \tag{5.9}$$

with $\eta = r/\sigma$ and c_2 equal to $\sqrt{2}$. If this function is fitted through the two data sets plotted in figure 5.35 the following parameters are obtained:
For P1: $c_1 = 0.0243 \pm 0.0003$ and $c_2 = 1.460 \pm 0.010$
For D1: $c_1 = 0.0212 \pm 0.0004$ and $c_2 = 1.478 \pm 0.013$
The high accuracy follows from the fact the that all data points in the plots are supposed to be independent. This, however, is not the case, so the real inaccuracy of the obtained parameters is higher. The difference in amplitude of the estimated

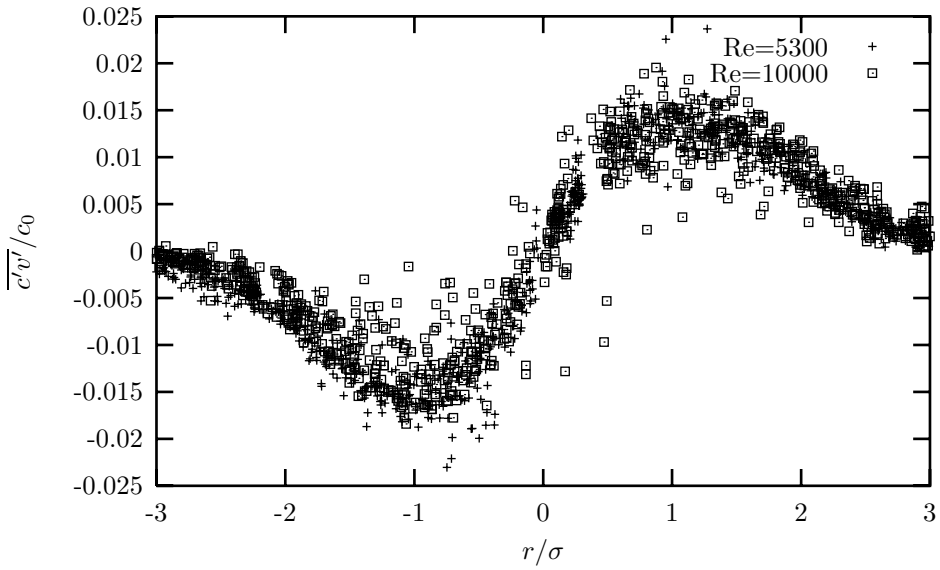

Figure 5.35: A comparison between the scaled $\overline{c'v'}$ profiles at two different Reynolds numbers.

transport terms for the two Reynolds numbers is 15%. This difference could be caused by the difference in turbulence intensity between the two Reynolds numbers. The difference in radial width of the fitted functions is only 1%. The fitted width of the data sets are 3% and 4% larger than the predicted $\sqrt{2}$. These differences are not significant concerning the noise on the data.

In figure 5.36 the correlation between axial velocity fluctuations and concentration fluctuations $\overline{c'u'}$ is given for measurement position P1. The correlations are scaled with the centerline concentration and the radial position with the width of the plume. Although expected from the theoretical relation for the derivative of the concentration profile, the result does not show an $1/x$ decay in the streamwise direction. This is probably caused by the resolution problem for the correlations. If (5.8) is divided by c_0 and r is scaled with the predicted width of the plume, the resulting equation decays in the streamwise direction as $1/x$:

$$\frac{1}{c_0}\frac{\partial c}{\partial x} = \frac{1}{x}\left[(r/\sigma)^2 - 2\right] e^{\frac{-r^2}{2\sigma^2}}. \tag{5.10}$$

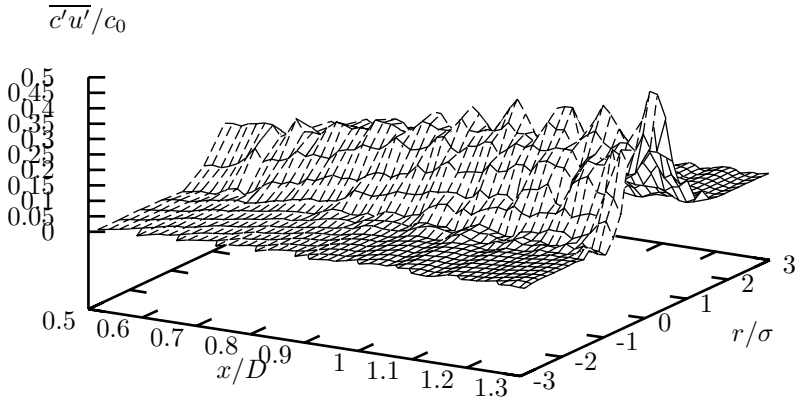

Figure 5.36: The scaled $\overline{c'u'}$ profiles at a Reynolds number of 5300.

Chapter 6

Investigation of the Mixing Process in an Axisymmetric Turbulent Jet Using PIV and LIF[1]

6.1 Introduction

Turbulent jet flow has been widely studied for its mixing properties. Mixing of passive scalars, such as heat or contaminants, is one of the significant features of the turbulence, and the jet flow in combination with turbulent mixing and the chemical reaction can be found in many practical applications (e.g. fuel injectors in combustion engines). In order to improve the efficiency of such devices, it is important to obtain more insight into turbulent mixing. In the experimental investigation of turbulent mixing, it is necessary to measure the instantaneous velocity and concentration field, simultaneously, since the mixing process can be described as the interaction between a velocity and concentration field.

In the present study, we investigated the mixing of a passive scalar contaminant in a turbulent free jet with a surrounding fluid. The Reynolds averaged equation for the conservation of the mean concentration of a passive scalar in an axisymmetric

[1]C. Fukushima, L. Aanen, J. Westerweel (2000) in: proceedings of the 10th international Symposium on Applications of Laser Techniques to Fluid Mechanics, Lisbon Portugal,July 10-13, 2000.

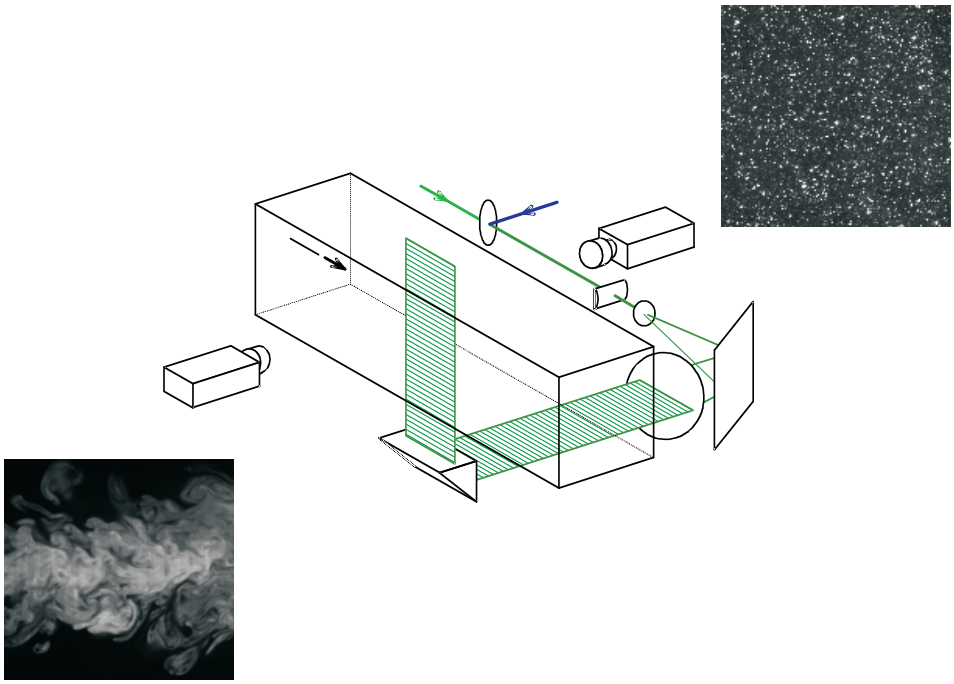

Figure 6.1: Schematic of flow field and optical configuration of combined PIV & LIF measurements.

jet is given by,

$$U\frac{\partial C}{\partial z}+V\frac{\partial C}{\partial r}=D\left\{\frac{\partial^2 C}{\partial z^2}+\frac{1}{r}\frac{\partial}{\partial r}\left(r\frac{\partial C}{\partial r}\right)\right\}-\frac{\partial}{\partial z}\overline{uc}-\frac{1}{r}\frac{\partial}{\partial r}\left(r\overline{vc}\right) \tag{6.1}$$

where U, V and C are the mean axial and radial velocity and the mean concentration respectively, z and r are the axial and radial coordinate respectively, D is the molecular diffusion coefficient, and $\overline{uc}$ and $\overline{vc}$ are the correlation of the axial and radial velocity fluctuation and the concentration fluctuations respectively. The terms on the left-hand side of (6.1) are the advection of the mean concentration by the mean flow. The first term on the right-hand side represents the molecular diffusion. The remaining terms on the right-hand side represent the transport of the passive scalar by the turbulence.

Of particular interest in the present study are the radial and axial turbulent fluxes of the passive scalar. Therefore, these simultaneous measurements were achieved by utilizing combined particle image velocimetry (PIV) and planar laser induced fluorescence (LIF). The combined PIV and LIF measurement system is already developed in our laboratory and applied for the mixing of a point source

placed at the centerline of a fully developed turbulent pipe flow (chapter 5).

The aim of the present study is to obtain a reliable reference data set for the further investigation of chemically reacting turbulent jets. Detailed measurements are made for the mean and fluctuating velocity, mean concentration, concentration fluctuation intensity, and turbulent flux. In order to validate the present data set, the results are compared with the results of a direct numerical simulation (Boersma et al. 1998, Lubbers et al. 2000), various point velocity measurement (Panchapakesan & Lumley1993, Wygnanski & Fiedler 1969), and with the results of measurements with combined PIV/LIF (Law & Wang 1998), PTV/LIF (Webster et al. 2000) or LDV/LIF (Papanicolaou & List 1988). Additionally, the mass balance in equation (1) is examined in detail.

6.2 Measurement techniques

Particle image velocimetry (PIV) is used to measure the instantaneous velocity field in a planar cross section of the observed flow. With PIV, the fluid velocity is determined by measuring the displacement of small tracer particles, over a small time interval. The tracer particles are illuminated by a thin light sheet, which exposes the tracer particles two times, with a small time delay. The light scattered from the tracer particles is recorded with a CCD camera, where each exposure is recorded in a separate frame. The displacement of the particles is determined by computing the spatial cross-correlation in small interrogation windows of each frame pair. Sub-pixel displacements are estimated by means of a Gaussian peak fit to the correlation peak for both the horizontal and vertical components of the displacement (Westerweel 1993). The estimated precision for the measured displacement by the method is 0.05-0.10 pixel units (see also section 3.2).

The instantaneous concentration distribution in a planar cross section of the flow is measured with laser induced fluorescence (LIF). The concentration of a fluorescent dye is observed by measuring the amount of light emitted by the dye when it is illuminated by a light source with a known intensity distribution. The light that is absorbed by the dye is emitted at a longer wavelength, and the intensity of the emitted light is directly proportional to the local concentration of the dye. The instantaneous planar distribution of the emitted light is measured with a CCD camera. For the calibration, the measurement section is filled with a uniform dye concentration and a series of 100 images are recorded and then averaged at each pixel. Besides that, a series of 50 dark images are recorded after each measurement to determine the gray value offset for each pixel. The difference of these two yields the local light intensity distribution. The concentration distributions are determined by subtracting the gray offset value distribution, and then normalizing with the light intensity distribution (see also section 3.3).

Detailed descriptions of PIV are given by Adrian (1991) and Westerweel (1993),

and of LIF by Walker (1987) and Koochesfahani (1984).

6.3 Experimental configuration

The measurements are carried out in a rectangular test section ($110\times110\times300\text{mm}^3$) fitted in a closed-loop water pipe facility with a total length of 6 m, also described in chapter 4. A schematic of the experimental configuration is shown in figure 6.1. The jet is discharged by driving an electromotor which drives a syringe, and injected through a long thin needle with an inner diameter d of 1mm. A fluorescent dye (fluorescein) is used as a scalar, so that the Schmidt number Sc (i.e. the ratio of kinematic viscosity to molecular diffusivity) of the dye is 2075. This implies that the molecular diffusion term in equation (6.1) is negligible with respect to the turbulent diffusion. The self-preserving axisymmetric turbulent jet is then obtained in the test section some distance downstream of the nozzle. All the measurements are made in a plane through the centerline of the jet in the region of $z/d = 20-140$ at a Reynolds number Re ($= U_j d/\nu$) $= 2\times10^3$. This value was chosen to match the Re-number of a DNS by Boersma et al. (1998).

A combined PIV and LIF measurement system is already developed in our laboratory (see section 3.4). For the illumination of the PIV image and light source of the LIF measurements, a twin Nd:YAG pulsed laser (wavelength of 532 nm, 200 mJ per pulse) and a CW Argon-ion laser (wavelength of 488 nm, 2.4 W) are used respectively. Both the laser beams are combined along the same optical path and transformed into a light sheet (see figure 6.1). The light sheet has a thickness of less than 1 mm over a length of 50 mm, and is almost parallel across the test section with a width of 50 mm. The light intensity scattered by the particles and the light intensity of the fluorescent dye are recorded separately on two synchronized digital CCD cameras (Kodak ES-1.0, 992×1004 pixels). The observed common area is about 45×45 mm^2 using 55 mm micro Nikkor lenses. The alignment between these cameras is accurate within 3 pixels, i.e. less than 0.3% of the image dimension.

Both the PIV and LIF measurements do not influence each other by using a shutter and appropriate optical low-pass filters. In order to completely avoid mutual influence of the measurements, PIV and LIF measurements are made sequentially. In the present case, the time delay between the two laser pulses are 0.24, 1.2, and 2.4 ms at each streamwise section with center positions of the camera at z/d = 40, 80 and 120 respectively for PIV, so the particle-image displacement is about one-quarter of the interrogation domain. The exposure times are 0.9, 2.4, and 4.8 ms respectively for LIF. These times are a compromise between an exposure that is long enough to record an adequate image and short enough to avoid motion blurring of the image. The total duration of the measurement is 1.5-7.6 ms, which is shorter than the Kolmogorov time scale, so it is considered that the combined PIV and LIF measurements are made simultaneously. A sample image of each PIV and LIF

measurement is also shown in figure 6.1.

The signals from the cameras are digitized and recorded by two pipeline processors (DATACUBE MV-200), and then a continuous image sequence of 134 frames is obtained at a rate of 15 Hz with double trigger mode. For each measurement location, 12 sequences of images are recorded so that one measurement includes 804 frame pairs that cover a total measurement time of 53.6 sec.

6.4 Results and discussion

6.4.1 Mean Velocity and Turbulent Statistics

All the results are obtained at 3 positions in the streamwise section including 61×61 statistics at each position. The total of three positions correspond to a downstream distance in the z/d range of 20-140 with an axial and radial spacing of 0.75. However, in the initial mixing region the fluorescent dye and tracer particles are not yet well mixed, so that reliable data are obtained in the z/d range from 30 for the velocity field.

Figure 6.2 shows the decay of the mean centerline velocity and concentration as a function of the distance from the nozzle respectively. Each peak value is obtained from the least-square fit of Gaussian function, or parabolic function, to the mean velocity and concentration profile, and is recognized as the centerline value. The results for the mean velocity and the mean concentration clearly show the z^{-1} decay of the jet. The virtual origin of the velocity and concentration fields are 6.75 and 6.76 mm respectively. The value of $z_0 = 6.75d$ for the velocity field is slightly larger than the result of DNS (Boersma et al. 1998), which is $z_0 = 4.9d$, and that of the measurement (Wygnanski & Fiedler 1969), $z_0 = 3 - 7d$, since the virtual origin significantly depends on the Reynolds number and the initial condition of the jet.

The streamwise development of the half width for the velocity b_u and the scalar b_c are shown in figure 6.3. It is important to examine the development of the length scale in detail, since the present jet is not an ideal free jet in the far downstream region, due to the wall boundary of the test section. The results show the linear development of the length scale, where $b_u = 0.097z$ and $b_c = 0.125z$ respectively, and there is no wall constraint effect on the jet development within the present experimental extent. Each coefficient 0.097 and 0.125 agree with the average of previous results (Fischer et al. 1979). Therefore it can be expected that self-preserving turbulent jets are established in the present experiment.

The axial mean velocity for the 12 representative streamwise sections are shown in figure 6.4. The axial mean velocity U, which is normalized by the centerline velocity U_c, is plotted versus the non-dimensional radial coordinate, $\eta = r/(z - z0)$. All the profiles collapse onto a single profile within the experimental extent. When the profiles are examined in detail, a small reverse flow (i.e., a negative value of U) is observed in the region $|\eta| > 0.2$ in the far downstream region. If the velocity profile is

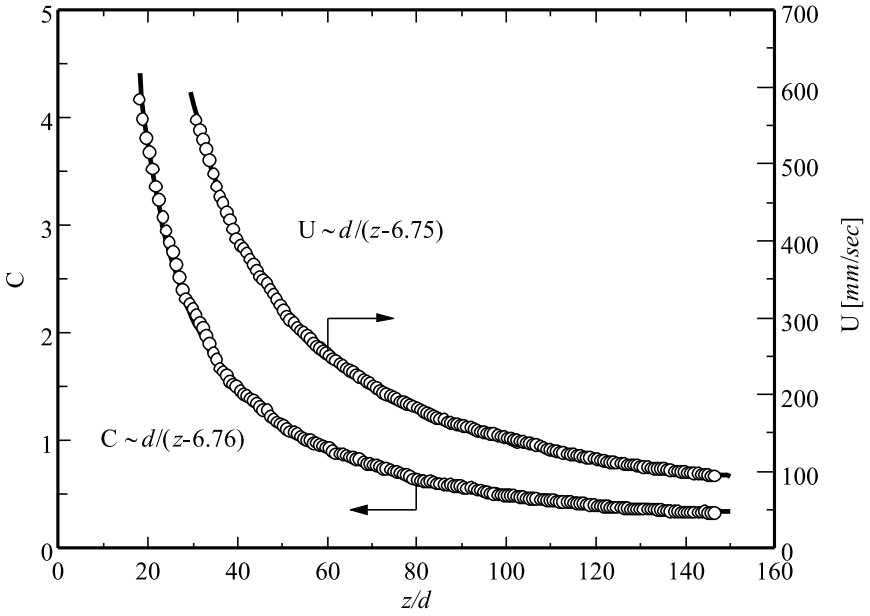

Figure 6.2: Variation of the centerline mean velocity and mean concentration along the jet axis.

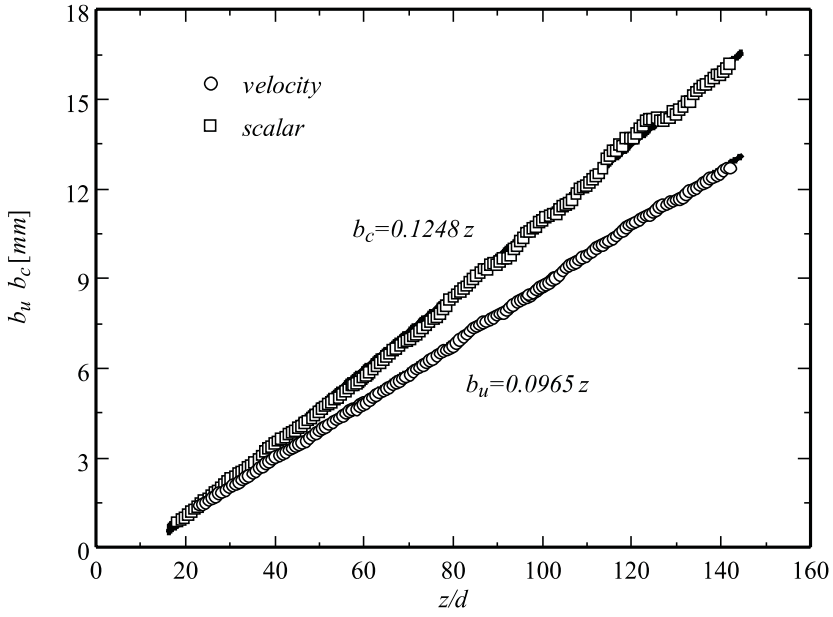

Figure 6.3: Streamwise development of the half width for the velocity field and concentration field.

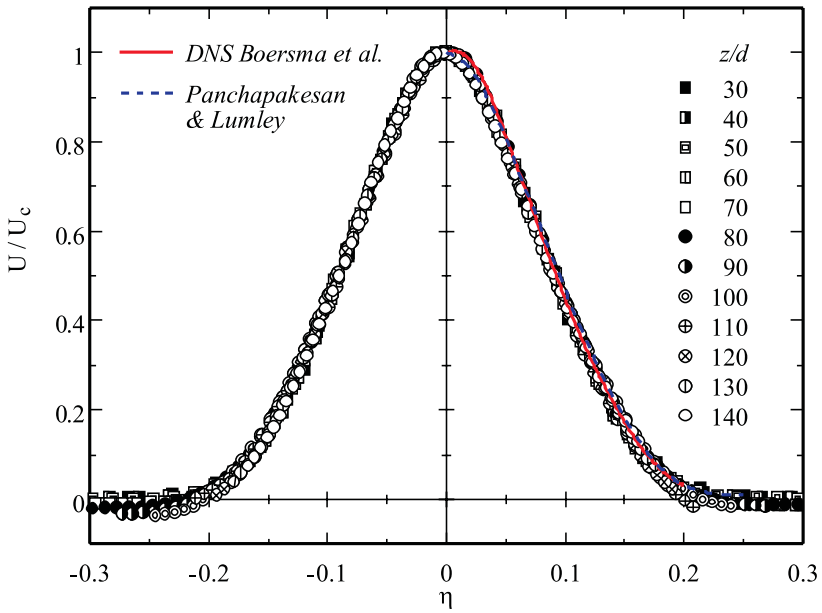

Figure 6.4: Axial mean velocity profile across the jet.

assumed Gaussian it becomes $U/U_c = exp(-K_u\eta^2)$. The average of the least-square fit to all the data gives $K_u = 84.9$, whereas in the experiment by Panchapakesan & Lumley (1993) a value of 75.2 (at a Reynolds number of 1.1×10^4) and in the DNS by Boersma et al. (1998) a value of 76.1 (at a Reynolds number of 2.4×10^3) have been found respectively. It means that the spread of the center region of the profile is slightly narrower than other results. Although, there is a slight effect on the velocity profile due to the wall constraint of the test section in the far downstream region, the profiles can be considered self-similar within the experimental extent.

Figure 6.5 shows the radial mean velocity profile at each representative streamwise section. The results in Panchapakesan & Lumley (1993) and Wygnanski & Fiedler (1969) are obtained from the curve fit of the axial velocity and the continuity equation. The present results exhibit a relatively high scatter due to the small absolute value of the V to the PIV resolution, however the averaged peak value throughout the data, and the distributions of the velocity profile agree well with the previous estimation.

The radial profiles of the turbulent intensity of the axial and radial velocity component are shown in figure 6.6 and figure 6.7 respectively. There is a distinct off-axis peak in the profile of the axial velocity fluctuations, which is also seen in the DNS results (Boersma et al. 1998) and the experimental results of Panchapakesan

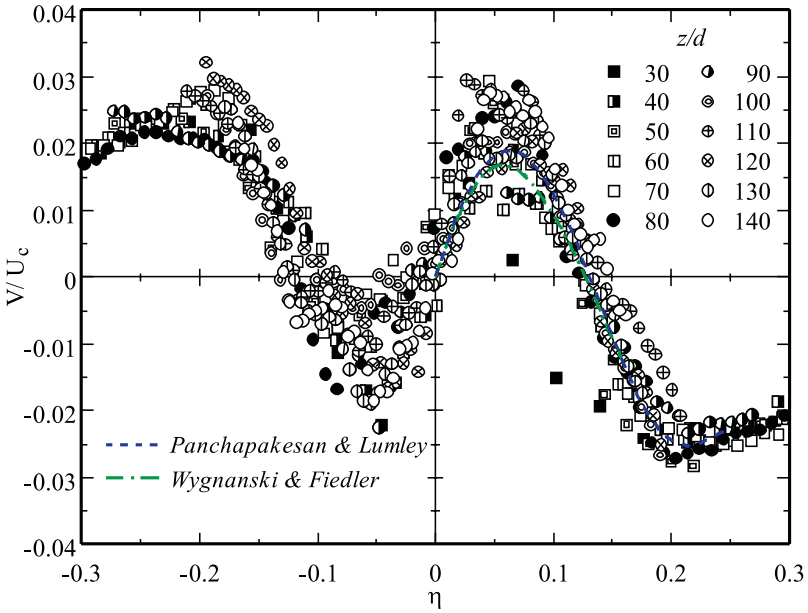

Figure 6.5: Radial mean velocity profile across the jet.

& Lumley (1993). This peak is expected from the profile of shear production of the kinematic energy, which has a distinct peak at nearly same location. The value at the centerline, the off-axis peak value and the location of the peak agrees well with the results of DNS and Panchapakesan & Lumley. For the radial velocity fluctuations, the present results almost agree with the DNS results of Boersma et al. (1998) near the centerline. The results from Wygnanski & Fiedler (1969) have quite higher peak values (figures 6.6 and 6.7) and the profile is narrower (figure 6.7) than the present or other results. This is probably due to the effect of the confinement of the jet, where the momentum loss arises due to the reverse flow, as suggested by Panchapakesan & Lumley (1993). In the present results, therefore, each turbulent intensity profile has reached its self-similar state in the region of $z/d \geq 60$. In the range of $z/d = 30 - 50$ (not shown here) the profiles have a relatively lower peak value at the center and higher value around the outer edge. As one of the reasons of such results, it may be supposed that the time delay between two laser pulses is adjusted for the nearest position from the nozzle, so the results include experimental uncertainty of 13-25% around $z/d = 50$.

The Reynolds shear stress profiles for the 12 representative streamwise sections are shown in figure 6.8. The Reynolds shear stress is asymmetric about the centerline, as expected; positive where the mean shear is negative, and negative where the mean

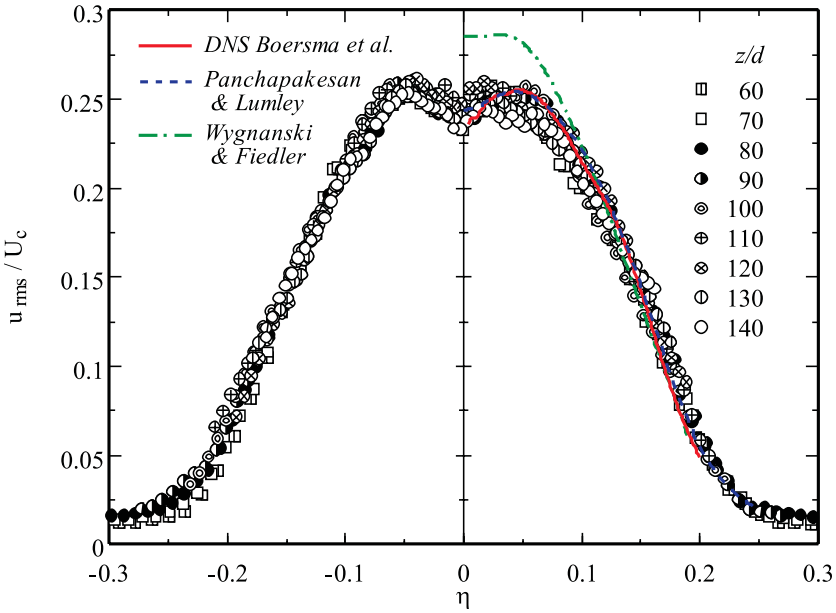

Figure 6.6: Turbulent intensity of the axial velocity fluctuations across the jet.

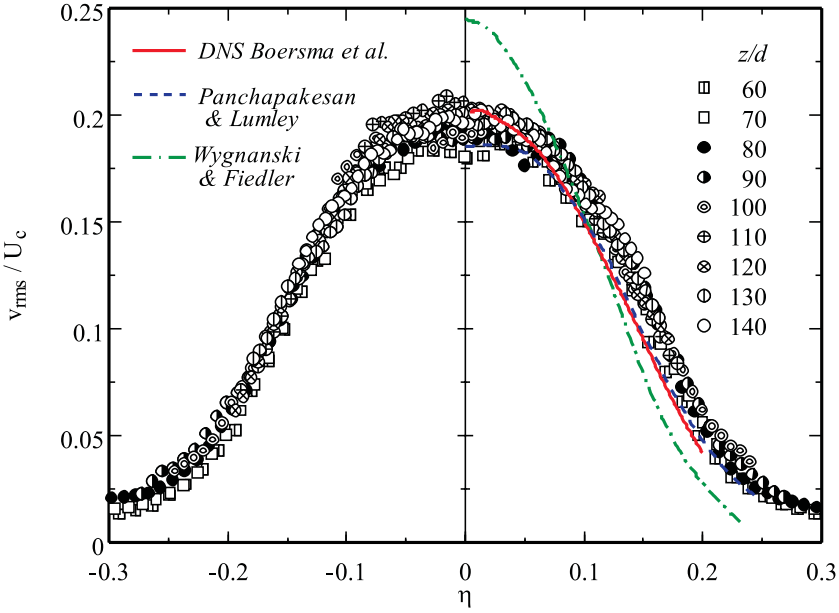

Figure 6.7: Turbulent intensity of the radial velocity fluctuations across the jet.

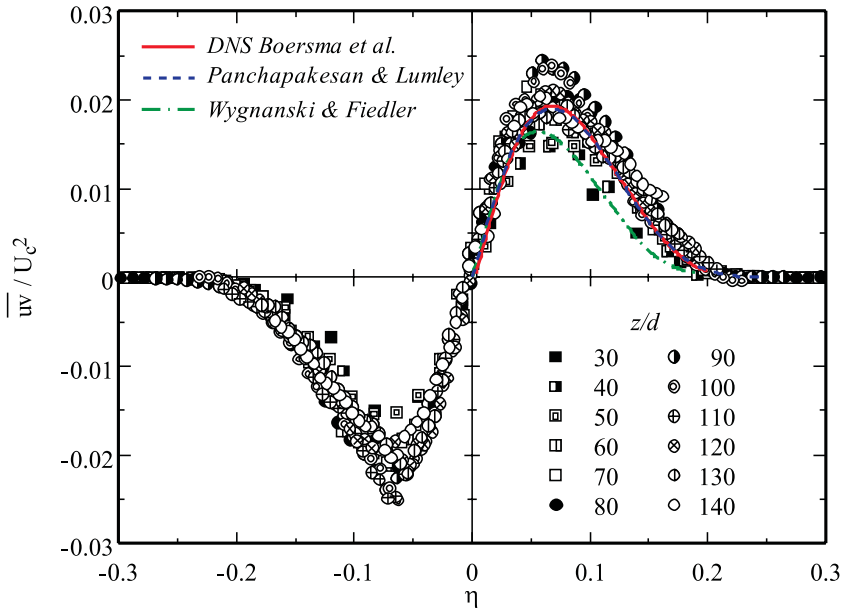

Figure 6.8: Reynolds shear stress variation across the jet.

shear is positive. In the present data, location of the peak value of the shear stress is 0.06-0.07, which agrees well with that of the radial component of mean velocity, and slightly larger than that of the turbulent intensity of 0.05. The sign of the shear stress corresponds to the transport of high momentum away from the centerline. The shear stress profiles almost agree with the results of DNS (Boersma et al. 1998) and Panchapakesan & Lumley (1993), while the result from Wygnanski & Fiedler (1969) has lower peak value and is narrower than our present measurements. Therefore, the Reynolds shear stress has reached its self-similar state in the region of $z/d \geq 60$.

6.4.2 Mean Concentration and Turbulent Flux

As shown in figure 6.2 and figure 6.3, the mean centerline concentration profiles collapse onto the curve proportional to z^{-1}. And the concentration field exhibit linear development, which is faster than the velocity field.

The radial profile of mean concentration across the center plane is shown in figure 6.9. The mean concentration C, which is normalized by the centerline concentration C_c, is plotted versus the non-dimensional radial coordinate, $\eta = r/(z - z0)$. All the profiles collapse onto a single profile within the experimental extent. When the mean concentration profile is assumed as Gaussian, it becomes $C/C_c = exp(-K_c\eta^2)$.

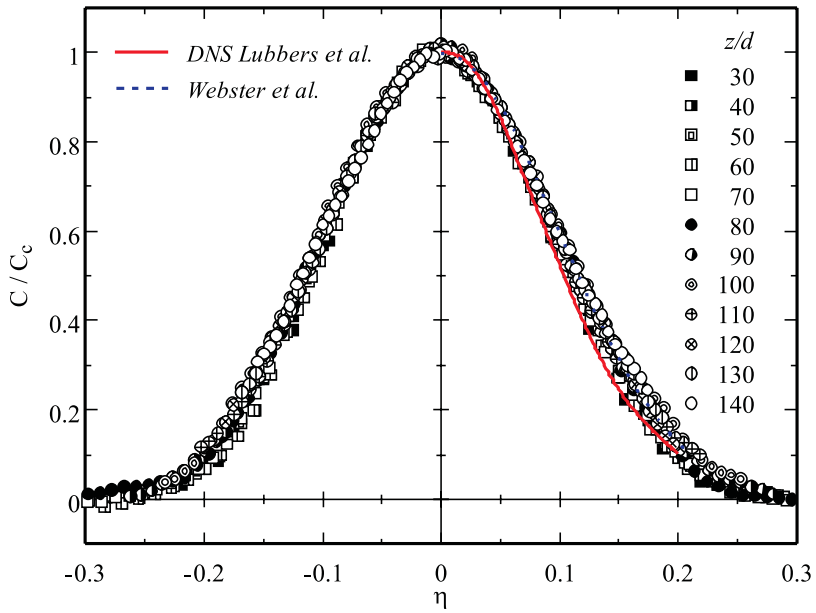

Figure 6.9: Mean radial concentration profile across the jet.

The average of the least-square fit to all the data gives $K_c = 56.9$, whereas in the DNS of Lubbers et al. (2000) at a Reynolds number of 2.0×10^3 a value of 59.1 was found. Although this means that the spread of the present profile is slightly wider than the DNS results, these K_c values seem in good agreement. Also the present data agrees well with the combined PTV (particle tracking velocimetry) and LIF measurements by Webster et al. (2000) at a Reynolds number of 3.0×10^3. Therefore, the mean concentration is considered to be self-similar and independent of the Reynolds number. When the value $K_c = 56.9$ is compared with $K_u = 84.9$, which is the value for the axial mean velocity, it is found that the concentration field spread faster than the velocity field as observed in figure 6.2. This is associated with the preferential transport of the scalar over momentum as suggested by Lubbers et al. (2000).

The radial variation of concentration fluctuation intensity is shown in figure 6.10. All the profiles at the representative streamwise section almost collapse onto a single profile. However, the profile is asymmetric about the centerline, and the peak value is significantly higher (especially negative η region) than DNS (Lubbers et al. 2000) and combined LDV/LIF measurement (Papanicolaou & List 1988). The negative region of the η correspond to the lower side of the test section. Therefore, there is

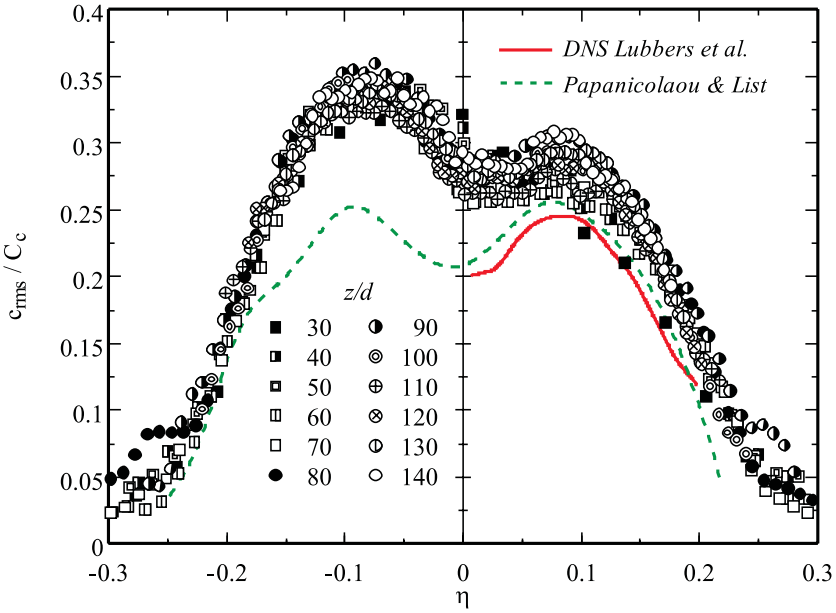

Figure 6.10: Concentration fluctuation intensity across the jet.

a possibility of the effect of the absorption of the light due to the fluorescent dye. In the present measurements, any adjustment of the results is not applied.

The axial and radial turbulent flux $\overline{uc}$ and $\overline{vc}$ are shown in figure 6.11 and figure 6.12 respectively. The turbulent flux $\overline{uc}$ and $\overline{vc}$ are normalized by the mean centerline velocity and concentration. The curves in these figures are the curve-fits given by Papanicolaou & List (1988), and by Law & Wang (1998). These results show a similar scatter level with the results given by Webster et al. (2000). The axial turbulent flux collapse onto a single profile, and the exhibition of a significant off-axis peak which is also seen in the result of Papanicolaou & List. The position of the off-axis peak is about 0.07, which is slightly larger than that of turbulent intensity, and almost agrees with that of Reynolds shear stress and radial turbulent flux $\overline{vc}$. The averaged value at the centerline almost agrees with the result of Law & Wang, however, the value around the off-axis is significantly higher than other results. The radial profiles of the turbulent flux $\overline{vc}$ show asymmetric profile about the centerline, as expected. The profiles collapse onto a single profile in the region from $z/d \geq 50$, and exhibit fewer scatter than observed in the axial turbulent flux. This is similar manner with the results of Webster et al. (2000). However, present results show slightly larger value of turbulent flux than those of Webster et al. and Law & Wang (1998). Boersma et al. (1998) pointed out that scaling of $\overline{uv}$, which is

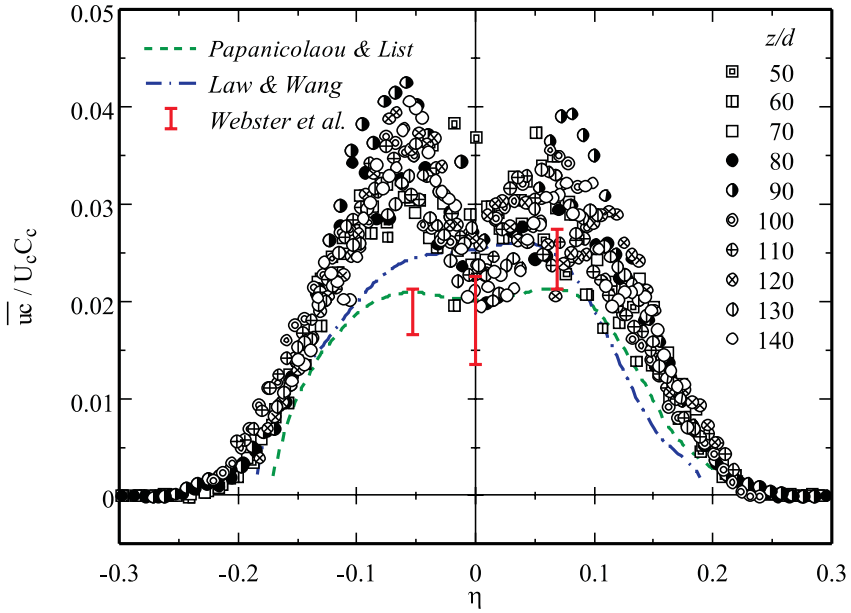

Figure 6.11: Axial turbulent flux $\overline{uc}$ across the jet.

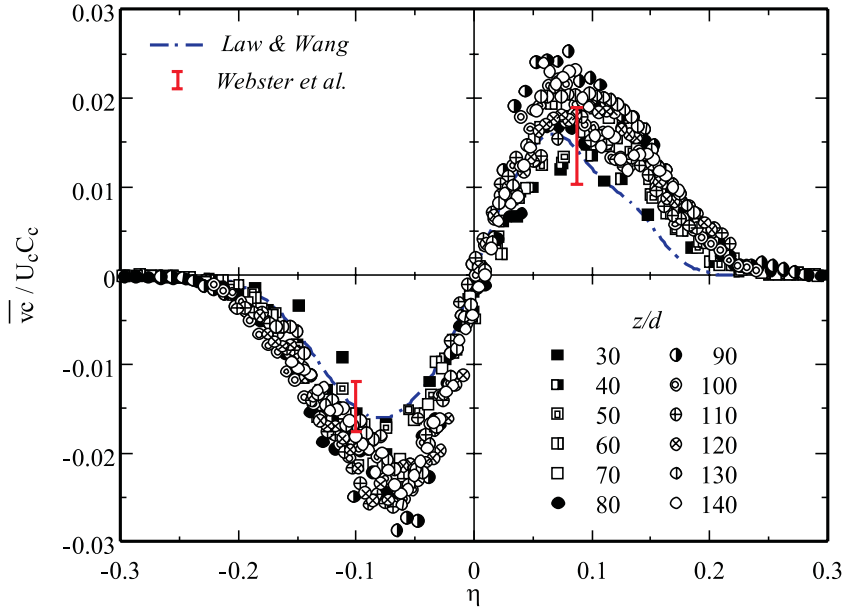

Figure 6.12: Radial turbulent flux $\overline{vc}$ across the jet.

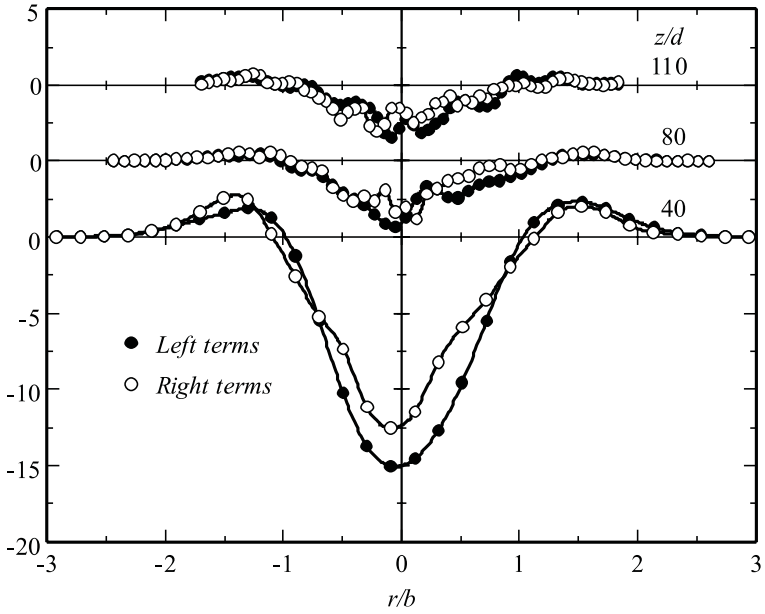

Figure 6.13: Estimation of the left and right hand side terms in the mass balance equation.

considering the growth rate of the half width, gives better results for the similarity profile of $\overline{uv}$. It means that the results could depend on the initial conditions of the jet. In fact there is a difference of the growth rate of the half width for the scalar between present data ($db_c/dz = 0.125$) and Webster et al. ($db_c/dz = 0.140$).

In order to assess the consistency of the present results, mass balances based on equation (6.1) are estimated. As mentioned above, molecular diffusion term is negligible since Sc $\gg$1. In addition, variation of the turbulent flux in the axial direction is also negligible applying the boundary layer approximation, i.e. $|\partial\overline{uc}/\partial z| \ll |(1/r)\partial r\overline{vc}/\partial r|$. The results are shown in figure 6.13 for 3 representative streamwise sections. The left hand side (closed symbols) of the equation (1) is slightly larger than right hand side (open symbols), which is observed most of the streamwise sections. This is probably due to the finite spatial resolution of the present measurements and the fact that the concentration fluctuations are highly intermittent. However, the difference between these terms is at an acceptable level.

6.5 Conclusions

In the present study, in order to obtain the reliable data set, detailed measurements were made for the mixing of a passive scalar in an axisymmetric turbulent free jet utilizing combined PIV and LIF method. The results were compared with the DNS, various point measurements and combined measurements. All the profiles of the mean velocity, turbulent intensity, Reynolds shear stress, mean concentration, concentration fluctuation intensity, and turbulent flux collapse onto each single profile. The results for the velocity field exhibit good agreement with the previous results, which is within the statistical sampling error. Although the discrepancy was not recognized in the mass-balance equation of the present measurements, some scatter especially in the axial turbulent flux and asymmetric profiles in the concentration fluctuation intensity, were observed. Therefore, it is necessary to increase the duration of the measurement, or to adjust the relation between the fluorescein concentration and exposure time.

The present results demonstrate the possibilities and the limitations of this combined PIV and LIF method for investigating turbulent mixing. We plan to continue this kind of investigation such as jet flow in combination with chemical reaction. In such an investigation, the local pH dependency of the fluorescent dye will be used to determine the influence of the turbulent mixing on the chemical reaction. Understanding of the turbulent mixing involving the chemical reaction is quite important for such as engineering design and environmental problems.

Chapter 7

Conclusions and Recommendations

In this chapter the most important conclusions based on the research presented in this thesis are summarized.

A measurement technique for doing simultaneous two-dimensional velocity and concentration measurements was developed and tested. The technique uses PIV for the velocity measurements and LIF for the concentration measurements.

Measurements with the combined PIV/LIF technique have been done done in two different flow geometries, a point source of a passive scalar placed at the centerline of a turbulent pipe flow, and a passive scalar dispersion in an axisymmetric turbulent free jet. The PIV technique is used to measure the flow field. The LIF technique is used to measure the concentration distribution. First the conclusions with respect to the PIV technique and its results are given. Second the conclusions are given for the LIF technique. Third the conclusions for the combined PIV-LIF measurement technique are discussed. Finally we give some recommendations for future work.

7.1 Conclusions

7.1.1 PIV measurements

- For the velocity measurements in the pipe flow experiments, the autocorrelation mode of the PIV technique has been used and for the jet flow experiments we applied the cross-correlation mode. Resulting velocity fields are found to be accurate in both modes.

- If the results for the mean and rms velocities of both experiments are compared

with LDV and DNS results, the results agree within the statistical error.

- The PIV measurements are slightly biased due to peak locking. The number of outliers is larger than 5%, which is usually taken as the upper limit for valid measurements. This is partially caused by the reflection lines present in the PIV frames. Another source of outliers is the difference in beam shape of the two YAG-beams, causing an increased number of outliers near the instream and outstream edges of the PIV frames.

- The number of outliers reduced when the background image of the LIF frames was added to the PIV images. This is probably caused by the fact that the gray value of the cameras is not a linear function of the light intensity. Adding LIF images (the background images of the LIF camera) to the PIV images appears to compensate for this effect.

- In the point source measurements the influence of the wake of the vertical part of the injection needle on the velocity profile is still measurable after 6 pipe diameters. The effect of the boundary layer of the injection needle decays within 2.5 pipe diameters behind the injection point.

7.1.2 LIF measurements

- The LIF technique was successfully implemented. For both flow geometries the results for the mean concentration are reliable and are in good agreement with results from a DNS and the results predicted by a simple gradient transport theory.

- The resolution for the concentration values is rather poor. The uncertainty of the data is at least 2% of the maximum concentration due to the limited number of grey values and noise on both background image, calibration image and measurement frames.

- For the point source experiments, the results for second-order statistics of the concentration measurements are only qualitative due to lack of spatial resolution and the thickness of the light sheet, which are both much larger than the Batchelor-length scale. Results for concentration pdf and scalar dissipation are not reliable for the same reason.

- Due to the small amount of fluorescein injected in the point source experiments and the characteristics of the flow, it takes a long time before the results are statistically converged. Fluorescein is measured during 4% of the measurement time at 2 pipe diameters downstream of the injection point. For the jet measurements the convergence of the statistics is much faster.

- In the case of the point source, the measured mixing follows initially the expected $1/x^2$ decay for the centerline concentration as predicted by the advection limit of the theory for homogeneous turbulence. In this region the spreading of the plume is a linear function of the distance from the point-source. At 2.5 diameters behind the injection point a transition to a $1/x$ behavior of the centerline concentration decay can be seen, which implies a spreading proportional to the square root of the distance. This behavior is also predicted by the diffusion limit of the transport equations of homogeneous turbulence. Comparison of the centerline concentration and the spreading with the results of a DNS show a good agreement for $x/D > 1.5$.

7.1.3 Combined PIV/LIF measurements

- The two cameras used for the PIV and LIF measurements were aligned with an accuracy better than 3 pixels over the complete field of view for both experiments. In our case this means a maximal displacement of 0.135 mm between the velocity and the concentration field. This is small compared with the spatial resolution of the PIV images, so no correction is needed for this misalignment.

- For the point source experiments there are problems with the convergence of the statistics due to the intermittency of the concentration signal and a relatively short measurement time.

- The profile of the radial velocity-concentration correlation $\overline{v'c'}$ scales with the centerline concentration c_0 and the spreading of the jet σ.

- No significant differences can be seen between scaled profiles at a Reynolds number of 5300 and profiles with a Reynolds number of 10.000 for the point source experiments. This is in good agreement with the observation that also the spreading of the plume and the decay of the centerline concentration for the two Reynolds numbers are almost equal. This confirms our assumption that molecular diffusion plays no significant role in the dispersion of the mean concentration profile for high Schmidt numbers.

- Although results for $\overline{u'c'}$ and $\overline{v'c'}$ seem to be reliable it is not possible to find a closed mass balance for the point source experiments. This is probably caused by the fact that the mass balance contain the gradient of the correlation terms. The high noise level of the correlations make it hard to estimate the gradients with a high accuracy. The shape of the correlation profiles is measured correctly. For the jet experiments the mass balance is satisfied. This can be explained by the difference in intermittency between the jet and the point source experiments.

7.2 Recommendations

In order to be able to gain a better understanding of the mixing problem and to improve the measurement techniques used, the following recommendations are made:

Azimuthal correlations

To study the effect of the azimuthal correlations in the mass transport equation an asymmetric flow geometry should be studied. In that case also the azimuthal correlations have to be included in 2.23. To be able to do so, the measurement plane should be placed perpendicular to the flow direction in order to be able to measure the radial and tangential concentration gradients and velocity components.

Nonlinearity of the cameras

Investigate the effect of the nonlinearity of the cameras as described in section 5.3 on the PIV results.

Chemical reactions

To study chemical reactions, the pH dependency of the quantum efficiency of fluorescein can be used. Fluorescence only occurs as the pH level of the solution is above a certain threshold value. As can be seen in figure 7.1 this threshold value is about 6.5 (Buch 1995). If fluorescein is solved in an acid fluid, which mixes with a base fluid, fluorescence will only occur in the region where the two fluids are molecularly mixed. Such experiments can give new insight into the mixing process.

Coherent structures

If we look at the mixing of a passive scalar emitted from a point source in a turbulent pipe flow, it is clear that the mixing process is a strongly non-local and intermittent process. It is therefore clear that a statistical description as discussed in this thesis, will not capture all physical processes that are relevant during the mixing. For that reason an attempt should be made to look at the influence of structures in the flow field on the mixing process as function of the distance from the point source.

To do so, the mixing process should separated into two different regimes, macro-mixing and micro mixing. The macro-mixing is the redistribution of the scalar over the total volume of the flow by the large eddies. In our case the macro mixing causes the mean concentration profile to become uniform. This does not mean that there are no concentration fluctuations any more. The scalar is still not mixed on a molecular scale. The mixing of the scalar on a molecular scale is called the micro-mixing of the scalar.

There are different ways in labeling, or trying to label, events or structures in the flow. One can look at regions with high vorticity or regions with high shear. Following Hunt *et al* (1988) we suggest to use the deformation as the labeling parameter. The classification used is based on the value of the second invariant of the deformation tensor. This second invariant is given by

$$II = \frac{\partial u_i}{\partial x_j}\frac{\partial u_j}{\partial x_i}. \tag{7.1}$$

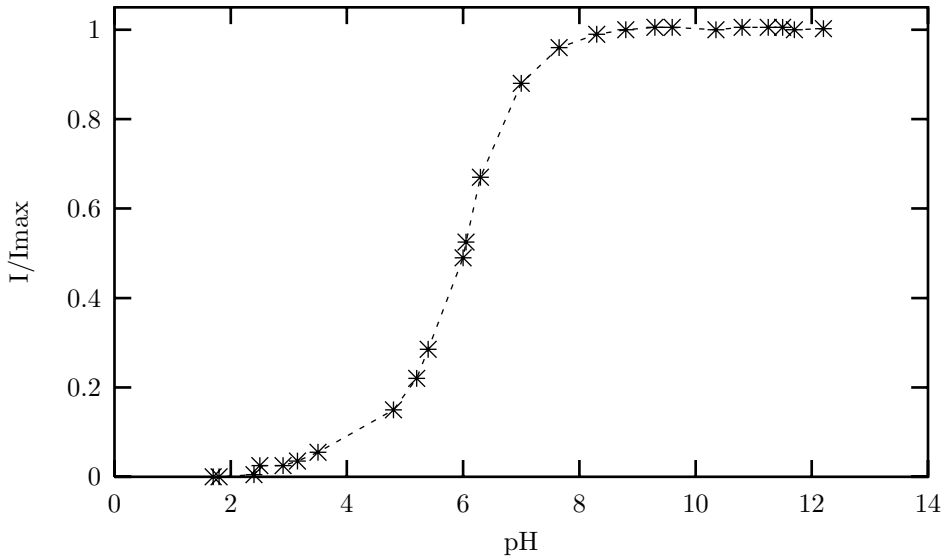

Figure 7.1: The relative fluorescence intensity of fluorescein as function of the pH value of the Fluorescein solution (Buch 1992).

Hunt *et al.* (1899) propose the following classification:
eddies: $II < -2II_{rms}$ and $p < -0.2p_{rms}$
convergence zones: $II > II_{rms}$
streaming zones: $\mid II \mid < II_{rms}$ and $u_i^2 > u_{rms}^2$
When the influence of the different zones on the mixing process is studied, in general the following characterization can be made:
In eddies there is only weak mixing. The fluid is rotating only without high deformation and mixing. The large eddies however do contribute to the macro mixing of the scalar.
In streaming zones, the mixing is also small. There is a strong transport of the fluid, so streaming zones are important in the macro-mixing of the flow also.
In convergence zones the fluid is deformed strongly, so they contribute to the micro-mixing of the scalar.

A way to link the structures present in the flow to mixing is to compute the joint pdf of the second invariant and the scalar concentration level. If the scalar is present mainly in one of the regions classified above, it can be said that these regions play an important role in the mixing of the fluid. It is expected that in regions where the deformation is strong, the scalar gradients are increasing, so the molecular mixing of the scalar is increasing, causing lower concentrations if the structures persist long

enough. This might cause lower concentrations in convergence zones. In streaming and eddy zones the flow deformation is small, so the only mixing mechanism is the molecular diffusion, which is very small in the experiments presented. It is therefore possible that, if the different zones persist long enough, further downstream high concentrations will be present in regions with lower second invariant values mainly.

Preliminary results for the pipe flow experiments suggest that there is no correlation between the presence of fluorescein and structures in the flow. This might be caused by the fact that the presented measurements are done only in the first 5 pipe diameters behind the injection point of the scalar. This means that the flow had only 5.5 eddy turn-over times to deform and organize the scalar structures.

Bibliography

Aanen, L. 1995. *LDA- and DPIV-measurements in a pipe flow under transition.* MEAH 125. Delft University of Technology, Rotterdamseweg 145, Delft, The Netherlands.

Aanen, L., Telesca, A., & Westerweel, J. 1999. Measurement of turbulent mixing using PIV and LIF. Machine Vision & Graphics 8.

Adrian, R.J. 1988. *Laser Anemometry in Fluid Mechanics-III.* Chap. Statistical properties of particle image velocimetry measurements in turbulent flow., pages 115–129.

Adrian, R.J. 1991. Particle-image techniques for experimental fluid mechanics. *Annu. Rev. Fluid Mech.*, **22**, 261–304.

Adrian, R.J. 1995. Limiting resolution of particle image velocimetry for turbulent flow. *Adv. in Turb. R.*

Adrian, R.J., & Yao, C.-S. 1984. Devellopment of pulsed laser velocimetry (PLV) for measurement of turbulent flow. Symp. Turbul., University of Missouri, Rolla.

Batchelor, G.K., Howells, I.D., & Townsend, A.A. 1959. Small-scale variation of convected quantities like temperature in turbulent fluid, Part 1. *J. Fluid Mech.*, **5**, 113–133.

Batchelor, G.K., Howells, I.D., & Townsend, A.A. 1959b. Small-scale variation of convected quantities like temperature in turbulent fluid. Part 2. The case of large conductivity. *J. Fluid Mech.*, **5**, 134–139.

Boersma, B.J., Brethouwer, G., & Nieuwstadt, F.T.M. 1998. A numerical investigation on the effect of the inflow conditions on the self-similar region of a round jet. *Phys. Fluids*, **10-4**, 899–909.

Borleteau, J.P. 2000. *PIV.* Dordrecht: Kluwer Academic. Chap. Seeding in a large quit water tank for the study of a wake flow with PIV technique, pages 384–390.

Brethouwer, G. 2001 (January). *Mixing of passive and reactive scalars in tur-*

bulent flows. Ph.D. thesis, Technische Universiteit Delft, Delft.

Bethouwer, G., Boersma, B.J., Pourquié, M.B.J.M., & Nieuwstadt, F.T.M. 1999. Direct numerical simulation of turbulent mixing of a passive scalar in pipe flow. *Eur. J. Mech. B/Fluids*, **18**, 379–756.

Buch, K.A. Jr. 1995. Laser induced fluorescence (LIF). *In: Short course on Flow Visualisation and Flow Structures*.

Buch, K.A. Jr., & Dahm, W.J.A. 1996. Conseved scalar mixing in turbulent shear flows. Part 1. *J. Fluid Mech.*, **317**, 21–71.

Durst, F., & Stevenson, D.H. 1997. *Sonderforschungsbereich 80 Ausbreitungs- und Transportvorgange in Stromungen*. Chap. The influence of Gaussian beam properties on laser Doppler signals.

Eggels, J.G.M., Westerweel, J., & Nieuwstadt, F.T.M. 1993. Direct numerical simulation of turbulent pipe flow. *Appl. Sci. Res.*, **51**, 319–324.

Elghobashi, S. 1994. On predicting particle-laden turbulent flows. *Appl. Sci. Res.*, **52**, 175–329.

Fischer, H.B., List, E.J., Koh, R.C.Y., Imberger, J., & Brooks, N.H. 1979. *Mixing in Inland and Coastal Waters*. New York: Academic Press.

Fox, R.W., & McDonald, A.T. 1985. *Introduction to fluid mechanics*. 3rd edn. John Wiley & Sons, Inc.

Fukuschima, C., Aanen, L., & Westerweel, J. July 10-13, 2000. Investigation of the mixing process in an axisymmetric turbulent jet using PIV and LIF. 10th international Symposium on Applications of Laser Techniques to Fluid Mechanisc, Lisbon, Portugal.

Gibson, C.H. 1968a. Fine structure of scalar fields mixed by turbulence. I. Zero-gradient points and minimal-gradient surfaces. *Phys. Fluids*, **11**, 2305–2315.

Gibson, C.H. 1968b. Fine structure of scalar fields mixed by turbulence. II. Spectral theory. *Phys. Fluids*, **11**, 2316–2327.

Goodman, J.W. 1968. *Introduction to Fourier Optics*. New York: McGraw-Hill.

Hinze, J.O. 1975. *Turbulence*. 2nd edn. McGraw-Hill, Inc.

Hunt, J.C.R., Wray, A.A., & Moin, P. 1988. Eddies, streams, and convergence zones in turbulent flows. *Pages 193–208 of: Proc. of the Summer Program 1998*. Center for Turbulence Research, Stanford.

Keane, R.D., & Adrian, R.J. 1990. Optimization of particle image velocimeters. Part I: Double-pulsed systems. *Meas. Sci. Technol.*, **1**, 1202–1215.

Keane, R.D., & Adrian, R.J. 1993. *Flow visualisation and Image Analysis*. Dordrecht: Kluwer Academic. Chap. Theory of cross-correlation of PIV images., pages 1–25.

Koochesfahani, M.M. 1984. *Experiments on turbulent mixing and chemical reactions in a liquid mixing layer.* Ph.D. thesis, California Institute of Technology, Pasadena.

Law, AW-K., & Wang, H. 1998. Simultaneous velocity and concentration measurements of buoyant jet discharges with combined DPIV and PLIF. 2nd International Symposium on Environmental Hydraulics, Hong Kong.

Lele, S.K. 1992. Compact finite difference schemes with spectral-like resolution. *J. Comp. Phys.*, **103**, 16–42.

Lubbers, C.L., Brethouwer, G., & Boersma, B.J. 2001. Simulation of the mixing of a passive scalar in a round turbulent jet. *Fluid Dyn. Res.*, **28**, 189–208.

Miller, J.N. 1981. *Standarts in fluorecein spectrometry.* London: Chapman and Hall.

Panchapakesan, N.R., & Lumley, J. 1993. Turbulence measurements in axisymmetric jets of air and helium. Part 1. Air jet. *J. Fluid Mech.*, **246**, 197–224.

Papanicolaou, P.N., & List, E.J. 1988. Investiagation of round vertical turbulent buoyant jets. *J. Fluid Mech.*, **195**, 341–391.

Prasad, A.K., Adrian, R.J., Landreth, C.C., & Offutt, P.W. 1992. Effect of resolution on the speed and accuracy of particle image velocimetry interrogation. *Experiments in Fluids*, **13**, 105–116.

Schlichting, H. 1979. *Boundary-Layer Theory.* 7th Ed. McGraw-Hill.

Tahitu, G.J.R. 1994. *The possibilities for laser-Doppler velovimetry in a turbulnt pipe flow.* MEAH 117. Delft University of Technology, Delft. M.Sc.-thesis (in Dutch).

Telesca, A. 1998. *Measurements on the mixing of a passive scalar in a turbulent pipe flow using DPIV and LIF techniques.* MEAH 180. Delft University of Technology, Rotterdamseweg 145, Delft, The Netherlands.

Walker, D.A. 1987. A fluorescent technique for measurement of concentration in mixing liquids. *J. Phys. E. Sci. Instrum.*, **20**, 217–224.

Webster, D.R., Roberts, P.J.W., & Raad, L. 2000. Simultaneous DPTV/PLIF measurements of a turbulent jet. *Exp. Fluids.*

Westerweel, J. 1993. *Digital particle image velocimetry. Theory and application.* Ph.D. thesis, Technische Universiteit Delft, Delft.

Westerweel, J. 1999 (Sept. 16–18). Theoretical analysis of the measurement precision in PIV. 3rd Int. Workshop on PIV, Santa Barbara, CA.

Westerweel, J., Draad, A.A., Hoeven, J.G.Th. van der, & Oord, J. van. 1996. Measurement of fully-developed turbulent pipe flow with digital particle

image velocimetry. *Experiments in Fluids*, **20**, 165–177.

Westerweel, J., Dabiri, D., & Gharib, M. 1997. The effect of a discrete window offset on the accuracy of cross-correlation analysis of digital PIV recordings. *Experiments in Fluids*, **23**, 20–28.

Willert, C.E. 1989. High resolution correlation peak detection. *ECE 251 C* UCSD, La Jolla.

Willert, C.E., & Gharib, M. 1991. Digital particle image velocimetry. *Experiments in Fluids*, **10**, 181–193.

Wygnanski, I., & Fiedler, H. 1969. Some measurements in the self-preserving jet. *J. Fluid Mech.*, **38**, 577–612.

Curriculum vitae

Lourens Aanen werd geboren op 22 december 1971 te Meerkerk. Nadat hij in 1990 het VWO diploma behaalde vertrok hij richting Delft. Daar heeft hij van 1990 tot 1995 Technische Natuurkunde gestudeerd. Zijn afstudeerwerk heeft hij gedaan op het Laboratorium voor Aero- en Hydrodyamica. De vakgroep fysische stromingsleer hoort weliswaar eigenlijk bij werktuigbouw, waar ze gewoon stromingsleer heet, maar er valt als natuurkundige prima af te studeren. Onder leiding van prof. dr ir. F.T.M. Nieuwstadt en Aswin Draad is er onderzoek gedaan naar het meten aan omslag laminair turbulent in een buisstroming.

Het onderzoek en de stromingsleer bevielen wel wat tot gevolg had dat hij in 1995 begon als OIO in de zelfde groep. Tijdens zijn OIO tijd is er gemeten aan de menging van een passieve scalar in een turbulente buisstroming. Omdat te kunnen doen moesten er twee meettschnieken gecombineerd worden. Het een en ander heeft geleid tot het boekje dat nu voor u ligt.

Naast zijn wetenschappelijk werk heeft hij zich ook op andere manieren op de vakgroep nuttig proberen te maken. Hij heeft twee jaar het Dispuut Panta Rhei gediend. Eerst een jaar als secrtaris, daarna een jaar als voorzitter. Zijn sociale leven buiten de vakgroep werd onder andere op peil gehouden tijdens de wekelijkse repetities bij het koor van het Delfts Studenten Muziek Gezelschap Krashna Musika.

Sinds 1 januari 2000 is hij werkzaam bij WL | Delft Hydraulics, waar hij zich bezig houdt op het gebied van de baggertechnologie en het slurrietransport.

De laatste grote verandering in zijn leven was het tegenkomen van de vrouw van zijn leven, wat geleid heeft tot zijn huwelijk op 28 juni 2002.